ALMA MATER STUDIORUM · UNIVERSITÀ DI BOLOGNA

SCUOLA DI SCIENZE
Dipartimento di Fisica e Astronomia
Corso di Laurea Magistrale in Astrofisica e Cosmologia

New LOFAR detection in the galaxy cluster A1413:

connection between non-thermal and thermal emission

Relatore:
Prof.ssa
Annalisa Bonafede

Candidato:
Giulia Lusetti

Correlatore:
Dr. Lorenzo Lovisari
Prof.ssa Myriam Gitti

Sessione I
Anno Accademico 2020/2021

Abstract

Clusters of galaxies are the largest virialized systems in the Universe and thus are ideal laboratories to study the formation and evolution of cosmic structures. The baryonic matter of clusters consists of stars and galaxies, and of the intracluster medium (ICM), a plasma which has been heated, through gravitational collapse, up to temperatures of tens of millions degrees at density of few hundreds particles per cubic meter, emitting mostly in the X-ray band. At the same time, radio observations have proved that the ICM is mixed with a non-thermal component, i.e. highly relativistic particles and large-scale magnetic fields, detected through their synchrotron emission. Diffuse synchrotron radio emission in the central and peripheral cluster regions has been found in many clusters, in the form of giant halos, mini-halos, and relics. This non-thermal component is linked to the cluster X-ray properties and understanding its origin is crucial for a comprehensive physical description of the ICM. Studying the connection between the cluster dynamical state and the properties of the diffuse radio emission is one of the main approaches to understand the origin of relativistic particles in galaxy clusters. In the last years, with the advent of new generation low-frequency radio telescopes, the classical dichotomy that connects merging events with giant halos and relaxed cool-core systems with mini-halos, has started to be questioned. In contrast to what has been generally believed, cluster-scale radio emission has also been observed in clusters with no sign of major mergers, indicating that minor mergers and/or sloshing of a dense cool core could trigger particle acceleration on larger scales and generate steep-spectrum radio emission.

This work is dedicated to the peculiar galaxy cluster Abell 1413 (hereafter A1413) that we discover to host a non-common radio emission. A1413 is a massive (M$_{500}$=5.99$^{+0.46}_{-0.45}$ $10^{14} M_{\odot}$), hot ($kT = 6.98^{+0.07}_{-0.06}\, keV$), and nearby (z=0.1427) galaxy cluster. Initially, A1413 was classified as a cool-core relaxed cluster (G. W. Pratt and Arnaud 2002, Pointecouteau et al. 2005), despite the high ellipticity of its morphology in both X-ray ($\epsilon \sim 0.27$) and optical ($\epsilon \sim 0.80$) bands (Castagné et al. 2012). Lately, it was found to have a mixed morphology (Lovisari et al. 2017), showing substructures likely produced by minor-mergers, and classified as a non-cool-core (Giacintucci et al. 2017), based on the central entropy value $K_0 = 64 \pm 8\, keV\, cm^2$.

We performed a new study of A1413 with two main goals: (i) to characterize separately the thermal and non-thermal properties of the cluster; (ii) to understand the origin of the radio-emitting electrons through a combined radio and X-ray analysis.

To fulfil these goals, in the initial part of this project, we obtained for the first time the projected thermodynamic quantities of the ICM - like gas temperature and pressure - by a dedicated 2D spectral analysis of archived XMM-Newton observations. This allows us to examine the dynamical state of the cluster. The general properties derived for A1413 suggest that this system is a weak cool core cluster, i.e., not a completely relaxed system.

In the second part of the work, we analyse low frequency radio data of A1413, using new unpublished observations from the LOFAR (LOw Frequency ARrray) Two-meter Sky Survey (LoTSS). Through this analysis, we determine the type and the properties of the extended radio emission hosted by the cluster. We find a radio diffuse emission more extended than previously know and constisting in a superposition of two different sources: the more compact mini-halo emission, at the cluster centre; surrounded by a low-brightness giant-halo on larger scales.

In conclusion, we performed for the first time, a point-to-point correlation between the physical quantities of the thermal emission and the radio surface brightness of A1413 to shed light on the connection between the re-acceleration processes, which give rise to radio emission, and the cluster dynamical state.

This Thesis is organized as follows:

- In **Chapter 1** we illustrate the thermal properties of galaxy clusters, with a focus on the so called “cooling flow" problem.
- In **Chapter 2** we describe the different types of radio emission found in galaxy clusters, and the mechanisms proposed to explain them.
- In **Chapter 3** we present the general picture of A1413, as known by literature studies.
- In **Chapter 4** we describe the procedure followed to reduce and analyze the X-ray data to derive the cluster thermal properties.
- In **Chapter 5** we describe techniques used to obtain the radio images from already reduced and self-calibrated data, and illustrate the cluster non-thermal properties.
- In **Chapter 6** we explore the connection between the thermal and non-thermal emission in A1413 and discuss it in light of other recent literature results.
- in **Chapter 7** we briefly summarize the main results of this Thesis.

Sommario

Gli ammassi di galassie sono i più grandi sistemi virializzati dell'Universo e quindi laboratori ideali per comprendere la formazione e l'evoluzione delle strutture cosmiche. La materia barionica che compone gli ammassi consiste in stelle, galassie e intracluster medium (ICM), plasma riscaldato a temperature di decine di milioni di gradi per via del collasso gravitazionale e con densità di alcune centinaia di particelle per metro cubo, che emette prevalentemente nella banda dei raggi X. Inoltre, osservazioni radio hanno mostrato che l'ICM coesiste con una componente non termica, particelle altamente relativistiche e campi magnetici su larga scala, rivelati per mezzo della radiazione di sincrotrone. Emissione diffusa di sincrotrone nella banda radio è stata trovata sia nelle regioni centrali che periferiche degli ammassi, sotto forma di aloni giganti, mini-aloni, e relitti. Le componenti non termiche sono collegate alle proprietà X degli ammassi e risultano cruciali per una descrizione fisica comprensiva dell'ICM. Studiare la connessione tra lo stato dinamico del cluster e le proprietà dell'emissione radio diffusa è uno dei principali approcci per comprendere l'origine delle particelle relativistiche negli ammassi. Negli ultimi anni, con l'avvento delle nuove generazioni di telescopi radio a bassa frequenza, la classica dicotomia che associa eventi di merger con aloni giganti e sistemi rilassati con mini-aloni, è stata messa in discussione. Contrariamente a quanto comunemente si credeva, emissione radio su vasta scala sono state osservate in ammassi che non mostravano alcun segno di eventi di mergers, mostrando che mergers minori e/o sloshing di densi cool cores potrebbero provocare l'accelerazione di particelle e generare uno spettro di emissione radio ripido.

Questo lavoro di tesi è dedicato al caso peculiare dell'ammasso Abell A1413 (da qui in avanti A1413) che abbiamo scoperto ospitare un'emissione radio non comune. A1413 è un ammasso di galassie massivo ($M_{500} = 5.99^{+0.46}_{-0.45} 10^{14} M_{\odot}$), caldo ($kT = 6.98^{+0.07}_{-0.06} keV$) dell'universo locale ($z = 0.1427$). In origine A1413 è stato classificato come un ammasso rilassato cool-core (G. W. Pratt and Arnaud 2002, Pointecouteau et al. 2005), nonostante l'alta ellitticità della sua morfologia sia nella banda X ($\epsilon \sim 0.27$) che in quella ottica ($\epsilon \sim 0.80$) (Castagné et al. 2012). Successivamente, Lovisari et al. 2017 ha mostrato che A1413 ha in realtà una morfologia mista, con diverse sottostrutture prodotte probabilmente da merger minori, abbinate ad un core abbastanza concentrato. A1413 è stato

poi classificato come non cool-core in un studio di Savini et al. 2019 basato sui valori di entropia centrale, avendo $K_0 = 64 \pm 8 keV cm^2$.

Abbiamo quindi condotto un nuovo studio di A1413 con due principali obiettivi: (i) caratterizzare separatamente le proprietà termiche e non termiche dell'ammasso, (ii) comprendere l'origine delle particelle radio emittenti attraverso uno studio combinato radio e X-ray.

Per conseguire queste finalità, nella parte parte di questo progetto, abbiamo ricavato per la prima volta le quantità termodinamiche proiettate dell'ICM - come la temperatura e la pressione del gas - tramite dedicate analisi spettrali 2D usando osservazioni d'archivio di XMM-Newton, al fine di esaminare lo stato dinamico del gas dell'ammasso. Le proprietà ottenute per A1413 suggeriscono che questo sistema è un ammasso debolmente cool-core, cioè un sistema non completamente rilassato.

Nella seconda parte di questo lavoro, abbiamo analizzato dati di A1413 sull'emissione radio LOFAR (LOw Frequency ARray), utilizzando nuovi dati inediti dalla LoTSS (Lofar Two-meter Sky Survey) survey. Attraverso questa analisi, abbiamo determinato il tipo e le proprietà dell'emissione radio presente in A1413. Abbiamo scoperto una emissione radio diffusa più estesa di quanto precedentemente riportato in letteratura, che consiste in una sovrapposizione di due emissioni: una più compatta emissione centrale di mini alone, circondata da un'emissione di alone su più larga scala.

Infine, abbiamo effettuato per la prima volta, una correlazione punto-a-punto tra le quantità fisiche dell'emissione termica e la brillanza superficiale di A1413 per fare luce sulla connessione tra processi di riaccelerazione, che danno origine all'emissione radio, e lo stato dinamico del cluster.

Il presente lavoro è strutturato come segue:

- Nel **Capitolo 1** illustriamo le proprietà termiche degli ammassi di galassie con particolare attenzione al problema del *cooling flow.*

- Nel **Capitolo 2** descriviamo i differenti tipi di emissione radio e i meccanismi proposti che li generano.

- Nel **Capitolo 3** presentiamo un quadro generale di A1413, come mostrato da studi in letteratura.

- Nel **Capitolo 4** descriviamo la procedura seguita per ridurre e analizzare i dati X e ottenere informazioni utili riguardo l'emissione termica.

- Nel **Capitolo 5** descriviamo la procedura con cui le immagini radio sono state prodotte, da dati precedentemente ridotti e calibrati, illustriamo le proprietà non termiche dell'ammasso.
- Nel **Capitolo 6** abbiamo investigato la connessione tra l'emissione termica e non termica di A1413 e abbiamo discusso quanto ottenuto sulla base di risultati recenti in letteratura;
- Nel **Capitolo 7** abbiamo brevemente sintetizzato i risultati principali di questo lavoro.

Contents

Introduction

Galaxy clusters are the most massive virialized objects in the Universe. They have a size that range from few to several Mpc and typical masses of $10^{13-15}\ M_\odot$. Clusters typically include 10-1000 galaxies (bound together by the cluster self gravity), representing just the 2-5$\%$ of the total cluster mass. The dominant component of galaxy clusters is dark matter ($\sim$ 80-85$\%$) followed by the intracluster medium ICM ($\sim$ 10-15$\%$).

The dark matter component is distributed as halos around the whole cluster and subhalos embedding single galaxies. This component is responsible for the formation and evolution of the clusters. According to the ΛCDM cosmological model, the formation of clusters starts with perturbations in the primordial matter density field. These objects are created as a consequence of the gravitational collapse driven by overdense perturbations of dark matter. These perturbations grow through dark matter dominated gravitational accretion, via hierarchical process of mergers and accretion of smaller structures (e.g., Kravtsov 2012). This model of structures formation is also confirmed by the most recent cosmological simulation, such as the *Millenium Simulation* (Springel 2005) or the *Illustris Simulation* (Vogelsberger et al. 2013).

Most of the galaxies that populate clusters are *early-type* galaxies, i.e. red elliptical and lenticular S0 galaxies. Red sequence galaxies tend to be more concentrated in the central regions of clusters, whereas the less numerous spiral galaxies are predominant in the outer regions. Dressler 1980 showed that there is a correlation between galaxy type populations and the local projected galaxy density: the number density of lenticular S0 and elliptical E galaxies Mpc^{-2} increases, while the fraction of spirals and irregular follows an opposite trend as shown in Fig. 1.

This relation evidences the evolution that galaxies undergo when they fall in the cluster gravitational well from peripheral regions, dominated by gas rich star-forming galaxies, to the cluster central region dominated by early type galaxies poor of gas. Processes responsible for the removal of gas from the galaxies are divided into *internal*, due to galactic winds induced by SN explosions or AGN activities, and *external* mainly originated by the interaction between the ICM and ISM (interstellar medium). In the latter case the gas loss can occur either through thermal conduction of the ICM that heats up the ISM causing its evaporation or via stripping phenomena, that verifies because galaxies, moving thorough the ICM, experience a pressure called *ram pressure* (Gunn&Gott

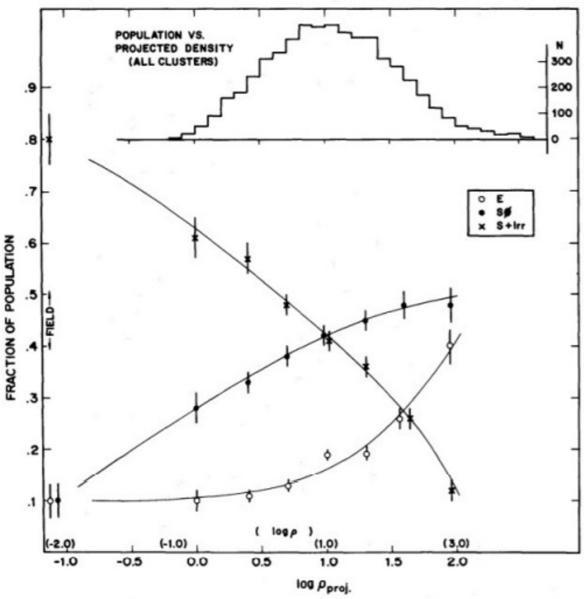

Fig. 1: Fraction of E, SO, and S + I galaxies as a function of the logarithmic projected density, in galaxies per Mpc^{-2}. Data come from 55 clusters studied by Dressler 1980. The histogram shows the number distribution of galaxies in the projected density bins. Credit: Dressler 1980.

1972). In the galaxy outer regions (e.g halos or disks), where the gravitational bound is weak, the ram pressure dominates the gravitational force leading to gas loss. The ICM viscosity also plays a crucial role; indeed friction is responsible for the momentum transfer from the ICM to the ISM (viscous or turbulent ablation). Moreover, regular, compact clusters are often dominated by a single very luminous (cD) galaxy, or by a pair of very bright galaxies. The central cD galaxy has a nucleus of a very luminous elliptical galaxy embedded in an extended low surface brightness halo (Matthews et al. 1964): they are more extended about 60% brighter than the other giant elliptical galaxies.

Observational studies of galaxy clusters have now developed into a broad, multi-faceted and multi-wavelength field. Even if galaxy clusters were first identified in optical band (Abell 1958), as mentioned before, stars in galaxies represent only a few percent of the baryonic mass. Most of the baryons in clusters reside in a hot ICM medium, observed via its X-ray emission (see Chapter 1) and Sunyaev Zel'dovich effect (Matthews et al. 1964). Galaxy cluster are also characterized by emission in the radio band (see Chapter 2), which cannot be ascribed to individual galaxies but is instead associated with the ICM. This radio emission represent impressive feature of the clusters, since it demonstrates thermal ICM is mixed with non-thermal components. The energy density of the relativistic plasma is globally $< 1\%$ than that of the thermal gas (Feretti et al. 2001), but represent an important step in the understanding of the physical processes in galaxy cluster. In fact, the diffuse radio sources are sensitive to the turbulence and shock structures of large-scale environment and provides essential complements to studies at other wavelengths.

X-ray emission in galaxy clusters

Galaxy clusters were first detected as high concentrations of galaxies in the sky. However, in addition to that, there is a host X-ray emitting ICM that accounts for the bulk of the cluster baryons: it represents about 80% of the total baryonic matter in clusters. Cluster of galaxies are indeed very luminous X-ray sources, with typical luminosity ranging between $10^{43} - 10^{46}\ erg\,s^{-1}$.

In this section, the properties of the X-ray gas are first described in Sec. 1.1, then the *cooling flow problem* is explained in Sec. 1.2, together with the characterization of the cool-core galaxy clusters.

1.1 Thermal ICM

The ICM consists of fully ionized hydrogen and helium plus trace of highly ionized heavier elements with a temperature $T \sim 10^7 - 10^8$ K ($1 - 10$ keV) and a particle number densities steeply declining from $n \sim 10^{-2} - 10^{-3} cm^{-3}$ near the centers to $10^{-4}\ cm^{-3}$ in the outskirts. ICM is heated to temperatures of $\sim 10^8$ K during the process of cluster formation (Kravtsov 2012), when the released gravitational energy is transformed into thermal energy.

The X–ray continuum emission from a hot diffuse plasma, such as the ICM, is due primarily to two processes: thermal bremsstrahlung (free–free emission) and recombination (free–bound emission). Processes contributing to X-ray line emission (bound-bound radiation) from a diffuse plasma include collisional excitation of valence or inner shell electrons. For a review, see Böhringer&Norbert 2010.

At the temperatures typical of galaxy clusters ($kT > 3$ keV) the X-ray luminosity from this gas is due to thermal bremsstrahlung, that is the predominant emission process.

Before describing the characteristic of the thermal bremsstrahlung emission, few words about the physical properties of the diffuse plasma need to be outlined.

The time scale for elastic Coulomb collisions between particles in the ICM is much shorter than the age of plasma cooling time, and thus, ions and electrons are assumed to have a Maxwell-Boltzmann distribution. In fact, it can be shown (Spitzer 1956) that electrons will achieve the thermal equilibrium on a time scale given roughly by:

$$t_{eq}(e,e) \approx 3.3 \cdot 10^5 \left(\frac{T_e}{10^8 K}\right)^{3/2} \left(\frac{n_e}{10^3 cm^{-3}}\right)^{-1} \quad yr \tag{1.1}$$

where T_e is the electron temperature and n_e is the electron number density. Instead, the time scale for Coulomb collisions between protons is about

$$t_{eq}(p,p) \approx (m_p/m_e)^{1/2} t_{eq}(e,e), \tag{1.2}$$

which is roughly 43 times longer than that for electrons. After this time, electrons and ions (generally assumed to be protons) would have each a Maxwellian distribution with different temperatures T_i and T_e, respectively. The time scale for the electrons and ions to reach the equilibrium $T_e = T_i$ is $t_{eq} \approx (m_p/m_e)\, t_{eq}(e,e) < 6 \times 10^8$ yr. Since this is shorter than the age of the clusters ($\sim 10^{10}$ yr) the intracluster plasma can be considered as being at single kinematic temperature $T = T_e = T_i$. This result can be understood if one compare the electron and ion mean free path

$$\lambda_e = \lambda_i \approx 23 \left(\frac{T_e}{10^8 K}\right)^{2} \left(\frac{n_e}{10^{-3} cm^{-3}}\right)^{-1} \quad kpc \tag{1.3}$$

with the cluster scales (≈1 Mpc). In fact, for typical values of $T_e \sim 10^8\, K$ and $n_e \sim 10^{-3}\, cm^{-3}$, $\lambda_e = \lambda_i$ are generally much shorter than the clusters size and therefore the ICM can be treated as a collisional fluid, satisfying the hydrodynamic equations.

Since electrons and protons can be considered in equilibrium at a temperature T, we can define the bremsstrahlung emissivity (the emitted energy per unit of time, frequency and volume) at a frequency ν of a plasma with temperature T, electron density n_e, and ion density n_i, as:

$$J_{br}(\nu,T) = 6.8 \times 10^{-38} Z^2 n_e n_i T^{-1/2} e^{-h\nu/kT} \overline{g}(\nu,T) \quad [erg \quad cm^3 s^{-1} Hz^{-1}] \tag{1.4}$$

where the Gaunt factor $\overline{g}(T)$, that includes correction for quantum mechanical distant collisions effects, is a slowly varying function of energy and temperature and is of the order of unity.

As mentioned before, emission lines from the ionized gas composed by H, He and heavy elements (metals) are also contributing to the X-ray emission. Among these, the 7 keV iron line is particularly strong in the cluster X-ray spectrum and can be used for abundance measurements (Mernier et al. 2017).

ICM can be considered to be in hydrostatic equilibrium in the cluster gravitation potential. This assumption is motivated comparing the typical cluster age ($\sim 10^{10}$ yr) with the time required for a sound wave in the ICM to cross a cluster, which is of the order of 10^8 yr. Under the supposition that ICM is locally homogeneous and the cluster is spherically symmetric, the hydrostatic equilibrium reads as:

$$\frac{1}{\rho}\frac{dp}{dr} = -\frac{d\phi}{dr} = -\frac{GM(r)}{r^2} \tag{1.5}$$

where ϕ is the gravitational potential of the cluster, ρ is the gas density and $p = \rho k_B T/\mu m_p$ is the gas pressure, $M(r)$ is the total cluster mass within r, and G is the gravitational constant. Neglecting the gas self-gravity ϕ, then the total cluster mass is:

$$M_{tot}(< r) = -\frac{k_B T r}{G\mu m_p}\left[\frac{d\ln\rho}{d\ln r} + \frac{d\ln T}{d\ln r}\right] \tag{1.6}$$

with k_B is the Boltzmann constant, μ molecular weight and m_p the proton mass. This expression is commonly used to estimate the gravitational mass of the galaxy clusters from X-ray observations, throughout the radial temperature and density profiles spectroscopically determined (Voigt&Fabian 2006).

Fusco-Femiano et al. 2000 tried to model the ICM density and surface brightness on the basis of the ICM X-ray emission. Assuming that the gas has an isothermal equation of state, gas and the galaxies are in equilibrium in the same gravitational potential ϕ. Thus, the galaxy distribution is well described by the empirical King's model (King 1962), and the ICM density radial profile ca be written as:

$$\rho(r) = \rho_0\left[1 + \left(\frac{r}{r_{core}}\right)^2\right]^{-\frac{3}{2}\beta} \tag{1.7}$$

where r_{core} is a measure of the size of the central core and beta is defined as:

$$\beta = \frac{\sigma_r^2}{kT/\mu m_p} \tag{1.8}$$

with σ_r is the line-of-sight velocity dispersion representing the ratio of specific kinetic energies of galaxies and gas. This gas density profile is known as β-model and is used in the X–ray astronomy to model the gas density profile in clusters of galaxies by fitting the surface brightness profile.

In fact, from the density profile it follows that the surface brightness profile observed at a projected radius x is:

$$\Sigma(x) = \Sigma_0\left[1 + \left(\frac{x}{r_{core}}\right)^2\right]^{1/2-3\beta}. \tag{1.9}$$

The model outlined above predicts that the gas density rises towards the cluster center, as expressed by equation (eq. 1.7). Since the bremsstrahlung emissivity depends on the square of the gas density, in the cluster central regions one expect an enhancement

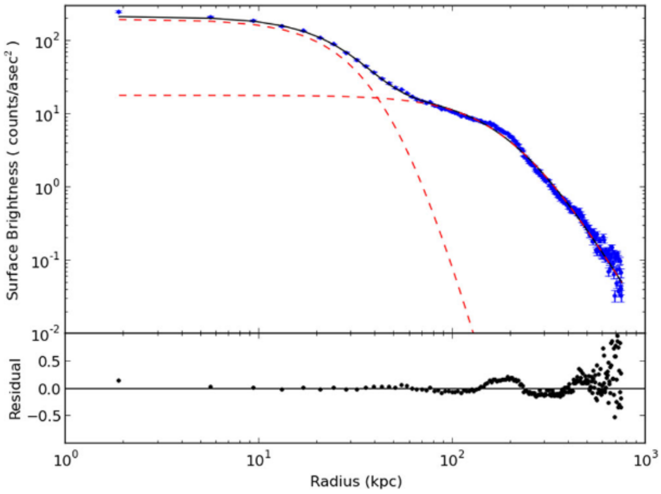

Fig. 1.1: Surface brightness profile of the galaxy cluster MS 0735.67421 fitted with a double β-model. The blue points show the observed surface brightness profile, while the solid black line is the best fit obtained from the double β-model. The dashed red lines show the individual components of the double β-model. Credit: Vantyghem et al. 2014

of the X-ray emission with a consequent cooling of large amount of gas. Loosing its thermal energy, the gas naturally flows into the center of the cluster, forming the so-called *cooling flows* phenomena.

Although the β-model in equation (eq. 1.9) predicts the increase of emissivity in the cluster central regions, some objects show a strong excess in the center of the surface brightness compared a fitted with a single β-model to the outer regions (for example, see the surface brightness profile of MS 0735.67421, in Fig. 1.1). This central excess emission can be qualitatively described by the double β-model (LaRoque et al. 2006):

$$\Sigma = \Sigma_{01}\left[1+\left(\frac{x}{r_{core1}}\right)^2\right]^{-3\beta_1+1/2} + \Sigma_{02}\left[1+\left(\frac{x}{r_{core2}}\right)^2\right]^{-3\beta_2+1/2} \tag{1.10}$$

1.2 Cooling flows and cool core clusters

Evidences of cooling flows in clusters can be found in the X-ray surface brightness distribution which show a sharply peaked emission in the central regions, where the gas density increases rapidly. The fraction of clusters with a central surface excess with respect to a β-model is considerable, so that it is usual to denote this category as *cool-core clusters*. This type of clusters are about 90% of X-ray selected clusters with total mass $M_{tot} \geq 10^{14} M_\odot$, and about 50% of X-ray selected clusters with total mass $M_{tot} \leq 10^{14} M_\odot$.

The cooling flow phenomenon in the cool clusters occurs as the cooling time t_{cool} over which the ICM radiates away a significant fraction of its energy, is smaller than the time for which the cluster has been completely relaxed. This is true at least in the cluster central region, where the density is sufficiently high to speed up the gas lose of energy. The cooling time is calculated as the time taken for the gas to radiate its enthalpy per unit volume H_ν:

$$t_{cool} \approx \frac{H_\nu}{n_e n_H \Lambda(T)} = \frac{\gamma}{\gamma - 1} \frac{kT}{\mu X n_e \Lambda(T)} \tag{1.11}$$

where $\gamma = 5/3$ is the adiabatic index, $\mu \approx 0.6$ is the molecular weight; $X \approx 0.71$ is the hydrogen mass fraction; $\Lambda(T)$ is the cooling function (Sutherland&Dopita 1993). The key feature of the relation (eq. 1.11), is that the cooling time is inversely proportional to the electron density so that the cooling rate increases as the distance from the cluster center decreases.

Irradiating its energy the gas increases its density to maintain the pressure required to support the weight of the overlying gas in the cluster outskirts where the cooling is less efficient, causing a slow subsonic inflow of material towards the cluster center and a further increases of the central density. This process is known as *cooling flow*. The *cooling region*, delimited by the so called *cooling radius* r_{cool}, is defined as the radius at which t_{cool} is equal to the look-back time to $z = 1$, that is $\sim 7.7 \times 10^9$ yr. The cooling region of cool core clusters usually occupies the inner $\sim 100 kpc$, or 10% or the virial radius (McDonald et al. 2018).
The amount of matter that crosses the border r_{cool} in the unit of time $\dot{M}$ is called the *mass inflow rate*. Typically this is of the order of $\sim 100 M_\odot yr^{-1}$ (Fabian et al. 1994) and can be estimated from the X-ray imaging using the luminosity associated to the cooling region L_{cool} due the radiation of the total thermal energy E_{th} of the gas plus the work done on the gas within the cooling region:

$$L_{cool} = dE_{th} + pdV = \frac{\gamma}{\gamma - 1} pdV \tag{1.12}$$

since $pdV = (\rho kT dV)/(\mu m_p) = (dMkT)/(\mu m_p)$ with $\gamma = 5/3$, one obtains:

$$L_{cool} = \frac{5}{2} \frac{\dot{M}}{\mu m_p} kT \tag{1.13}$$

where T is the temperature of the gas at r_{cool}. Usually L_{cool} ranges between $10^{42} - 10^{45}$ $erg\ s^{-1}$, accountig for the 10% of the total cluster luminosity. Value of $\dot{M} \sim 100 M_\odot yr^{-1}$ are typical for the cluster cooling flows.

However, the current generation of high resolution spectral observation X-ray satellites, *Chandra* and *XMM-Newton*, has shown the absence or weakness of the soft X-ray line Fe XVII, revealing that the amount of gas cooling radiatively below about one-third of its original temperature is ten time less than expected (Arnaud&Evrard 1999). This discrepancy represents the so-called *cooling-flow problem* for the cool cluster (McNamara&Nulsen 2007).

The cooling flow problem is commonly addressed following two different approaches: either the normal signatures of the radiative cooling below 1-2 keV are somehow suppressed, for example because of absorption or inhomogeneous metallicity, or there must be an energy-injection mechanism responsible for the ICM heating. In the latter case, processes associated with the central relativistic AGN outflows appears to be the most promising solution.

1.2.1 AGN feedback

All galaxy clusters host a *brightest cluster galaxy* (BCG) in its center, which is defined as the brightest galaxy in a galaxy cluster with typical masses of $M \sim 10^{12} M_{\odot}$ and luminosities $L \sim 10^{12} L_{\odot}$. The *Active Galactic Nuclei* of the BCGs and their activities represent the most accredited solution to the cooling flow problem. The central dominant galaxies of cool core clusters have a large impact on the cluster radio activity. The importance of the radio galaxies in cool cores comes to the light with the X-ray satellite ROSAT which observed a deficit of the Perseus and Cygnus A X-ray emission enhancing the synchrotron emission. *Chandra* and *XMM-Newton* further confirmed the profound connection between the ICM and the central radio sources, showing that the central hot gas of many cool core systems is not smoothly distributed with the cluster radius, but rather present cavities approximately coincident with the lobes of extended radio emissions related to AGN processes. Comparison of radio images having similar resolution to that of Chandra and XMM-Newton, has shown that jets from the central dominant elliptical are responsible for the emission of outwards bipolar flows which are inflating lobes of radio-emitting plasma. These lobes push away hot X-ray radio emitting gas, excavating depressions in the ICM which are detectable as "cavities" in the X-ray images.

Cavities consist in approximately elliptical X-ray surface brightness depressions, 20% to 40% below the level of the surrounding gas. During its initial stage, the tip of a radio jet advances supersonically into the surrounding medium until the radio lobes reach pressure balance with the surrounding hot ICM; while in the initial stage the cavity created by the tip of the jet might be long and narrow (thus making it difficult to detect), when the pressure within a radio lobe becomes comparable to the ram pressure of the jet it is possible that the cavity acquires a roughly spherical form. The scenario is shown in Figure 1.2.

Combined studies of cavities reported in Gitti et al. 2012 shed light on the AGN feedback mechanism. The emerging picture is that bipolar outflows produced by the BCG core inflate large bubbles while driving weak shocks, heating the ICM and inducing a circulation of the gas on hundreds kpc scale.

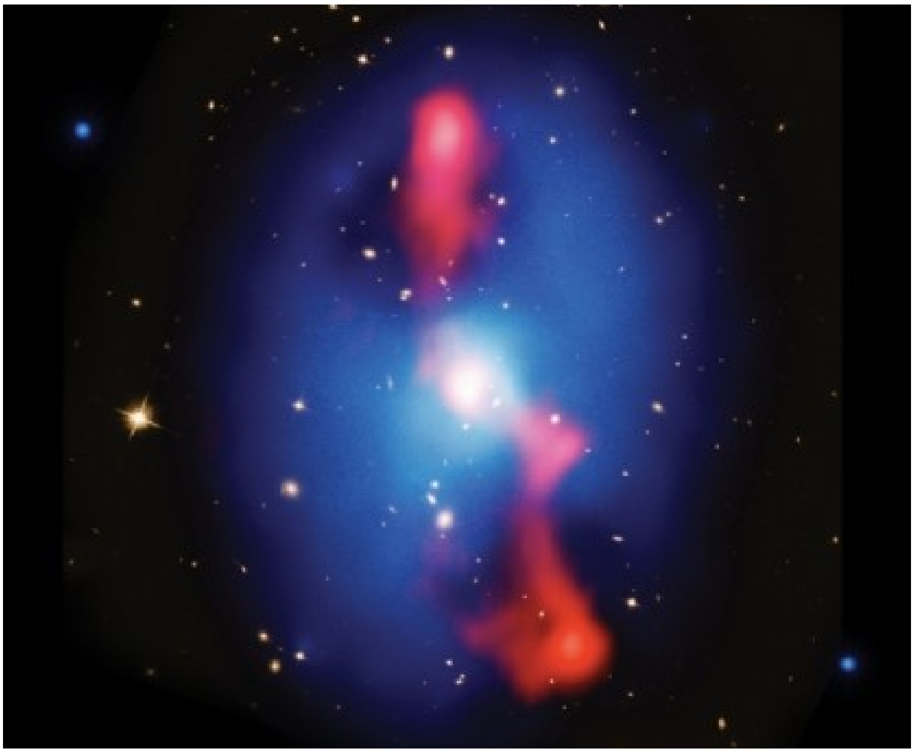

Fig. 1.2: Deep Chandra X-ray image and VLA 330 MHz radio image, superposed to the Hubble Space Telescope optical image of the GC MS0735. The image shows an example of radio lobes (red) which fill X-ray cavities (blue). Credit: Gitti et al. 2012

1.2.2 Cavity Heating

To see how the cavities influences the ICM heating, it is important to compare the power produced by the AGN outburst in the cavities with the cooling luminosity of the X-ray emission. The energy necessary to create a cavity with pressure p and volume V is the sum of the work done by the jet to displace the X-ray emitting gas pV and the internal energy of the lobes:

$$E_{cav} = E_{int} + pV = \frac{\gamma}{\gamma - 1} pV \tag{1.14}$$

with γ the ratio of the specific heats of the cavity content. Assuming the cavity is dominated by relativistic plasma, $\gamma = 4/3$ and $E_{cav} = 4pV$. It is important to notice that the product of the volume and the pressure is directly estimated by X-ray observations of the cavity size and of the temperature and density of the surrounding ICM. Cavity diameters range from less than 1 kpc to approximatelu 200 kpc, with typical values around 20-30 kpc. Studies of samples of X-ray cavities show that their energies range between $10^{55} - 10^{61}$ erg (see Diehl et al. 2008)

To derive the "cavity power" one should estimate the cavity age t_{cav} which can be estimate in three possible ways, as proposed by Bîrzan et al. 2004:

- If a cavity rises through the ICM with a speed equal to the local sound speed then the age of the cavity at distance R from the cluster center is the sound crossing

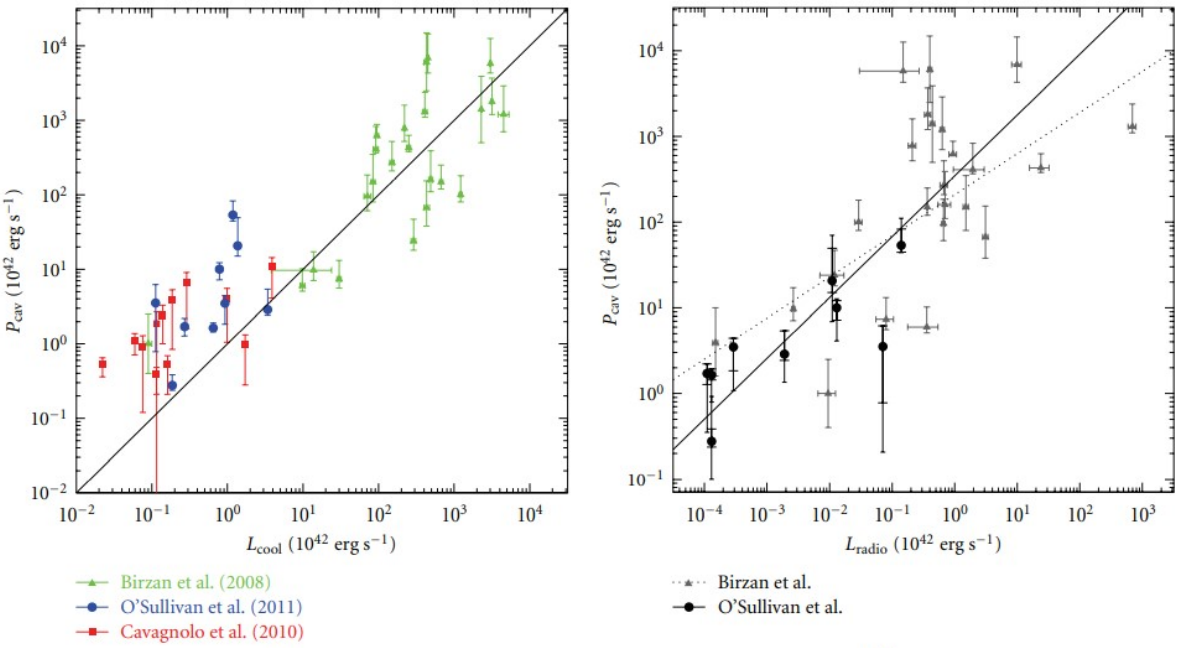

(a) (b)

Fig. 1.3: (a) Cavity power of the central AGN versus the X-ray luminosity in the cooling region. Different symbols refer to different samples. The diagonal line has equation $P_{cav} = L_{cool}$. (b) Cavity power of the central AGN vs the integrated 10 MHz-10GHz radio power L_{radio} for the cool core clusters in the sample of Bîrzan et al. 2008. The solid fit line indicates the regression fit to the data points calculated by O'Sullivan et al. 2011. The dotted line indicates the relation found by Bîrzan et al. 2008. Credit: Gitti et al. 2012

time $t_s = R/c_s$, with $c_s = \sqrt{\gamma kT/\mu m_p}$

- by assuming that the cavity is buoyant and move outwards at the terminal velocity v_t, the cavity age is the buoyancy-time $t_{buoy} \approx 3R/(4\sqrt{2gr})$ where r is the cavity radius and g is the gravitation acceleration at distance R from the cluster center;
- If the time required for the gas to refill the displaced volume of the cavity is considered, then the cavity age can be computed as $t_r \approx 2\sqrt{r/g}$.

Typically these three ages agree within a factor of 2-3 and are of the order of 10^7 yr (Gitti et al. 2012). At the end the cavity power can be simply estimated as $P_{cav} = E_{cav}/t_{cav}$ that, for a relativistic gas with the buoyancy-time as the cavity age, is given by $P_{cav} = 4pV/t_{buoy}$. Figure 1.3(a) shows the comparison between the cavity power P_{cav} and the luminosity inside the cool core region L_{cool} for three samples of galaxy groups from Cavagnolo et al. 2010. It is evident the linearity between the two, supporting the idea of *self-regulated feedback loop*: the active galactic nucleus is fueled by a cooling flow that is itself regulated by feedback from the AGN; the radiative losses from the thermal ICM are balanced by mechanical heating from the central AGN over the system lifetime. This mechanism should somehow be fine-tuned: on one hand the heating mechanism is expected to be enough efficient to offset the radiative cooling and thus to prevent high mass inflow rates (in contradiction with the observation), on the other hand, a too high heating contribution would imply cooling times exceeding the Hubble time, which is in conflict with the observed high fraction of short cooling times.

Another way of estimating the AGN energy release of energy, is based on radio observations avoiding the problem of cavity detectability in shallow X-ray images. Bîrzan et al. 2008 performed a study of a sample of galaxy clusters and derived the relation between the cavity power and the integrates 10 MHz-10 GHz radio luminosity. In particular the integrated radio luminosity estimated from the source spectral index is considered by these authors as superior cavity power indicator compared to estimates at a single frequency.

Figure 1.3b shows the relation between the cavity power and the integrated radio luminosity L_{radio} for the combined sample. The best fitting power-law is:

$$\log P_{cav} = 0.71(\pm 0.11) \log L_{radio} + 2.54(\pm 0.21) \tag{1.15}$$

where P_{cav} and L_{radio} are in units of $10^{42} erg\ s^{-1}$.

Non-thermal radio emission in galaxy clusters

A growing number of galaxy clusters appear to host diffuse extended radio sources, which have no optical counterpart and no obvious connection to the cluster galaxies, and are therefore associated with the ICM. This kind of emission is generally divided into three main classes, known as Giant Radio Halos, Mini-Halos and Relics based on their morphology, properties and location within the clusters. This non-thermal component is detect throughout synchrotron emission, revealing the presence of highly relativistic particles and large-scale magnetic fields. The origin of the radio-emitting electrons is still debated and different models have been proposed (see e.g. vanWeeren et al. 2019, Brunetti&Jones 2014 for recent reviews).

In this section, the origin of the radio emission is first described in section 2.1, together with the proposed models. Then, in section 2.2 and section 2.3 the different classes of radio emission, of interest for this work, are better described. Eventually, the most known and useful relation are presented in section 2.5.

2.1 Origin of the emission

2.1.1 Synchrotron emission - basic concepts

Radio observations prove the existence of relativistic particles (cosmic rays, or “CRs") and ICM magnetic field producing extended non-thermal synchrotron emission up to cluster-scale.

The synchrotron emission is generated by the helicoidal accelerated motion of relativistic particles along the magnetic field line (see e.g. Thomas L. Wilson 2013, Longair 2011 for more details). The power emitted by a single particle with charge e and the mass m that moves with a velocity $\mathbf{v}$ in a (homogeneous) magnetic field with flux density $\mathbf{B}$ is given by the Larmor’s formula, which for a relativistic $\gamma \gg 1$ particle becomes:

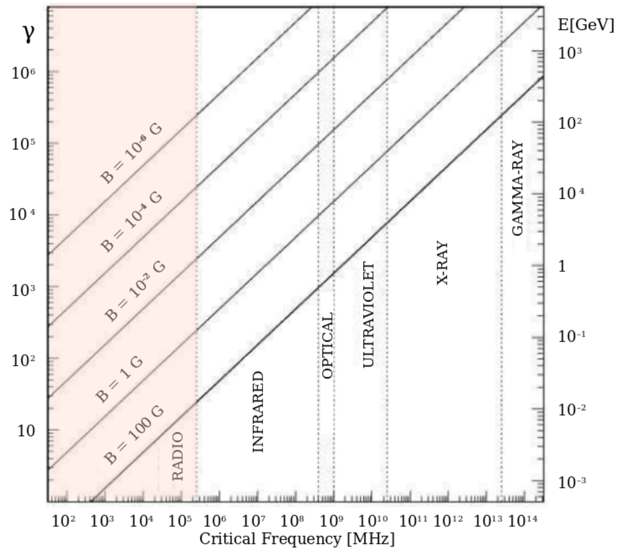

Fig. 2.1: Electron Lorentz factor $\gamma = E/m_e c^2$ (left-hand axis) and energy (right-hand axis) vs. synchrotron critical frequency for magnetic field strengths in the range $10^{-6} - 10^2\,G$. Credits: Govoni&Feretti 2004

$$-\frac{dE}{dt} = \frac{2e^2B^2}{3m^2c^3}\gamma^2 sin^2\theta = 2c\sigma_T\gamma^2 u_B sin^2\theta \quad [\mathrm{erg\,s^{-1}}] \tag{2.1}$$

where $u_B = B^2/8\pi$ is the magnetic energy density, $\sigma_T = 6.65{\cdot}10^{-25}\,cm^2$ is the Thomson cross section, $\gamma = E/mc^2$ is the Lorentz factor and θ is the so-called Pitch angle[1].

The characteristic frequency of an emitting particle is given by:

$$\nu_c = 4.2 \cdot 10^{-9}\,\gamma^2\,\frac{B}{\mu G} \quad [GHz] \tag{2.2}$$

The higher the magnetic field strength, the lower the electron energy needed to produce emission at a given frequency, and vice-versa. In a magnetic field of about B $\sim 1\mu$G, a synchrotron radiation detected for example at 100 MHz, is produced by relativistic electrons with $\gamma \sim 5 \cdot 10^3$ (see Fig. 2.1).

The total monochromatic emissivity of a generic population of electrons with a power-law energy distribution[2] $N(E) = N_0\,E^{-\delta}$, is equal to

$$J_\nu \propto N_0 B^{\alpha+1}\nu^{-\alpha} \tag{2.3}$$

where the spectral index $\alpha = (\delta - 1)/2$ is a direct measure of the electrons distribution and, since the flux density $S(\nu) \propto J(\nu)$, it is also the slope of the spectral energy distribution (SED). Thus, the synchrotron spectrum, emitted by electrons with a power-law energy distribution, in regions which are optically thin to their own radiation, is a power law itselfs $S_\nu \propto \nu^{-\alpha}$.

Moreover, a distinctive characteristic of synchrotron emission is that the radiation is linearly polarized, with a degree of intrinsic linear polarization, for a homogeneous

---

[1] i.e. the angle between the particle's velocity vector and the magnetic lines.

[2] From empirical evidence, cosmic ray data show that $N(E)$ is well described by a power law spectrum

and isotropic distribution of relativistic electrons with a power-law spectrum is (Govoni&Feretti 2004):

$$P = \frac{3\delta + 3}{3\delta + 7} \tag{2.4}$$

Generally speaking, for typical values of the particle spectral index, the intrinsic polarization degree could reach $\sim 75 - 80\%$, but in practice, the polarization degree detected in radio sources is much lower than expected by the above equation. A reduction in polarization could be due to a complex magnetic field structure whose orientation varies with depth in the source (Sokoloff et al. 1999).

Actually, extended radio sources in galaxy clusters are typically unpolarized or polarized up to a few percent, with different percentages for different types of the radio emission.

2.1.2 Energetic losses

It is evident from eq. 2.1 that $-dE/dt \propto m^{-2}$ more massive particles radiates less energy than the less massive ones, under the same condition of magnetic field and energy. Thus, the CR electrons (CRe), with a mass about three order of magnitude smaller[3] than CR protons (CRp), are the main responsible for the observed sychrotron radiation. At the same time, eq. 2.3 shows that the more energetic the CRe are, the more efficiently they emit, i.e. loose energy, ending up to populate the low frequency spectrum. The electron energy halves after a characteristic time t^*

$$t^* = \frac{5.1\,10^8}{\gamma_0 B_\perp^2} \quad s \tag{2.5}$$

which can be considered the particle lifetime: inversely proportional to the initial particles energy $\gamma_0 = E_0/m_e c^2$ and the magnetic field strength[4] $B_\perp^2$. Again, for B $\sim 1\mu$G and $\gamma \sim 5 \cdot 10^3$, the characteristic time t$^* \sim 10^9$ yrs.

These losses lead to the so-called *spectral ageing*: the steepening or cut-off of the synchrotron spectrum for frequencies greater than the so-called break frequency ν^* depending on whether new particle are continuously injected or not, respectively. In particular, eq. 2.3 becomes $J_\nu \propto \nu^{-(\alpha+0.5)}$, $\nu > \nu^*$.

In addition to ageing only due to synchrotron losses, the presence of the cosmic microwave background (CMB), produces an Inverse Compton (IC) emission and thus additional IC losses must be taken into account. The IC emission is due to the relativistic electrons scattering the photons of the CMB: in this process low-energy photons are upscattered (i.e. gain energy) by relativistic electrons. The sum of both effects on electrons

---

[3] $m_e = 9.11\,10^{-28} g$ vs $m_p = 1.66\,10^{-24} g$

[4] $B_\perp^2 = 2/3 B^2$ in the isotropic case

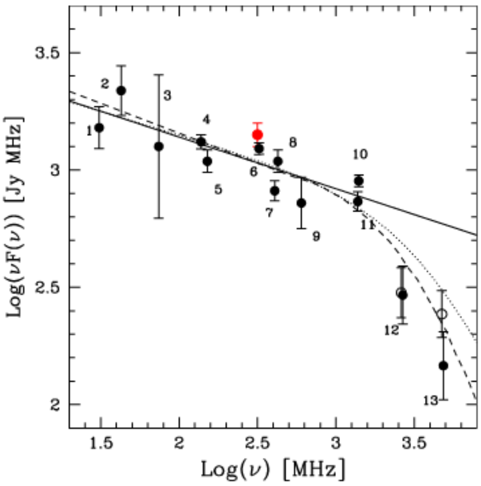

Fig. 2.2: Observed spectrum of the Coma radio halo (black data-points) and the power law ($\alpha = 1.22 \pm 0.04$) that best fits the spectrum at lower frequencies, $\nu \leq 1.4$GHz (solid line). The dotted line is a synchrotron model assuming a broken power-law energy distribution of the emitting electrons, while, the dashed line is a synchrotron model assuming a power-law ($\alpha = 0.75$) with a high energy cut-off, which occurs for instance in (homogeneous) re-acceleration models. Credits: Brunetti et al. 2013

gives rise to a time-scale of

$$\tau_{sync+IC} = 3.2 \cdot 10^{10} \frac{B^{0.5}}{B^2 + B_{CMB}^2} [(1+z)\nu^*]^{-0.5} \quad yrs \tag{2.6}$$

where the break frequency ν^* is in MHz, and the magnetic field in μG, with B_{CMB} the equivalent magnetic field strength of the CMB at redshift z, defined as $B_{CMB}[\mu G] = 3.25(1+z)^2$.

An example of extended radio emission in clusters of galaxy is that of Coma cluster (Fig. 2.2), which shows also a clear steepening in its SED.

Diffuse cluster radio emission typically has a steep spectral index, ranging between $1 < \alpha < 1.5$ (vanWeeren et al. 2019). As mentioned before, due to the energy losses, the initial power-law spectrum steepens beyond a break frequency $\nu > \nu^*$, whose position is related to the time since acceleration.

For relativistic CRp, the main channel of energy losses in the ICM is instead provided by inelastic proton-proton collisions with thermal protons. In this case the radiative time-scale is:

$$\tau_{pp} = \frac{1}{c\, n_{th} \sigma_{pp}} \tag{2.7}$$

where n_{th} is the thermal plasma protons number density and σ_{pp} is the inclusive p–p cross-section.

Fig. 2.3 shows the (total) time scales for losses of CRe and CRp. Even though their contribution to the extended radio emission is negligible, CRp with energy 1 GeV – 1 TeV are long-living particles with life-times in the cores of galaxy clusters of ∼ several Gyrs. CRe, instead, are short-lived particles at the energies where they radiate observable emissions. The maximum life-time of CRe, is about 1 Gyr, at energies ∼100 MeV, while CRe with energy of several GeV, that emit synchrotron radiation in the radio band

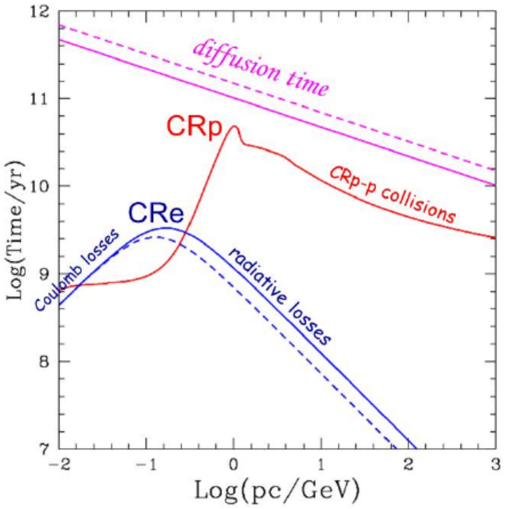

Fig. 2.3: Life-time of CRp (red) and CRe (blue, lower curves) in the ICM at redshift z = 0, compared with the CR diffusion time on Mpc scales (magenta, upper curves) (adapted from Blasi et al. 2007). The most relevant channels of CR energy losses at different energies are highlighted in the panel. Adopted physical parameters are : $n_{th} = 10^{-3} cm^{-3}$,$B =$ 1 (solid) and 3μG (dashed). Diffusion is calculated assuming a Kolmogorov spectrum of magnetic fluctuations. Credits: Brunetti&Jones 2014

(GHz), have shorter life-times (∼0.01-0.1 Gyrs).

2.1.3 Cluster Magnetic Field

Like most astrophysical objects, galaxy clusters are permeated by magnetic fields, and the strongest evidence for the presence of cluster magnetic fields comes from radio observations.

The origin of magnetic fields in galaxy clusters remains unclear (e.g. review of Dolag et al. 2008, Ferrari et al. 2008). It has been suggested that they are of *primordial origin* (Grasso and Rubinstein 2001), i.e., magnetic fields would be already present at the onset of structure formation, and would be a remnant of the early Universe. In this case, a seed field that has formed prior to recombination is subsequently amplified by compression and turbulence. Alternatively, it has been proposed that the magnetic field is of *proto-galactic origin,* i.e. generated during the initial stages of the structure formation process, during the protogalaxy formation (Kulsrud et al. 1997). Another option is the *galactic origin*: galactic winds (Voelk&Atoyan 2000) or active galactic nuclei (AGN) ejecta (Furlanetto&Loeb 2001) can produce magnetic fields and pollute the proto cluster region.

Even if their origin is still debated, radio observations of galaxy clusters allow to measure ICM fields and test the different theories on their origin (Govoni&Feretti 2004). In the following, the most used methods are described.

Faraday rotation analysis of radio sources in the background or in the galaxy clusters themselves is one of the key, although indirect, techniques used to obtain information on the cluster magnetic fields. In fact, the presence of a magnetised plasma between an observer and a radio source changes the properties of the polarised emission from a radio source: Faraday effect rotates the plane of polarisation of the radio emission as it passes through the magnetised and ionised intracluster medium, by an angle:

$$\Delta\Phi = \Phi_{obs} - \Phi_{int} = \lambda^2 \mathrm{RM} \tag{2.8}$$

where Φ_{int} the intrinsic polarisation angle, Φ_{obs} is the polarisation angle observed at a wavelength λ and the rotation measure (RM) is related to the thermal electron density n_e, the magnetic field along the line-of-sight $B_{\|}$, and the path-length L through the intracluster medium according to

$$\mathrm{RM} = 812 \int_0^{L_{[kpc]}} \frac{n_e}{cm^{-3}} \frac{B_{\|}}{\mu G}\, dl \quad [rad\, m^{-2}] \tag{2.9}$$

Since only the magnetic field component along the line-of-sight is measured, the results depend on the assumed magnetic field topology.

Many high quality RM images of extended radio galaxies are now available in the literature (see e.g. the review by Carilli&Taylor 2002). These data are consistent with magnetic fields of a few μG throughout the clusters (e.g. Bonafede et al. 2010). Moreover, stronger fields exist in the inner regions of strong cooling core clusters, with values exceeding $\sim 10\mu$G (e.g. in the inner region of Hydra A, a value of $\sim 35\mu$G was deduced by Taylor et al. 2002).

Another possible way is using minimum energy assumption to estimate an equipartition magnetic field (Beck&Krause 2005). To derive it, it is necessary to assume that the total energy content, which is the sum of the energy in relativistic particles (U_{el} in electrons and U_{pr} in protons) and the energy in magnetic fields (U_B) is minimized:

$$U_{tot} = U_{el} + U_{pr} + U_B \tag{2.10}$$

where the energy contained in the heavy particles U_{pr} can be related to U_{el} assuming $U_{pr} = kU_{el}$ and with k that depends on the mechanism of (re-)acceleration of electrons, whose physical details, are still unknown. Thus, a typical value of $k = 1$ is adopted for extended radio source. The magnetic field energy contained in the source volume V is given by $U_B = (B^2/8\pi)\Phi V$. So, another important assumption of this method relates to the value of the filling factor, i.e. the fraction of the source volume V occupied by magnetic field and relativistic particles. It is usually considered that particles and magnetic fields occupy the entire volume, i.e. $\Phi = 1$. Finally, the electron total energy can be expressed as a function of the synchrotron luminosity $U_{el} \propto L_{sync} B^{-3/2}$.

As mentioned above, in order to obtain an estimate for the magnetic fields, it is necessary to make some assumptions about how the energy is distributed between the fields and particles. A convenient estimate for the total energy is represented by its minimum value (see Fig. 2.4). The condition of minimum energy is obtained when

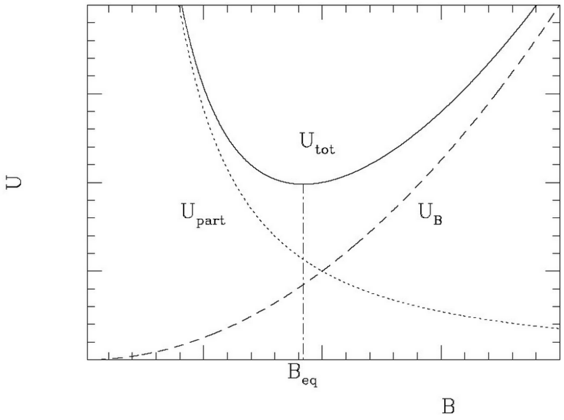

Fig. 2.4: Energy content in a radio source (in arbitrary units): the energy in magnetic fields is $U_B \propto B^2$, the energy in relativistic particles is $U_{part} = U_{el} + U_{pr} \propto B^{-3/2}$. The total energy content U_{tot} is minimum when the contributions of magnetic fields and relativistic particles are approximately equal (equipartition condition). The corresponding magnetic field is the so-called equipartition value B_{eq}. Credits: Govoni&Feretti 2004

$U_B = 3/4(1+k)U_{el}$, i.e. the contributions of the magnetic field and the relativistic particles in the radio emitting regions are approximately equal.

This is the so-called classical *equipartition assumption*, which allows to estimate he magnetic field of a radio source from its radio luminosity L_{sync}.

$$B_{eq} \propto \left[\frac{L_{sync}(1+k)}{\Phi V}\right]^{2/7} \tag{2.11}$$

In this way, magnetic field values in the range 0.1–1 μG are obtained (e.g. Bacchi et al. 2003), consistently with observations (vanWeeren et al. 2019).

Finally, in few cases, clusters containing a radio extended emission show an excess emission, probably due to the IC scattering of relativistic CRe responsible for the radio emission with the CMB photons. In this case, the measurements of the magnetic field strength can be obtained from the ration between the X-ray and radio luminosity. As mentioned in §2.1.2, when the synchrotron radio and IC X-ray emission are produced by the same population of relativistic CRe the total synchrotron and IC powers are related and share the same spectral index α. Since the IC emissivity is proportional to the energy density in the photon field, u_{ph}, whereas the synchrotron emissivity is proportional to the energy density in the magnetic field, $u_B = B^2/8\pi$, a simple proportionality between synchrotron and IC luminosities ca be used

$$\frac{L_{sync}}{L_{IC}} \propto \frac{u_B}{u_{ph}} \tag{2.12}$$

Thus, combining the standard formula of the synchrotron and Compton emission mechanisms, the magnetic field strength B can be easily derived. Using eq. 2.1.3 and assuming $\alpha = 1$, a formula for practical use can be obtained (Carilli&Taylor 2002)

$$B = 1.7(1+z)^2 \left(\frac{S_r\,\nu_r}{S_X\,\nu_X}\right)^{0.5} \quad \mu G \tag{2.13}$$

where S_r and S_X are the radio and X-ray flux densities at observed frequencies ν_r ν_X, respectively. Note that, unlike Faraday rotation measurements, the geometry of the field does not play a critical role in this calculation. The difficulties related to this method are essentially due to the limitations of present X-ray observations in the hard X-ray domain and to the problem of distinguishing between the thermal and the non-thermal X-ray emission. When the IC X-ray emission is not detected from a radio emitting region, only lower limits can be used. Indeed, the upper limit on IC emission translates to a lower limit on the magnetic field strength. For example $B \gtrsim 0.2 \mu G$ for the Bullet Cluster (Wik et al. 2014).

2.1.4 Models of the origin of diffuse sources

Since magnetic fields have been found to be ubiquitous in galaxy clusters (§2.1.3), the crucial ingredient for the existence of diffuse synchrotron radio sources is the presence of relativistic particles $\gamma \sim 10^4$, i.e. GeV energy (vanWeeren et al. 2019). As described in §2.1.2, relativistic electrons undergo energetic losses and have a typical life time $\sim few\, 10^8\, yrs$ (Fig.2.3). The typical diffusion length-scale in the ICM of a GeV electron, using the Bohm approximation, is of the order of 10 pc (e.g. Bagchi et al. 2002).

So, there must be some specific processes to produce synchrotron emitting particles present in the cluster volume and responsible for the diffuse radio emission on cluster scale. Specifically, the radiative lifetime of radio-emitting electrons is much shorter than their diffusion time over cluster scale:

$$\tau_{sync+IC} \sim 2 \cdot 10^8 \left[\left(\frac{B}{1\mu G} \right)^2 + \left(\frac{B_{CMB}}{3.2\mu G} \right)^2 \right]^{-1} \left(\frac{\gamma}{10^4} \right)^{-1} \quad yrs \tag{2.14}$$

$$\tau_{diff} \sim 1.4 \cdot 10^{11} \left(\frac{R}{1Mpc} \right)^2 \left(\frac{\gamma}{10^4} \right)^{-1/3} \left(\frac{B}{1\mu G} \right)^{1/3} \quad yrs \tag{2.15}$$

so, $\tau_{diff} \sim 10^{9-11}, yrs \gg \tau_{sync+IC} \sim 10^8\, yrs$ for typical values of $B \sim \mu G$ (§2.1.3), $\gamma \sim 10^4$ and extension of the emission $R \sim 0.1 - 1\,\mathrm{kpc}$.

This problem is known as the *slow diffusion problem* (Brunetti&Jones 2014): the slow CR diffusion in the ICM is incompatible with the observed size of the radio sources unless the observed CRe are continuously injected or accelerated throughout radio sources volumes. To explain the radio emission on Mpc scale, it is necessary that the relativistic CRe undergo in-situ energization, with an efficiency comparable to the energy loss processes, or be continuously injected into the cluster volume.

Two main classes of models have been suggested for the origin of relativistic electrons: the *leptonic (re-acceleration) model* which predict that relativistic particles are continuously accelerated within the cluster volume (Gitti et al. 2002, ZuHone et al. 2013; Brunetti&Lazarian 2007), and the *hadronic (secondary electrons) model*, in which relativistic electrons are produced through the cluster volume by proton-proton collisions (Pfrommer and T. A. Enßlin 2004; T. Enßlin et al. 2011).

The *re-acceleration model* predicts that the already existing electrons in the cluster volume (e.g. injected by AGN activity or by star formation in normal galaxies - supernovae, galactic winds, etc.) are re-accelerated to maintain their energy to the level necessary to produce the observed synchrotron radio emission in relatively weak magnetic fields ($B \sim \mu G$). There are two main ways that entail the transfer of energy from the cluster ICM to the radiating particles: these are cluster shocks and cluster turbulence, via Fermi I and Fermi II acceleration mechanisms, respectively.

In Fermi I process, particles are accelerated at a shock with the acceleration taking place diffusely. Particles cross back and forward, across the shock front, as they scatter from magnetic inhomogeneities in the shock down and upstream region. At each crossing, particles gain additional energy, forming a power-law energy distribution of CR.

Instead, in Fermi II is a stochastic process where particles scatter from magnetic inhomogeneities, for example from magneto-hydrodynamical (MHD) turbulence. Particles can either gain or loose energy when scattering. But the motions are random, the probability for a head-on collision, where energy is gained, is slightly larger. Because of its random nature, second order Fermi acceleration have a low efficiency.

In a stochastic process, we have $dE/dt \sim E/\tau_{acc}$, combined with the increase of energy at each scatter in Fermi II $dE/dt \sim 2v^2E/\lambda c$, leads to the following re-acceleration time scale

$$\tau_{acc} \sim \frac{\lambda c}{2\,\delta V^2} \sim 10^8 - 10^9\,yrs \tag{2.16}$$

with V the magnetize cloud random velocity and λ the cloud average separation. Thus, assuming rough equipartition between Syn and IC losses (Brunetti & Lazarian 2016) the maximum synchrotron frequency can be calculated as

$$\nu_{max} \sim \left(\frac{\tau_{acc}}{4\,10^8\,yrs}\right)^{-2} \quad GHz \tag{2.17}$$

It is easy to comprehend that, a frequency break around 1 GHz leads to the non-detection of these electrons in the classical frequency range 1.4-5 GHz. At lower frequency, instead, it is possible to observe the emission from less energetic electrons, with a steeper spectrum and visible at 10-100MHz. A good example of that, is the case of A1033 (Fig. 2.5) where observation at lower frequency (right) show the previous "invisile" (right) population of radio emitting electrons.

In the *hadronic model*, secondary electrons are injected as secondary particles (decay products) by inelastic nuclear collisions between the relativistic protons CRp and the

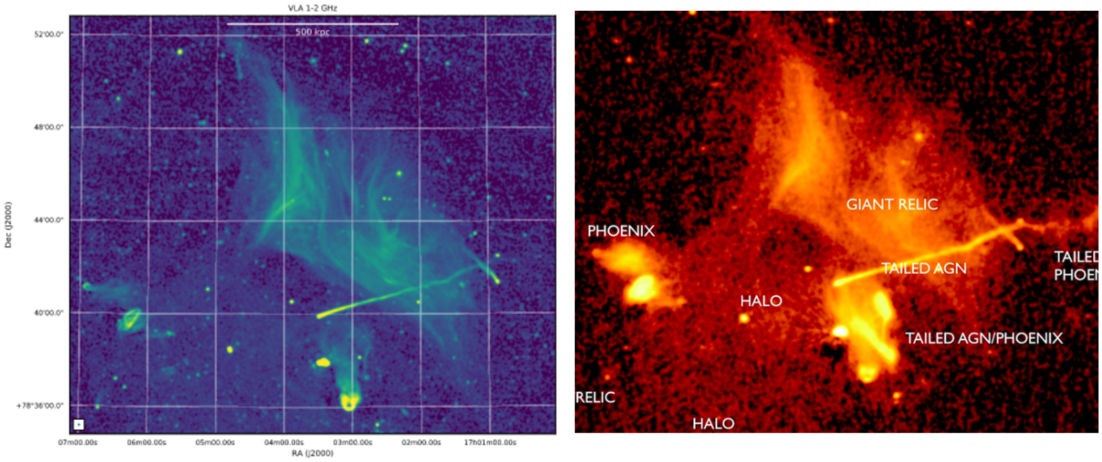

Fig. 2.5: Left: VLA 1–2 GHz image with a resolution of 6 of the radio shock region in Abell 2256 (Owen et al.2014). ; Right: Radio continuum emission at 120-180 MHz of Abell 2256. The resolution is 5 arcsec and the image has a noise about 0.1 mJy/beam

thermal protons in the ICM (e.g. Pfrommer and T. A. Enßlin 2004). The decay chain for the injection of secondary particles is

$$\begin{aligned} p + p &\rightarrow \pi^0 + \pi^+ + \pi^- + \text{other particles} \\ \pi^0 &\rightarrow \gamma\gamma \\ \pi^\pm &\rightarrow \mu^\pm + \nu_\mu(\bar{\nu}_\mu) \\ \mu^\pm &\rightarrow e^\pm + \bar{\nu}_\mu(\nu_\mu) + \nu_e(\bar{\nu}_e) \end{aligned} \tag{2.18}$$

CRp have a very long lifetime compared to CRe (Fig.2.3), because their energy losses are negligible. Hence, they can diffuse on large scales, producing CRe throughout the cluster volume. Possible mechanisms to produce CRp are first order Fermi acceleration at shocks, AGN activity, and galactic outflows (supernovae, winds).

2.2 Giant Radio Halos

Radio halos are centrally located diffuse sources, with an extension comparable to that of the cluster ∼1-2Mpc (see Fig.2.6 *left*). They are typically unpolarized sources, primarily found in dynamically disturbed clusters and show a smooth and regular morphology, with the radio emission approximately following the distribution of thermal ICM. They present magnetic field value of about $\sim 0.1 - 1\mu G$ (Feretti et al. 2012).

Giant radio halos are found only in ∼30% of X-ray luminous and massive clusters (Brunetti et al. 2007, Venturi et al. 2008), with evidence that this fraction depends on cluster X-ray luminosity (Cassano et al. 2008).

The surface brightness of radio halos is faint ($\sim 1 - 0.1\, \mu Jy/arcsec^2$ at 1.4GHz) and characterised by a steep spectrum, with a spectral index $\alpha > 1$ (Feretti et al. 2012).

As explained in §2.1.2 because of the slow diffusion problem CRe must be re-accelerated or continuously injected in the ICM. Two principal mechanisms have been proposed to explain radio emission on Mpc-scales: i) requiring that the emitting electrons are (re)accelerated *in-situ* (for example through merger-generated turbolence in the ICM) or ii) that there is a continuous iniection of secondary electron-positron pairs into ICM, for instance by inelastic hadronic collisions between relativistic and thermal protons (Brunetti&Jones 2014). However, secondary models have some observational problems. For example, an unavoidable consequence of this scenario is the emission of γ-rays due to the decay of π^0 (eq. 2.1.4) that are produced by the same decay chain that is responsible for the injection of secondary CRe (Brunetti&Jones 2014). Models can be constructed to provide a rough measure of the low energy end of the expected γ-ray spectrum (Kelner et al. 2006). Thus, comparison with γ-ray emission (e.g. by using The Fermi-LAT Gamma-ray Space Telescope) can provide an immediate test to the model. Observationally, γ-ray emission from clusters of galaxies were searched for the last several years to decade, but all these attempts resulted in no detection.

Thus, hadronic models are currently disfavoured and turbulent re-acceleration models are considered to explain radio giant halos. The most obvious expectation of this model is a tight connection between giant radio halos and cluster mergers, because of the finite decay time for merger-generated turbulence (Brunetti&Jones 2014). According to this model radio halos could have complex, spatially varying (and potentially very steep) spectra due to the breaks and cut-offs that are produced in the spectrum of the emitting CRe as a result of the balance between (spatially varying) acceleration and cooling.

2.3 Mini-Halos

Radio mini-halos are centrally located diffuse sources, but their emission is limitated to smaller spatial scales $\sim 100-500$ kpc (Fig.2.6 *right*). In common with large-scale halos, have a steep spectrum and a very low surface brightness.

Mini-halos are usually found in relaxed cool core clusters and their size is comparable to that of the central cluster cooling region (Sec. 1.2) r_{cool}. In particular, in a recent work, Giacintucci et al. 2017 determined the occurrence of radio mini halos in a sample of 58 clusters with $M_{500} > 6 \cdot 10^{14}\, M_{\odot}$: they found that 80% of the cool core clusters host mini-halos.

Moreover, cluster hosting mini halos always have central radio-loud AGN exhibiting outflows in the form of radio lobes and bubbles inject CRe into the central region of galaxy cluster (Brunetti&Jones 2014).

As for giant halo, the origin of mini-halo emission is generally attributed to hadronic

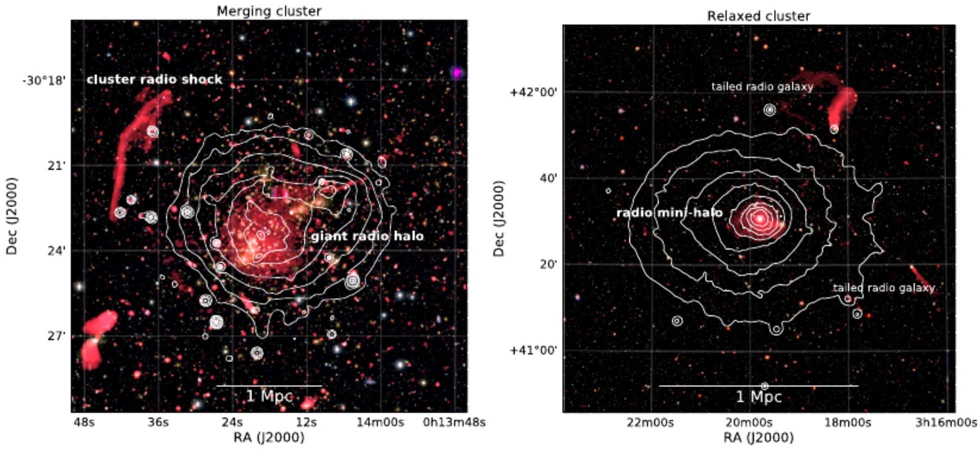

Fig. 2.6: *Left panel*: VLA 1–4 GHz image of the merging galaxy cluster Abell 2744 with different source classes labeled. Chandra X-ray contours are shown in white. This cluster hosts a luminous *giant radio halo* and a cluster radio relic, i.e.*relic*. X-ray surface brightness contour are drawn proportional to [1, 4, 16, 64, . . .]. *Right panel*: VLA 230–470 MHz image of the relaxed cool core Perseus cluster from Gendron-Marsolais et al. (2017). The Perseus cluster hosts a radio mini-halo as well as two prominent tailed radio galaxies. XMM-Newton X-ray contours in the 0.4–1.3 keV band are overlaid in white with the same contour spacing as in the left panel. Credits: vanWeeren et al. 2019

(Zandanel et al. 2015) or turbolent acceleration mechanisms (Gitti et al. 2002, ZuHone et al. 2013); but unlike giant halo, where it is connected to major cluster mergers, here the radio emission should be caused by turbulence confined to core region, induced by gas-sloshing between relativistic and thermal protons, or connected with the central AGN feedback (e.g., Bravi et al. 2016)

Actually, even relatively relaxed clusters have large-scale gas motions in their cores at significant fractions of the local sound speed. The clearest observational signatures of these gas motions are spiral-shaped cold fronts seen in the majority of cool-core clusters. These cold fronts are believed to be produced by the cold gas of the core sloshing in the clusters deep potential well, for example in response to passing dark matter subhalo motions Brunetti&Jones 2014. Those sloshing motions, can advect mass and gas from the cluster core producing a turbulence cascade (ZuHone et al. 2013).

2.4 "Intermediate" or "hybrid" radio halos

In the last years, the advent of low-frequency and deep observations has complicated the picture described above. In fact, a few cooling core clusters show the presence of a diffuse sychrotron halo-like emission that extends quite far from the central classical mini-halo, differently to what is generally observed.

Only a handful of galaxy cluster hosting this kind of sources are found so far, and their classification is somehow ambiguous, but the study of these objects and their connection with thermal and non-thermal gas properties can be a very powerful tool to connect the two main classes of extended sources or even follow their evolution.

A generic scenario proposed by Brunetti&Jones 2014 is that the driven flows and turbulent motion that destroy the ICM cores of cluster during merger could also transport and re-accelerate CRs on large Mpc scales. In this scenario, complex situations where a central mini-halo is embedded in a lower brightness radio emission on larger scales should exist in dynamically "intermediate" systems, such as the case of A2142 (Farnsworth et al. 2013). They detected a ∼2 Mpc radio halo structure, in addition to the smaller, possible MH previously seen (Giovannini&Feretti 2000), in A2142 galaxy cluster, which has a massive cooling flow (Perese et al. 1998) centered on the diffuse radio source. A recent analysis of this cluster was performed by Venturi2017. They argued that the radio halo consists of two components, that show different observational properties: the inner brightest component, with properties similar to that of a mini-halo; the outer larger component, with a steeper spectrum. They proposed that the inner component is powered by central sloshing turbulence. The outer component might probe turbulent re-acceleration induced by a less energetic merger event. Alternatively, the different components are the result from a transition between hadronic and turbulent re-acceleration processes.

Moreover, some peculiar cases, such as CL1821+643 studied by Bonafede2014, show that giant radio halos could exist also in strong cool core cluster, failing to fulfil the classical dichotomy between the two classes of radio emission.

As often has happened, this emission was not detectable before the low frequency radio facilities, such as LOFAR (referenza al capitolo). Among others, is the case of the cluster PSZ1 G139.61+24.20 (z = 0.267), that was previously listed as a candidate minihalo by Giacintucci2017 but Savini2018 discovered a steep-spectrum extended emission well beyond the cool core region of the cluster with LOFAR. They assert that the outer emission could be produced by turbulent re-acceleration from minor merger event that has not disrupted the cool core (as in the case of CL1821+643).

If this scenario is correct, it indicates that both giant and mini halos could co-exist.

2.5 Radio & X-ray Scaling Relations

The evident connection between thermal and non-thermal emission can be further investigated searching for global and point-to-point correlations between thermal and non-thermal components. These studies result in a variety of well known scaling relation and can provide important information on the origin of the non-thermal CR component. In this section the main relation, useful for this thesis work, are explain.

Diffuse radio emission in galaxy clusters is known to be related to cluster mass and cluster dynamical state. High sensitivity survey with GMRT found that clusters with similar thermal X-ray luminosity ($L_{500} > 5 \cdot 10^{44}\, erg\, s^{-1}$), and presumably similar mass, branch into two populations (Fig.2.7, left), one hosting radio halos and a second one with no evidence for halo-type cluster-scale radio emission at the sensitivity level of current observations (radio upper limits considered) (first studies done by Brunetti et al. 2007, Brunetti et al. 2009).

This is the well know $\mathrm{P_{1.4GHz} - L_X}$ relation, concerning the radio power at 1.4GHz of giant halos with the cluster X-ray luminosity. Because the X-ray luminosity and gas temperature of galaxy clusters are tightly related to cluster mass, the relation of $\mathrm{P_{1.4GHz} - L_X}$ indicates that emission of halos is fundamentally related also to cluster mass and thus, a similar relation can be found (e.g. Yuan et al. 2015).

As discussed in section 2.1, in current models, radio halos have origin when CRe in the ICM are re-accelerated by turbulence, injected during merger events. Thus, it is reasonable to believe that the properties of radio halos should be connected to the cluster mass, since it sets the energy budget available for particle acceleration[5], and to the merging history of the host clusters (Cuciti et al. 2021). Being steeper than other halos, ultra-steep spectrum RH(green asterisks) are, in general, under-luminous with respect to this correlation.

The fitting procedure is performed using a power law of the generic form (e.g. as in Cassano et al. 2006, Cassano et al. 2013):

$$log\Big(\frac{P_{1.4}}{10^{24.5} Watt\, Hz^{-1}}\Big) = B\, log\Big(\frac{L_X}{10^{45} erg\, s^{-1}}\Big) + A \qquad (2.19)$$

and the slope of the correlation is $B \sim 2$, depending on different fitting techniques or different way of considering X-ray luminosity (e.g. L_{500}, $L_{[0.5-5keV]}$ etc.) (Cassano et al. 2006, Brunetti et al. 2009).

Related to this finding, another observational milestone that has been achieved in the last decade is the connection between giant radio halos and the dynamics of the hosting clusters, with halos preferentially found only in merging systems (Cassano et al. 2010; Cassano et al. 2013). To provide a quantitative measure of the degree of the cluster disturbance, i.e. define the its dynamical state, three type of morphological X-ray parameter are largely used (e.g.,Lovisari et al. 2017): the concentration parameter c, the centroid shift w and the power ratios $\mathrm{P_3/P_0}$.

- Concentration parameter c
  The concentration parameter has been used in literature for a first identification of cool core clusters in those cases where a spatially resolved spectroscopic analysis

---

[5] The idea is that during a merger event, a fraction of the gravitational energy released, which scales with cluster host mass, is channeled into the re-acceleration of cosmic rays via turbulence (e.g. Cassano et al. 2004)

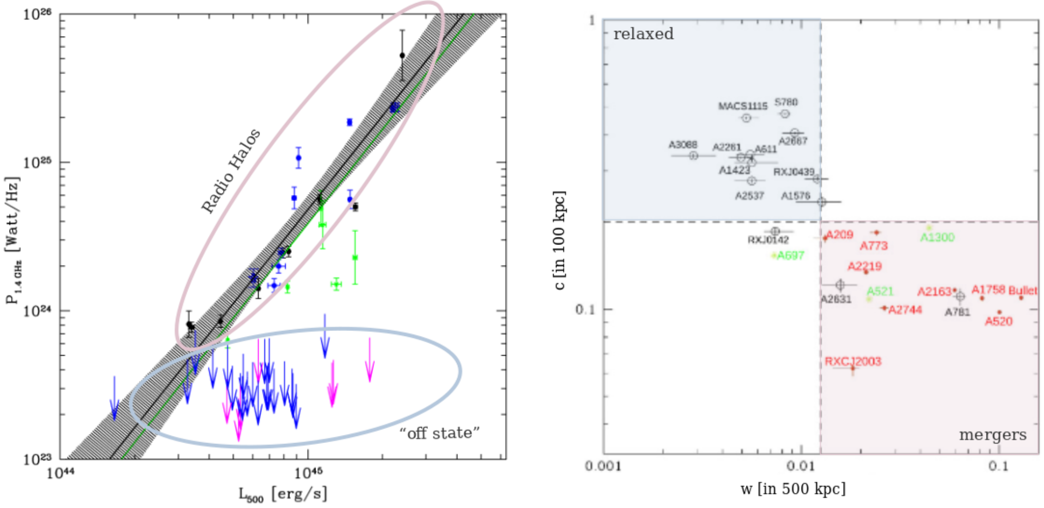

Fig. 2.7: *Left panel*: distribution of galaxy clusters of the GMRT sample in the radio power – X-ray luminosity diagram, showing that clusters branch into two populaitions: giant radio halos (the merging systems) and "off state", undetected, systems (the relaxed systems) (adapted from Cassano et al. 2013). Best-fit relations to giant RHs only (black lines) and to all RHs (including USSRH, green dashed lines) are reported. The 95% confidence regions of the best-fit relations obtained for giant RHs only are also reported (shadowed regions). *Right panel*: distribution of galaxy clusters in the concentration parameter c vs centroid-shift w. Mergers are expected in the bottom-right panel, relaxed systems in the top-left panel. Clusters hosting giant radio halos are reported in red (adapted from Cassano et al. 2013).

was not possible (e.g. in the case of high redshift clusters; Santos et al. 2008). It is defined as the ratio of the peak over the ambient surface brightness SB, as

$$c = \frac{SB(r < 100kpc)}{SB(r < 500kpc)} \tag{2.20}$$

It is used to differentiate galaxy clusters with a compact core (i.e., core not disrupted from a recent merger event) from cluster with a spread distribution of gas in the core (i.e., core disturbed from a recent merger episode).

- Centroid shift w

  The centroid shift is defined as the variance of the projected separation between the X-ray peak determined from the smoothed image (with a Gaussian of FWHM of 6 arcsec) and the centroid of the emission obtained within 10 apertures of increasing radius up to R_{ap}:

$$w = \left[\frac{1}{N-1}(\Delta_i - \langle\Delta\rangle)^2\right]^{1/2} \cdot \frac{1}{R_{ap}} \tag{2.21}$$

where Δ_i is the distance between the X-ray peak and the centroid of the i-th aperture.

- Power ratio P_3/P_0
  The power ratio method is motivated by the idea that the X-ray surface brightness could represent the projected mass distribution of the cluster. The power ratio is a multipole decomposition of the 2D projected mass distribution inside a given aperture R_{ap}
  $$P_m = \frac{1}{2m^2 R_{ap}^{2m}}(a_m^2 + b_m^2) \tag{2.22}$$
  where the moments a_m and b_m are given by
  $$a_m(R) = \int_{R' \leq R_{ap}} SB(x')(R')cos(m\Phi')d^2x' \tag{2.23}$$
  and
  $$b_m(R) = \int_{R' \leq R_{ap}} SB(x')(R')sin(m\Phi')d^2x' \tag{2.24}$$
  Usually, P_3/P_0 is used, that is the lowest power ratio moment providing a clear substructure measure (e.g. Böhringer et al. 2010)

Cassano et al. 2010 showed that, considering the median value of each parameter, $w = 0.012$ and $c = 0.2$, it was possible to separate the sample between *RH merging clusters* ($w > 0.012$ and $c < 0.2$) and *more relaxed clusters without RHs* ($w < 0.012$ and $c > 0.2$), as shown in (Fig. 2.7, right). Diagrams similar to that of Fig.2.7 can be obtained by plotting $w - P_3/P_0$ or $c - P_3/P_0$ (see Cassano et al. 2010).

As described above, traditionally, the radio power is computed at a rest-frame frequency of 1.4 GHz $P_{1.4\,GHz}$ and all correlation studies so far have used this quantity. With the new LOFAR radio halo detections it becomes feasible to study this relation at a rest-frame frequency of 150 MHz, with $P_{150\,GHz}$ given by

$$P_{150\,MHz} = \frac{4\pi D_L^2 S_{150MHz}}{(1+z)^{\alpha+1}} \tag{2.25}$$

with D_L the luminosity distance of the cluster. Analogous statistical studies at lower frequencies with LOFAR were performed by vanWeeren et al. 2020: following Cassano et al. 2013, they used the relation between radio power and cluster mass

$$log\Big(\frac{P_{150\,MHz}}{10^{24.5} Watt\,Hz^{-1}}\Big) = B\,log\Big(\frac{M_{500}}{10^{14.9} M_\odot}\Big) + A \tag{2.26}$$

and found that, there is also a clear correlation between M_{500} and $P_{1.4\,GHz}$ (Fig. 2.8) with a slope of B = 6.13 ± 1.11, steeper than B = 4.51 ± 0.78 obtained at 1.4 GHz for

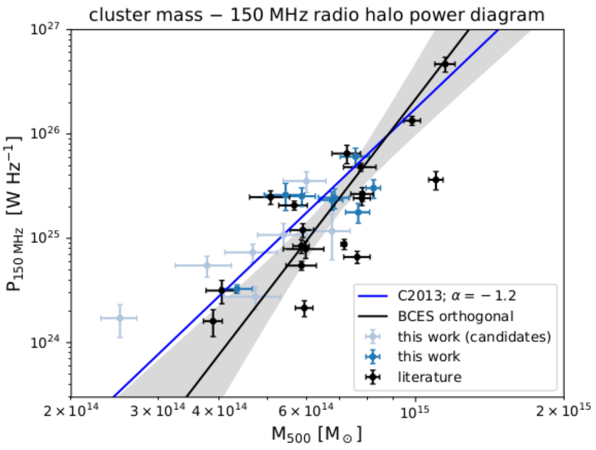

Fig. 2.8: Distribution of clusters in $P_{150\,\mathrm{MHz}} - M_{500}$ plane. The black solid line displays the BCES orthogonal fit (candidate halos were excluded). The shaded region shows the 3σ (99.7% confidence) region of the fit. The blue line is the BCES orthogonal fit from Cassano et al. 2013 scaled with a spectral index of -1.2. Credits: vanWeeren et al. 2020

$P_{1.4\,\mathrm{GHz}} - M_{500}$ by Cassano et al. 2013, but still consistent with that, considering the uncertainties.

Other relations can be performed using the surface brightness profile and the radio emissivity, through the investigation of extended radio sources morphological properties.

The brightness of halo-like diffuse radio sources in clusters of galaxies decreases with increasing distance from the cluster center, eventually falling below the noise level of the radio images. Since, the size of the diffuse low-surface brightness emissions as derived from the 3σ-isophotes seen in the radio images may be strongly affected by the sensitivity of the radio observations, to obtain an unbiased estimate of the size of mini-halos and halos, the azimuthally averaged brightness profile are usually fitted with an exponential(e.g. Orrù et al. 2007, Murgia et al. 2009) of the form:

$$I(r) = I_0 e^{r/r_e} \tag{2.27}$$

where the two independent parameters I_0 and r_e are the central radio surface brightness and the e-folding radius i.e., the radius at which the brightness drops to I_0/e. Thus, the quantity r_e can be used to define a length-scale which is relatively independent on the the signal-to-noise ratio of the radio images.

Through the study of their averaged brightness profiles, Murgia2009 analyzed some of their morphological and physical radio properties (i.e., length-scale, central brightness, and emissivity).

They found that their sample contains radio halos with quite different length-scales (r_e ∼ 70-400 kpc) but, comparing the location of the halo sources in the $\mathrm{I_0} - \mathrm{r_e}$ plane with the dotted lines of constant emissivity, is evident that their emissivity is remarkably similar (I_0 ranges between $0.4 - 3\,\mu Jy/arcsec^2$) from one halo to the other, as shown in Fig. 2.9, right.

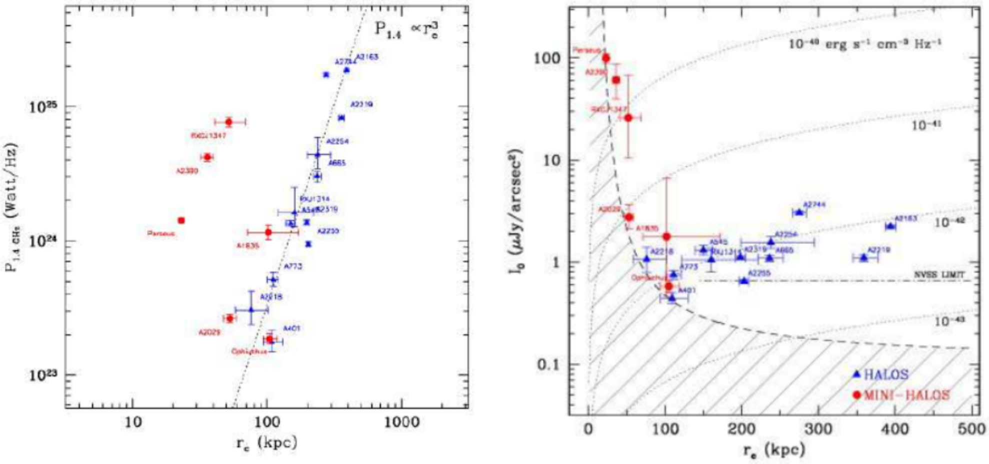

Fig. 2.9: *Left panel:* Radio power at 1.4 GHz versus e-folding radius in kpc for mini-halos (red dots) and halos (blue triangles) for the sample analyzed by Murgia et al. 2009. The dotted reference line represents the expected radio power if one assumes for the emissivity the average value we found for radio halos $\langle J \rangle = 10^{-42}\, erg\, s^{-1}\, cm^{-3} Hz^{-1}$ and for the volume V the volume of a sphere a radius $3r_e : log(P_{1.4}) = 23.52 + 3\, log(r_e/100kpc)$. *Right panel*: Best fit central brightness I_0 $(\mu \mathrm{Jy}/\mathrm{arcsec}^2)$ versus the length-scale r_e (kpc) both for halos (blue triangles) and mini-halos (red dots). The dotted lines indicate regions of constant emissivity, namely 0.1, 1, 10, 100 times the average emissivity of radio halos which is $\langle J \rangle = 10^{-42}\, erg\, s^{-1}\, cm^{-3} Hz^{-1}$. The dot-dashed line represents the 3σ sensitivity level of the NVSS. Credit: Murgia et al. 2009

In contrast, mini-halos span a wide range of radio emissivity (Fig. 2.9, right), with values more than 100 times greater than that of radio halos. By comparing the location of the mini-halo sources in the $\mathrm{I}_0 - \mathrm{r}_e$ plane with the lines of constant emissivity is clear that, although some mini-halos (like Ophiuchus and A1835) are quite comparable to the halo sources, they appear generally separated from the halo sources, showing a larger spread in radio emissivity. So, there is a tendency for the smaller mini-halos of the sample to have a higher central brightness, but this trend must be considered carefully, because a selection effect may be present.

A further investigation can be done by studying the trend of the radio power versus the e-folding radius of mini-halo and halos (Fig. 2.9, left). Murgia et al. 2009 found indeed a tight correlation between the radio power and the e-folding radius of radio halos, with radio power increases as $P_1 1.4 \propto r_e^3$. Even though this separation into two distinct groups in this case, could just be due to the small-number statistics, a similar relation was also found by Cassano et al. 2008. In their study, while mini-halo clusters share the same region of giant halo clusters in the $\mathrm{P}_{1.4} - \mathrm{L}_\mathrm{X}$ plane, they are clearly separated in the $\mathrm{P}_{1.4} - \mathrm{r}_\mathrm{e}$ plane. Specifically, the synchrotron emissivity of mini-halos is found to be more than 50 times larger than that of giant halos, implying a different and very efficient process for their origins.

The galaxy cluster Abell 1413

In this thesis work, we present a multi-wavelengths analysis of the diffuse emission of the galaxy cluster Abell 1413.

A1413 is a nearby (z=0.1427) galaxy cluster well studied in optical, X-ray and radio bands. Nevertheless, it shows some peculiarities that opens the way to further investigation. From the morphological point of view, it presents a high ellipticity confirmed by both optical (Castagné et al. 2012) and X-ray (G. W. Pratt and Arnaud 2002) studies. As clearly visible in Fig. 3.1a, the elongation of the cluster is approximately aligned in the North-South direction (Castagné et al. 2012). Studying the galaxy number density distribution, Castagné et al. 2012 estimated the value of the cluster ellipticity[1] $\epsilon \sim 0.35$ at large radii, increasing up to $\epsilon \sim 0.8$ at the cluster center $r < 1'$ (see Fig. 3.1b); while fitting the XMM-Newton image, they found values quickly converging toward 0.27, which is fully compatible with the global value of 0.29 derived by G. W. Pratt and Arnaud 2002 over the radial range $[3' - 13']$.

The discrepancy at large radii of the optical and X-ray ellipticity values is not surprising if we consider that the collisional gas relaxes more quickly within the cluster potential than the non-collisional galaxies and reaches more rapidly a spherically symmetric distribution. However, Castagné et al. 2012 stressed that A1413 seems a rather extreme example of this effect.

Moreover, by analysing the velocity distribution of the cluster, they found a velocity offset of $450 \pm 210\, km\, s^{-1}$ (i.e., 2σ significance) between the velocity of the central cD galaxy (Paturel et al. 1989) and the mean cluster velocity. Velocity offsets of BCGs are often found in clusters far from equilibrium, for instance when undergoing major merging events. If confirmed this BCG velocity offset would suggest that A1413 may be in a non-fully relaxed dynamical state.

Despite its highly elliptical shape, early X-ray studies (G. W. Pratt and Arnaud 2002, Vikhlinin et al. 2005, Baldi et al. 2007) classified this cluster as a relaxed system , with no obvious signatures of a merger. The lack of shocks or cold fronts has been also confirmed by Botteon et al. 2018, who explored a combination of different analysis approaches of

---

[1] defined as $1 - b/a$, where a and b are the semi-major and semi-minor axis of the ellipse

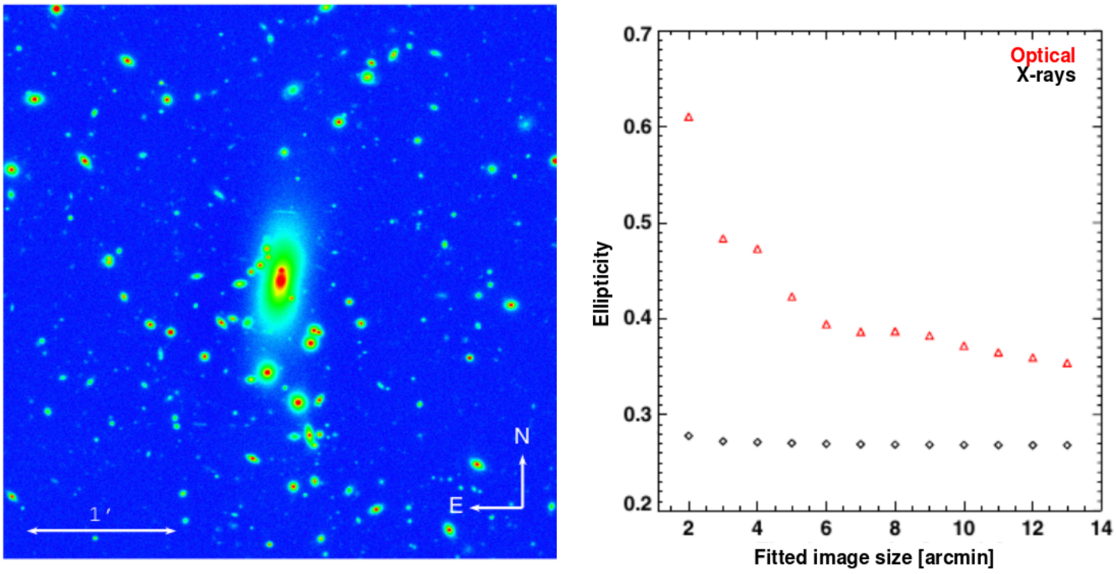

(a)

(b)

Fig. 3.1: *Left panel:* Detailed view of the cD galaxy at the center of A1413. The extended envelope covers more than 100 kpc along the major axis. The image is the result of stacking two images in R and Z bands. Credits: Castagné et al. 2012. *Right panel:* Ellipticity profile of A1413, derived from the galaxy density map (red triangles) and from the XMM-Newton image (black diamond). Credits: Castagné et al. 2012.

X-ray observations to firmly detect and characterize edges in a sample of non-cool-core massive galaxy clusters. The XMM-Newton observation (G. W. Pratt and Arnaud 2002) does not provide strong evidence of a cool core region, in contrast with the temperature profiles obtained with Chandra (Vikhlinin et al. 2005), with a cooling time in the central region of $t_{cool} = 4.2 \pm 0.3\, Gyrs$ (Baldi et al. 2007). The authors suggested that this could be related to the better resolution of Chandra with respect to XMM-Newton.

Recently, it was classified as having a mixed morphology, i.e. with small substructures, not circular X-ray isophotes or relatively flat X-ray distribution, by Lovisari et al. 2017. They studied various morphological parameters able to determine the dynamical state of the galaxy cluster and argued that the best morphological indicators to distinguish between relaxed and disturbed systems, are concentration c and centroid shift w. Using these parameters, according to their classification, A1413 could be classified as a relaxed system (see Tab. 6 in Lovisari et al. 2017).

The first investigation of the radio emission in A1413 was performed by Govoni et al. 2009, who found a candidate mini-halo at 1.4 GHz (see Fig. 3.2a). They noted that the cD galaxy, located in the middle of this putative mini-halo, does not contain a compact radio source, at least at the FIRST[2] sensitivity level (3.2a), and thus speculated about

---

[2] Faint Images of the Radio Sky at Twenty-cm (FIRST) is a project designed to cover over 10,000 square degrees of the North and South Galactic Caps, using the NRAO Very Large Array (VLA), with a typical

the presence of "relic" mini-halos, in which the central cD galaxy is switched-off, while the diffuse mini-halo continues to emit. However, the authors stressed the need for low frequency observations to better understand the emission.

Furthermore, in a statistical study about the occurrence of mini-halos in a mass limited ($M_{500} > 6 \cdot 10^{14} M_{\odot}$) sample, Giacintucci et al. 2017, classified clusters according to the value of the specific central entropy and included A1413 ($K_0 = 64 \pm 8\, keV\, cm^2$) as non-cool-core cluster, the only one of the whole sample hosting a (candidate) mini-halo.

Finally, the radio emission was studied at 144 MHz, in a recent study of non-merging galaxy clusters (Savini et al. 2019), confirming the presence of a mini-halo source at the centre of the cluster (Fig. 3.2b), with size of $\sim\, 210\, kpc$ and a total flux density of $40 \pm 7\, \mathrm{mJy}$.

From these past studies, a controversial and intriguing picture of A1413 emerges, making it a very interesting object.

The aim of this Thesis work is to provide a dedicated and updated multi-wavelength investigation of the galaxy cluster A1413, characterizing its dynamical state, throughout the study of ICM properties, and determining the properties of the diffuse radio emission hosted by the cluster.

Then, for the first time, we aim to correlate radio and X-ray properties to investigate the relation between the thermal and non-thermal emission. These correlations can be useful tools to define observable properties connected to the mechanism which generate the radio emission in galaxy clusters, a still very debated topic.

Throughout this Thesis, the adopted cosmology is the standard ΛCDM with $\mathrm{H_0} = 70\, \mathrm{km\, s^{-1}\, Mpc^{-1}}$ and $\Omega_{\mathrm{M}} = 1 - \Omega_{\Lambda} = 0.3$. Assuming the cluster redshift $z = 0.1427$, the luminosity distance is $\mathrm{D_L} = 675.35\, \mathrm{Mpc}$, leading to a conversion 1 arcsec = 2.50 kpc.

---

rms of 0.15 mJy, and a resolution of 5".

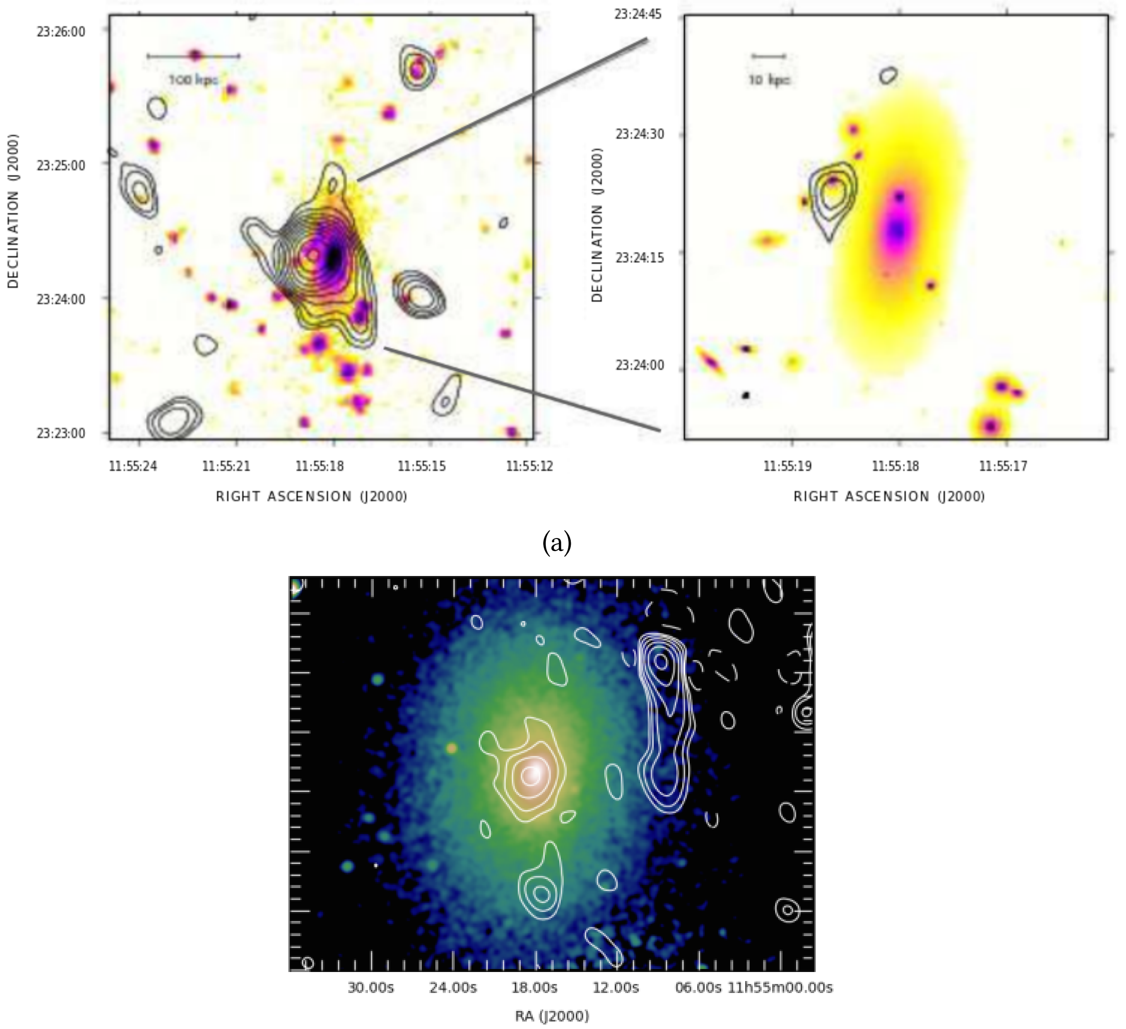

(a)

(b)

Fig. 3.2: *Top left panel:* radio contours of A1413 at 1.4 GHz with a beam of $15'' \times 15''$, overlaid to the optical POSS2 image. The first contour level is drawn at 0.1 mJy/beam and the rest are spaced by a factor $\sqrt{2}$. The sensitivity (1σ) is 0.035 mJy/beam. *Top right panel:* zoom of total intensity radio contours in the center of A1413 at 1.4 GHz with a beam 5.4×5.4 taken from the first survey. The first contour level is drawn at 0.5 mJy/beam and the rest are spaced with a factor $\sqrt{2}$. The sensitivity of the first survey is 0.15 mJy/beam. The contours of the radio image are overlaid on the optical image taken from HTS (F606W) archive. Credit: Govoni et al. 2009. *Bottom panel:* Chandra X-ray image of A1413 smoothed on a scale of $5''$ with 144 MHz LOFAR contours overlaid from a radio image with beam $20'' \times 20''$. The contour levels start at 3σ, where $\sigma = 450\,\mu\mathrm{Jy/beeam}$, and are spaced by a factor of two. Credit: Savini et al. 2019.

X-ray Analysis

In this chapter we describe the main steps of the X-ray analysis. Since A1413 was observed with XMM-Newton, here we present a short description of its characteristic and of the instruments on board of the satellite (Sec. 4.1). In Sec. 4.2 we illustrate the process of data reduction and analysis, and finally we interpret and shown the the main results in Sec. 4.3.

The goal of the X-ray analysis is to investigate the dynamical state of the cluster by performing a spectral analysis and morphological studies, to derive the ICM physical properties.

XMM-Newton, with its high throughput, large collective area and large field of view, is the satellite best-matched for the detection and study of the ICM diffuse emission.

4.1 XMM-Newton

Since Earth's atmosphere blocks out all X-rays, only a telescope in space can detect and study celestial X-ray sources. Thus, X-ray telescopes, such as XMM-Newton are satellites orbiting around the Earth.

XMM-Newton is a ESA mission launched on December 10th 1999. It carries 3 high throughput X-ray telescopes with an unprecedented effective area (see §4.1.2), and an optical monitor, the first flown on a X-ray observatory. The large collecting area and ability to make long uninterrupted exposures are the strenghts of this satellite, and provide highly sensitive observations.

4.1.1 The Telescopes of XMM-Newton

Since X-rays are high energy photons, it is difficult to reflect or refract them. Thus, the optics needed to focus them must take advantage of the phenomena of grazing-incidence. It means that in order to avoid the transmission of the incident photons, they had to be almost parallel to the X-ray optics (Fig. 4.1a top left box), thus, the mirror system had to utilize a very shallow grazing angle $\theta < \theta_c \propto \sqrt{\rho}/E$, which depends on the optics reflecting material ρ and the energy of incident photon E. Usually, high

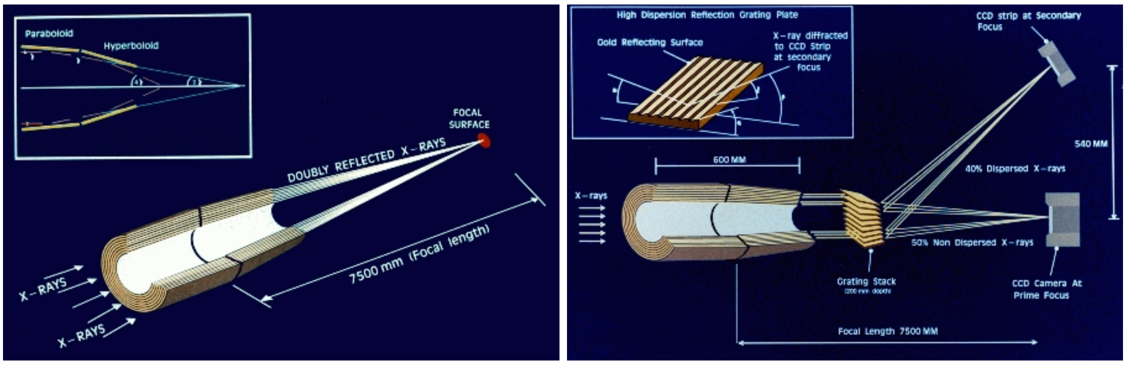

(a) (b)

Fig. 4.1: Light path in the XMM-Newton telescope with only an EPIC camera in its primary focus (left), and in the two telescopes in which a RGA is mounted into the optical path (right).

density materials (e.g., gold, platinum or iridium, with density around 20 $\mathrm{g/cm^3}$) are used for reflecting surface because they allow a larger critical angle θ_c. Since θ is inversely proportional to X-rays energy, total reflection works only in the soft band. Thus, current X-ray telescopes generally work in a energy range between $\sim$0.1 and $\sim$10 keV, i.e. with very small grazing angles, between 0.5 and 1 degree.

XMM-Newton is equipped with 3 telescopes: each Mirror Module is a grazing-incidence Wolter I telescope[1] consisting of 58 gold-coated nested shells in a coaxial and cofocal configuration. The design of the optics was driven by the requirement of obtaining the highest possible effective area over a wide range of energies, with particular emphasis in the region around 7 keV, where the K lines of astrophysically significant iron appear.

One telescope has a light path as shown in Fig. 4.1a; the two others carry a Reflection Grating Array (RGA) in their light paths, diffracting about 40% of the incoming radiation onto their secondary focus Fig. 4.1b.

There are three scientific instruments aboard XMM-Newton, illustrated in Fig. 4.2:

- **European Photon Imaging Camera (EPIC)**
  At the prime focus of each of the spacecraft's three telescopes, behind a six-position filter wheel[2], is a European Photon Imaging Camera (EPIC). With silicon chips that can register extremely weak X-ray radiation, these advanced Charge-Coupled Device cameras (CCD) are capable of detecting rapid variations in intensity, down to a thousandth of a second and less.

---

[1] Wolter I configuration consists of a paraboloid and an associated hyperboloid: the combination of these permits to reduce the focal lenght (i.e., the dimension of the telescope itself), which for XMM-Newton is equal to 7.5 meters, with mirrors diameter up to 70 cm. This configuration also allows to nest many shells to increase the collecting area: the thinner the mirror shells are and the narrower the shells are spaced, the larger is the collecting area.

[2] The EPIC CCD cameras on board XMM-Newton are equipped with light and UV blocking filters. There are 6 different filter setups (Closed, Thin1, Thin2, Medium, Thick, Open). Closed position is used to protect the CCDs from soft protons in orbit, while the open position can be used for observations where the light flux is very low, and no filter is needed.

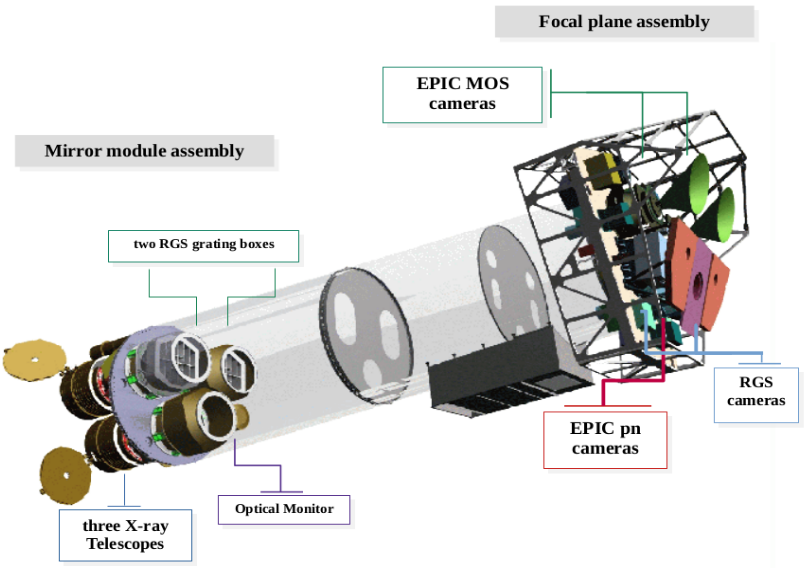

Fig. 4.2: Sketch of the XMM-Newton payload. The mirror modules, two of which are equipped with Reflection Grating Arrays, are visible at the lower left. At the right end of the assembly, the focal X-ray instruments are shown: The EPIC MOS cameras with their radiators (black/green “horns”), the radiator of the EPIC pn camera (violet) and those of the (light blue) RGS detectors (in pink). Credit: *XMM-Newton Users Handbook* n.d.

- **Reflection Grating Spectrometer (RGS)**
  For a complementary analysis of the spectrum, two of the three telescopes have a grating structure on their mirror module that reflects about 40% of the incoming rays to a secondary focus, with its own CCD camera.

- **Optical Monitor (OM)**
  The third instrument aboard XMM-Newton is a conventional but very sensitive optical/UV telescope, the Optical Monitor (OM). It can observe simultaneously the same regions as the X-ray telescopes, but at ultraviolet and visible wavelengths. This gives astronomers complementary data about the X-ray sources.

In the next lines the main characteristics of the instrument of interest are shown. For this analysis, a good knowledge of EPIC camera is needed, thus a detailed description of it follows.

4.1.2 Instrument characteristics

The main properties that characterize the performance of an X-ray telescope are the Point Spread Function (PSF) and Effective Area.

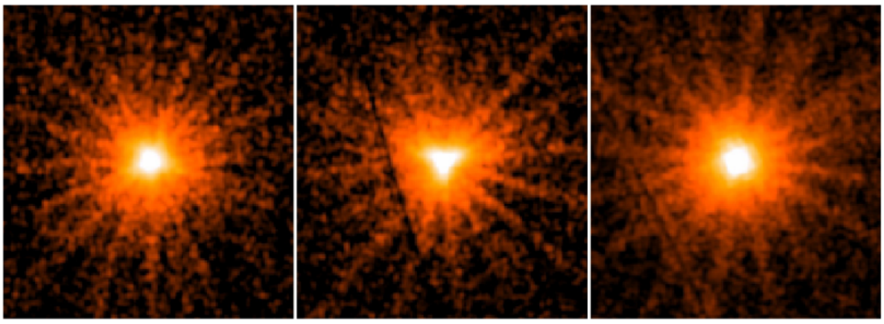

Fig. 4.3: On-axis PSFs of the 3 epic detectors (MOS1 *right*, MOS2 *center*, pn *right*) for the same non-piled-up source from the same observation (2XMM J130022.1282402, ObsID 0204040101, revolution 823). The images are 0.2-10 keV and very lightly smoothed, to accentuate the features. Credit: Read et al. 2011.

The PSF measures the ability of an instrument of focusing photons. Therefore, it is a critical parameter in determining the quality of an X-ray mirror module. Unlike the optical band, where the PSF is affected primarily by the seeing, in the X-ray band it reflects the mirrors properties (e.g., how smooth is the surface of the mirrors) and array assembly (e.g., how well aligned are the nested mirrors). Not only it depends on the position of the incoming photon $\mathrm{PSF} = \mathrm{PSF(x, y)}$, but also each of the three Wolter type I X-ray telescopes on board XMM-Newton has its own PSF. As an example, Fig. 4.3 shows the PSFs of the MOS1, MOS2 and pn X-ray telescopes, registered on the same on-axis non-piled-up source.

The *effective area*, A_e, reflects the ability of the mirrors to collect radiation at different photon energies and it is generally given by

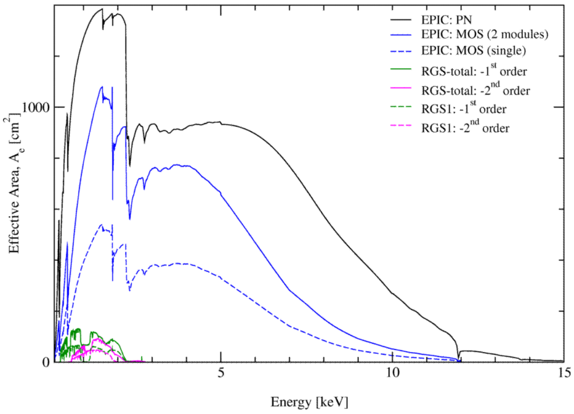

Fig. 4.4: The net effective area of all XMM-Newton X-ray telescopes, EPIC and RGS (linear scale).

$$A_e(E,x,y) = A_{geom} \cdot R(E) \cdot V(E,x,y) \cdot QE(E,x,y) \tag{4.1}$$

where geometric area A_{geom} , reflectivity $R(E)$, and vignetting $V(E,x,y)$, depend on the telescope optics, while the quantum efficiency $QE(E,x,y)$ depends on the detector properties. The variation of A_e as a function of the incoming photons energy, for each instrument on board of XMM-Newton, is shown in Fig. 4.4. The XMM-Newton mirrors are most efficient in the energy range from 0.1 to 10 keV, with a maximum at about 1.5 keV and a pronounced edge near 2 keV (the Au edge). Note that the effective area of a single MOS module (blue dashed line) is about a half of pn-camera, because only part of the incoming radiation falls onto MOS detectors, which are partially obscured by the RGAs.

4.1.3 EPIC onboard XMM-Newton

The XMM-Newton spacecraft is carrying a set of three X-ray CCD cameras, comprising the European Photon Imaging Camera (EPIC). Two of the cameras are Metal Oxide Semiconductor CCD arrays (MOS cameras, Fig. 4.5a). They are installed behind the X-ray telescopes that are equipped with the gratings of the Reflection Grating Spectrometers (RGS). The gratings divert about half of the telescope incident flux towards the RGS detectors such that about 44% of the original incoming flux reaches the MOS cameras (Fig. 4.1b). The third X-ray telescope has an unobstructed beam; the EPIC instrument at the focus of this telescope uses pn CCDs (pn camera, Fig. 4.5b).

The EPIC cameras offer the possibility to perform extremely sensitive imaging observations over the telescope's field of view (FOV) of 30 arcmin and in the energy range from 0.15 to 15 keV with moderate spectral ($E/\Delta E \sim 20-50$) and angular resolution (PSF, 6 arcsec FWHM).

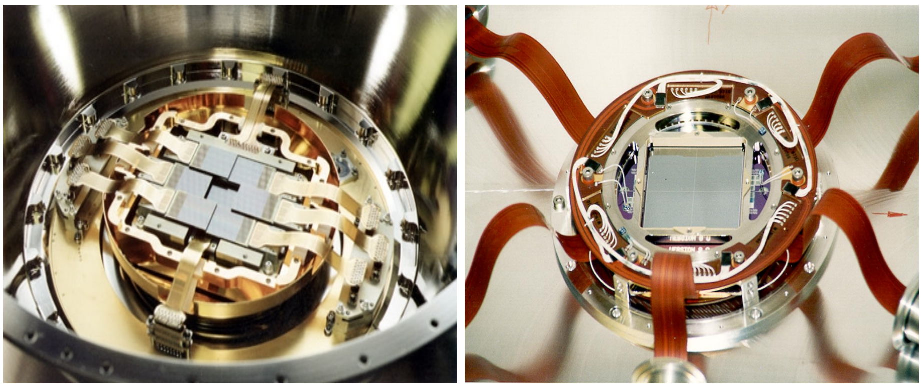

(a) (b)

Fig. 4.5: The CCDs of one of the MOS cameras in the cryostat *(left)*; The CCDs of the pn camera: twelve chips mounted and the connections to the integrated preamplifiers *(right)*. Credit [*XMM-ESA-WebSite* n.d.]

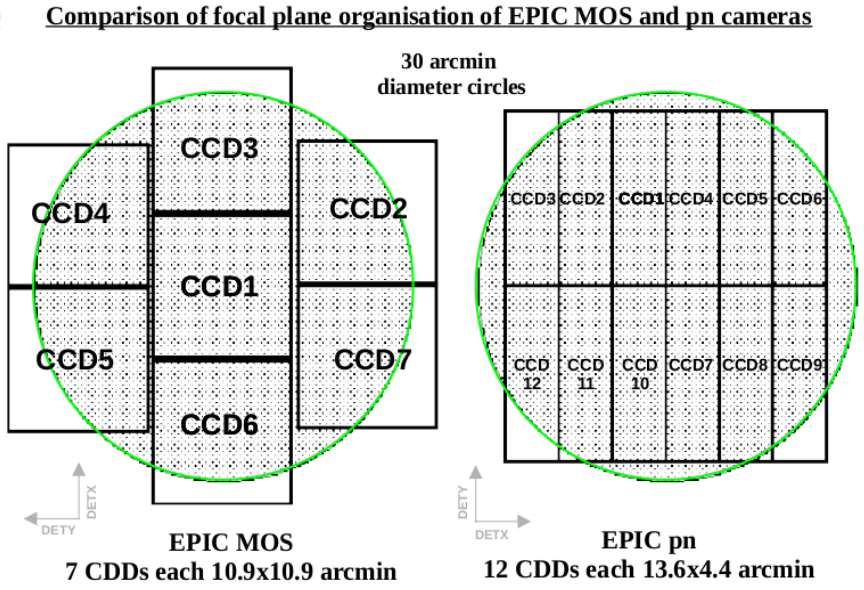

Fig. 4.6: A rough sketch of the field of view of the two types of EPIC camera; MOS *(left)* and pn *(right)*. The shaded circle depicts a 30 arcmin diameter area. Thus far, two CCDs of the MOS1 camera have been lost due to micrometeoroid impacts into the focal plane: CCD3 (11 December 2012) and CCD6 (9 March 2005).

The MOS chip arrays consist of 7 individual identical, front-illuminated chips; while the pn camera is a single Silicon wafer with 12 CCD chips integrated. The numbering scheme for the EPIC MOS and pn chip arrays and the directions of the detector coordinates are displayed in Fig 4.6 *(left)* and Fig. 4.6 *(right)*, respectively. The MOS cameras are orthogonally oriented. Hence, the RGS dispersion direction is aligned with the DETY direction[3] in the MOS1 camera, while it is aligned along the DETX direction in the MOS2 camera.

EPIC background

EPIC background is a mixture of different component:

- Electronic noise: such as bright pixels, bright columns, readout noise etc., which becomes important at low energies (< 300 eV);
- Cosmic X-ray background, compose by different unresolved AGN sources (hard X-ray background photons) and from the Local Bubble, Galactic Disk, Galactic Halo, the Solar Wind Charge Exchange (soft X-ray background photons);
- Particles background, which consist of
  - External ’flaring’ background: produced by the so-called soft protons (SP), ~ 100 keV solar protons, that are accelerated by magnetospheric reconnec-

---

[3] The DETX and DETY coordinate system is fixed with respect to the EPIC instrument

tion events and thus are quite variable, unpredictable background sources. These soft protons occur in flares up to 1000% of the quiescent level in an observation: their signal is indistinguishable from X-ray photons and therefore, it produces an enhanced background;

- Internal 'quiescent' (cosmic-ray induced) background, produced by direct interaction of High Energy particles (cosmic rays, with energies larger than some 100 MeV) with the detectors, or indirectly when hitting satellite components, causing associated instrumental fluorescence.

4.2 XMM data reduction and analysis

The more recent observations of A1413 date from the years between 2007 and 2008: all four observations are longer than 60 ks each. The one chosen for this analysis is the longest and less flared one, OBS ID 0502690201 (as shown in Tab. 4.1). Data consists in 82.5 ks archival observation time during XMM-Newton revolution 1466 (2007 December 11), obtained with the THIN1 filters and are processed with XMMSAS v19 and the ESAS software package (Snowden et al. 2008), through a dedicated pipeline that follows the procedure described in Lovisari et al. 2019 and which is briefly described in this section. The pipeline processes the X-ray data from the raw data, the Observation Data File (ODF), to the 2D maps, passing through data calibration and filtering, imaging, and spectral fitting.

In order to get the proper event fits files from the raw data, the tasks `cifbuild` and `odfingest` need to be run. The former provides an up-to-date list of the relevant calibration files (the Calibration Index File - CIF[4]), while the latter produces extended ODF summary file needed for subsequent data processing.

Then, we run the `emchain` and `epchain` tasks to convert the raw data into calibrated photon event files for the MOS and pn camera, respectively. Also, out-of-time events (OoT) file for the pn data are created. Out-of-time events occur because the read-out period for the CCDs can be up to $\sim 6.3\%$ of the frame time[5]. These events, occurring when a photon hits the CCD during the read-out process, cannot be distinguished from others events and are included in the event files; however they will not be associated with the correct sky location. For observations with bright sources they can provide a serious contamination of both images (as bright stripes along the CCD read-out direction) and spectra (broadening the spectral features). The OoT event files allow to remove

---

[4] XMM-Newton data reduction and analysis requires extensive calibration data (Current Calibration Files - CCF) which need to be dowloaded from the SOC XMM-Newton Calibration page. Relevant files are accessed from the set of CCF data using a CCF Index File (CIF).

[5] Fraction of OoT events scales with mode-dependent ratio of integration and readout time: highest for pn full frame (6.3%) and extended full frame (2.3%)mode.

statistically their contamination from images and spectra.

The event files need to be filtered and manipulated to get rid of electronic noise and events which are not X-ray photons, SP flares, and point sources in the field.

Standard filtering procedure is achieved first, by discriminating the event based on their pattern, i.e. distribution of pixels over which a charge cloud spreads. A good X-ray pattern must be compact, with the highest charge at the center. The pattern assignments are: single pixel events PATTERN=0, double pixel events PATTERN in [1:4], triple and quadruple events PATTERN in [5:12]. Good pattern (created by X-ray photos) are 0-12 for MOS and 0-4 for pn; other patterns are probably connected with Comic Rays and are eliminated. Secondly, events with energies higher than 15 keV and lower than 0.3 keV are removed, due to the low effective area (as shown in Fig. 4.4) at high energy and soft electronic contamination, respectively. Finally hot and bad pixels are excluded via the FLAG value, that provides a bit encoding of various event condition concerning pixel with abnormal behaviour or out-of-fied-of-view (OoFoV). During this filtering also dead time and bad frames are removed.

Moreover, it is known that there are some MOS CCDs in anomalous states, which detect a very high soft emission. The cause of these anomaly is still unknown, thus, a good choice when possible, is to definitely not use them for all the data analysis process. The anomalous CCD are inspected via `mos-filter` task: in this case, CCD 7 for MOS2 is excluded from the analysis, while CCD 6 of MOS1 was demaged by a meteorite and thus, not available.

Successively, the light curve has been filtered to determine the good time intervals (GTIs), time intervals not affected by the solar flares. These flares vary strongly with time and currently we do not have a model to account for their contribution. Thus, the only option to get rid of this contamination is by removing completely parts of the observation altered by flares. Determining the bad interval is quite straightforward: since extended X-ray gas is assumed to have constant flux, the times where the event rate rises are related to flares, and can be eliminated. The data are cleaned using a two-stage filtering process (extensively described in Lovisari et al. 2011):

- Since particle background dominates at high energy, light curve with 100s bins are first inspected in [10-12] keV band for MOS and [12-14] keV for pn. From a simple visual inspection, t is quite evident the time bins where SP flares affect the observation (Fig. 4.7a).
  Then, the histogram of the light curve is fitted with a Poissonian distribution (Fig. 4.7b):
  $$y(x,\lambda) = \frac{\lambda^x \, e^{-\lambda}}{x!} \tag{4.2}$$

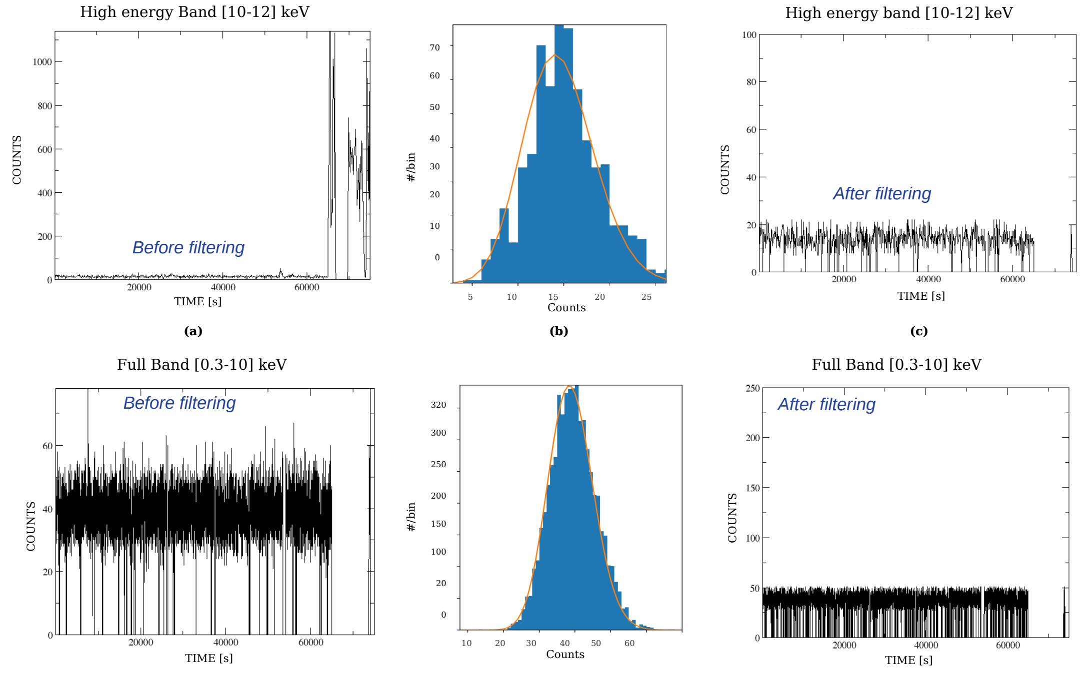

(a) (b) (c)

(d) (e) (f)

Fig. 4.7: Light Curve filtering procedure for MOS1. *First row:* screen using high energy band [10-12] keV. Light curve with bins of 100s and best fit parameter $\lambda = 14.53\, cts/100s$. *Second row:* screen based on full energy band [0.3-10] keV. Light curve with bins of 10s and best fit parameter $\lambda = 38.87\, cts/10s$.

where x = cts/bin, to find the mean of the distribution λ, that allows to set a threshold value $\pm 2\sigma$, where $\sigma = \sqrt{\lambda}$ is the error on the mean, using Poisson statistic. Then, exclude all the intervals of exposure time having higher count rate, i.e. count rate that deviated by more than 2σ from the mean (see G. W. Pratt and Arnaud 2002, Appendix A for a precise description). The result of the first filtering is shown in Fig. 4.7c. By comparing 4.7a and 4.7c, it is evident that most of the flare contaminated intervals have been removed.

- After this high energy band screening, the second-stage filtering is done with the full [0.3-10] keV band, as a safety check for possible flares with soft spectra (Nevalainen et al. 2005). In this case, considering the full band, 10s bins is sufficient to have a good statistic. So, the binning of the light curve and modeling of the histogram is repeated, and the final two-step filtered light curve is obtained (Fig. 4.7d,e,f)

This procedure has been carried out independently for each of the three detectors and exposure time before and after GTI filtering are shown in Tab. 4.1.

Obs ID - 0502690201			**Obs ID - 0502690101**		
camera	observed exp time [ks]	cleaned exp time [ks]	camera	observed exp time [ks]	cleaned exp time [ks]
MOS1	82.5	56.9	MOS1	66.7	33.6
MOS2	82.5	57.5	MOS	66.7	33.6
pn	82.5	40.5	pn	66.7	3.0
Obs ID - 0551280101			**Obs ID - 0551280201**		
camera	observed exp time [ks]	cleaned exp time [ks]	camera	observed exp time [ks]	cleaned exp time [ks]
MOS1	76.7	48.9	MOS1	76.2	46.8
MOS2	76.7	49.6	MOS2	76.2	47.5
pn	76.7	36.6	pn	76.2	34.0

Tab. 4.1: Exposure time of each detector before and after the flare-cleaning, for each archive observation. The observation 0502690201, used in this work, is clearly the less flared. Exposure time pre and post flare filtering for the other observations were already available from Lovisari et al. 2017 (private communication).

Filtering the light curve does not ensure that all SP components are eliminated. There could be continuous and constant flares (i.e. flares that last for long time intervals), without evident spikes, that still remain. We can first estimate the amount of residual SP flare contamination by using the suited code of deLuca&Molendi 2004. It compares area-corrected count rates in the *in-FOV*, affected by residual SP (owing to the focusing of the low energy particles by the telescope optics), and *out-of-FOV* regions of the detector, where no SP residual should be present, in the range 8−12 keV and excluding the central CCD region (r $> 10\,\mathrm{arcmin}$) in order to minimize the presence of genuine cosmic X-rays in the count rate in the *in-FOV*. The higher the in-FOV to out-of-FOV ratio, the more the file is contaminated by SP. Results are shown in Tab. 4.2.

Even if the SP contamination is low[6], it is important to include SP contamination as an extra model component, when dealing with spectral fitting (§4.3.2).

We are interested in the galaxy cluster emission, thus, all point sources in the field are removed using the REGION file, available together with all PPS data[7]. Since the REGION file is created by standard pipeline of XMM-Newton, before cleaning data from point

---

[6] Usual bands are:
$\mathrm{F}_{\mathrm{IN}}/\mathrm{F}_{\mathrm{OUT}} < 1.15$: File is not contaminated by SPs.
$\mathrm{F}_{\mathrm{IN}}/\mathrm{F}_{\mathrm{OUT}}$ 1.15-1.3: File is *slightly* contaminated by SPs.
$\mathrm{F}_{\mathrm{IN}}/\mathrm{F}_{\mathrm{OUT}}$ 1.3-1.5: File is *very contaminated* by SPs.
$\mathrm{F}_{\mathrm{IN}}/\mathrm{F}_{\mathrm{OUT}} > 1.5$: File is *extremely* contaminated by SPs.

[7] XMM ODF data are released together with the pipeline processed data products (PPS), data already processed, obtained with old calibration file and standard setup, an thus used just for a first look at the data. However, there are some useful products, including the REGION file.

	Obs ID - 050269020		
Instrument	counts IN	counts OUT	F_{IN}/F_{OUT}
MOS1	13618	5377	1.120±0.025
MOS2	16296	6956	1.120±0.023
PN	32286	3821	1.120±0.024

Tab. 4.2: Results for the SP residual contamination. Count rates in the *in-FOV* (*Col.2*); Count rates in the *out-of-FOV* (*Col.3*) regions of the detector; F_{IN}/F_{OUT} ratio calculation (*Col.4*).

sources, the file is inspected to discriminate between real point sources and extended cluster sub-structures, detected in particular in the BCG region. Even if identified as point-source, we did not remove the BCG region because the cluster emission is so bright that the contribute of the AGN is negligible and can be modeled as a power law during the spectral fitting.

4.3 Results

4.3.1 Images

To derive EPIC background subtracted, exposure corrected images, data (filtered and point-source subtracted) from the three instruments are combined properly. To take the background into account, using the available Blank Sky Fields Field[8] (BSF) event files (see Carter&Read 2007) is not very accurate for XMM-Newton. In fact, since XMM-Newton background is variable (with temporal, spectral, and spatial variations), it can happen that the contribution to the background in the BSF is different from the actual observation. A better way to proceed, as previously mentioned, is to model the background with all its components.

To determine the mean count rate of each background component, the following data are fitted and used:

- Archival ROSAT[9] file for astrophysical sky background
  Since in ROSAT observations, particle background is negligile, these can be considered as pure sky data. So, ROSAT All-Sky Survey (RASS) diffuse background maps in a region beyond the virial radius (between 1 and 2 degrees) are downloaded[10] and used to model this component of background emission, with an absorbed ~ 0.2 keV thermal component representing the Galactic halo emission, an unabsorbed ~ 0.1 keV representing the Local Hot Bubble (LHB) and an absorbed power-law model with its slope set to 1.41 representing the unresolved point sources (deLuca&Molendi 2004).

- Filter Wheel Closed (FWC) observation for instrumental particle background
  FWC exposures are taken with closed filters that avoid that X-ray photons hit the detector and thus, are dominated by the instrumental background and can be modeled to subtract the internal instrumental background. The model used for FWC observation consist in a power-law with additional fluorescence lines (e.g. Fe, Al, Si, Au). Unexposed corners of the CCD chips are used to measure the particle background level in each observation. Since FWC observation are taken in different time period from our observation and have a different exposure, they need to be normalized, comparing them with the OoFoV data.

---

[8] In general, Blank sky background event files, constructed for each of the EPIC instruments in each filter/mode combination, can be used to model/subtract the background of an observation. That is for example, the case of extended sources, that occupy all the FoV, when "local" background can't be considered.

[9] ROSAT, the ROentgen SATellite, was an X-ray observatory developed through a cooperative program between the Germany, the United States, and the United Kingdom. The satellite launched by the United States on June 1, 1990 and turned off on February 12, 1999.

[10] tool at the HEASARC webpage `https://heasarc.gsfc.nasa.gov/cgi-bin/Tools/xraybg/xraybg.pl`

- An outer annular region for the SP residual
  the contribution of SP is calculated in an external region between 9 and 12 arcmin, where the cluster contribution is minimal. This is done by adding a power law component folded only with the RMF, with normalization free to vary, to a complex model that comprises all the other background component and a residual cluster emission.

Background subtracted and exposure corrected image of the cluster emission in two bands ([0.7-2] keV and [0.3-7] keV) are shown in Fig. 4.8. Regions where point sources were subtracted have been filled using `dmfilth`, a CIAO task that replaces pixel values in a source region with values interpolated from surrounding background regions, and the image is smoothed with a 3" gaussian.

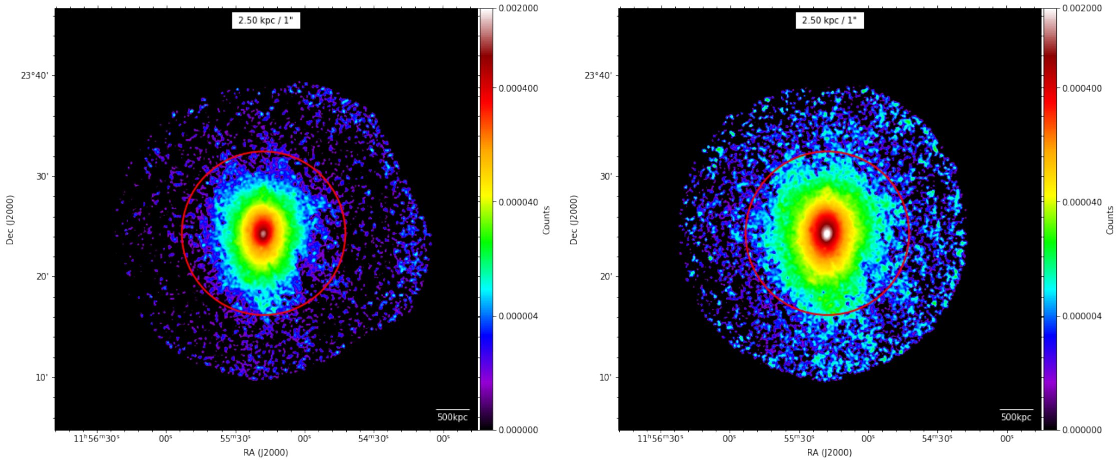

Fig. 4.8: Background-subtracted and exposure-corrected images of A1413 in the 0.7-2 keV (*left panel*) and 0.3-7 keV (*right panel)* bands, respectively. The *red circle* marks the position of $\mathrm{R}_{500} \sim 1224\,\mathrm{kpc}$, i.e., the radius within which the mass density is 500 times of the critical density $\rho_c(z) = E^2(z)3H_0^2(8G)^{-1}$, at the cluster redshift. Both images are smoothed with a 3" gaussian.

4.3.2 Spectral Analysis

All the spectral fits are performed with the XSPEC (Arnauld 1996) package v12.11.1, in the [0.5-12] keV and [0.5-14] keV energy range for MOS and pn, respectively, by modeling the cluster emission with an `apec` single-temperature thermal plasma model with an absorption fixed at the total (neutral and molecular; see Willingale et al. 2013) $\mathrm{N_H} \sim 1.97\,10^{20}\,\mathrm{cm}^{-2}$ value estimated using the SWIFT online tool[11]. For the apec model (Smith et al. 2001) the parameters are: plasma temperature [keV], metal abundances (the elements included are C, N, O, Ne, Mg, Al, Si, S, Ar, Ca, Fe, Ni), redshift (that is kept fixed

---

[11] `https://www.swift.ac.uk/analysis/nhtot/index.php`

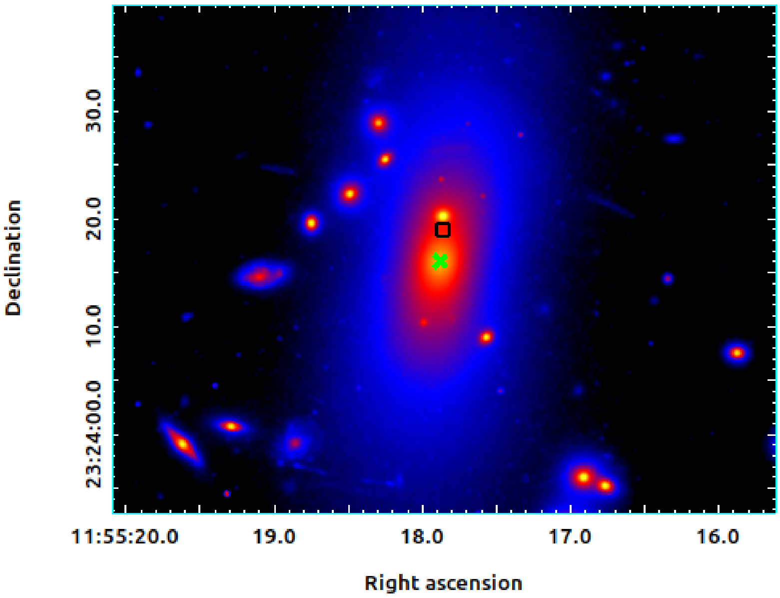

Fig. 4.9: HTS (F606W filter) image of the central BCG. The black box marks the position of the X-ray peak, while green cross corresponds to the BCG.

at z=0.1427), and the normalization $\frac{10^{-14}}{4\pi[D_A(1+z)]}\int n_e n_H dV$, with D_A the angular distance of the source, n_e,n_H the electron and proton densities in units of cm^{-3}

All the regions used for the spectral profiles were centred on the peak of the X-ray emission of coordinates R.A.(J2000) $11^h55^m17^s.85$, DEC. (J2000) $+23°24^m18^s.85$. Note that we found a small offset of about 7.2 kpc between the X-ray peak with the optical BCG (see Fig. 4.9). The coordinates of the central galaxy were available R.A. (J2000) $11^h55^m17^s.87$, DEC. (J2000) $+23°24^m16^s.02$. (Rawle et al. 2012) and correspond to the brightest pixel of the optical image, retrieved from HTS (F606W filter) archive. Recent statistical studies by Rossetti et al. 2015, have shown that an off-set less than $0.02\,R_{500}$ (as in this case $7.2\,kpc \ll 0.05\,R_{500}$) is still characteristic of relaxed systems.

The size of the annuli have been determined by requiring a minimum width of $30''$ and a fixed S/N=50. The first requirement ensures that most of the flux (i.e. $>$ 80%, Zhang et al. 2009) comes from the selected region (due to the XMM–Newton PSF, some photons scatter from one annulus to another); the second that the 1σ uncertainty in the spectrally resolved temperature (and consequently in the fitted temperature profiles) is <10% (see Lovisari et al. 2019 for more details of how uncertainties vary as function of S/N and cluster temperature). The redistribution matrix and auxiliary response[12] files (RMF and ARF) are created with the SAS tasks `rmfgen` and `arfgen` for each camera and each region that are analyzed. The background is modeled together with the cluster emission by performing a join fit with the above explained RASS spectrum and FWC observations components, and cluster emission extracted from each region. Temperatures and metallicities obtained for each annulus are listed in Tab. 4.3.

---

[12] ARF includes information on the effective area, filter transmission and any additional energy-dependent efficiencies, i.e. the efficiency of the instrument in revealing photons; while RMF associates to each instrument channel the appropriate photon energy

The projected temperature profile is shown in Fig. 4.10, left. The contribution of SP can be evaluated by doing the fit with a constant, variable or no SP residual component. As previously mentioned, an extra power law, folded only with the RMF, is added to the background modelling to account for a residual SP contamination which is affecting the observation even after filtering flare events. The effect is clear: at outer radii, where the contribution of the cluster emission decreases, the SP contaminate the emission and causes higher spectral temperature. The option that allows the SP component to spatially vary can account, in first approximation, for the proton vignetting. In fact, protons are funneled toward the detectors by the X-ray mirrors, and thus the power-law should be folded also through the ARF. However, the proton vignetting is different from the photon vignetting (Marelli et al. 2017) and there is no proton vignetting model available. Letting the SP component spatially vary the normalization can provide for this vignetting effect. However, the spectral temperature profile obtained with SP kept fixed or free to vary are consistent within the error, meaning that in this case SP remain quite stable.

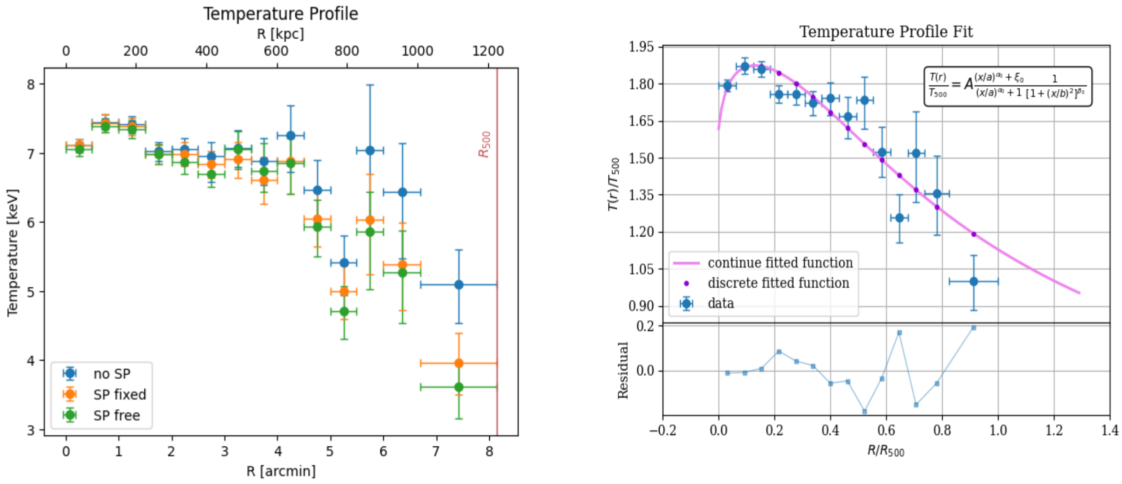

Fig. 4.10: Projected temperature profile: Projected temperature profile, given 3 different contribution of SP(*left*); Projected temperature profile with SP fixed, fitted with an analytical function by Vikhlinin et al. 2006 (*right*).

The metals abundance of the apec model is a mean abundance that gather the possible emission from different elements (C, N, O, Ne, Mg, Al, Si, S, Ar, Ca, Fe, Ni) and where Fe generally dominates. The results, again shown for different evaluation of the SP component, are displayed in Fig. 4.11. The two graphs show the same profile compared with average metallicity profiles for relaxed (left) and disturbed (right) galaxy groups and clusters studied by Lovisari et al. 2019, as a reference.

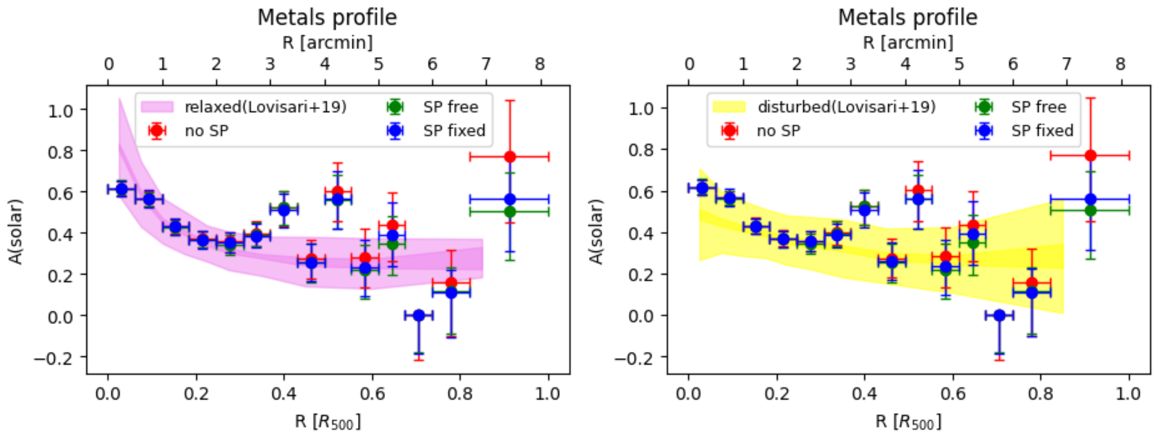

Fig. 4.11: Metals aboundance profile obtained from spectral fitting, compared with different averaged value of relaxed sistems sample *(left)* and disturbed ones *(right)* taken from Lovisari et al. 2019.

It is well known that for relaxed cool-core galaxy cluster the temperature profile shows a clear drop in temperature in the central region (G. Pratt et al. 2008), while the metals profile presents a central peak (Lovisari et al. 2019). In our case the temperature does not show the drop in the central region clearly: just the innermost bin presents a cooler temperature. On the other hand, at the outer radii the temperature profile decreases as expected for typical relaxed cluster. This is consistent with the analysis of G. W. Pratt and Arnaud 2002, but could be due to the low resolution of XMM (as pointed out in Vikhlinin et al. 2005). With this perspective the profile has been fitted with an empirical function derived by Vikhlinin et al. 2006 for the temperature profiles of a low-redshift cool-core cluster sample:

$$\frac{T(r)}{T_{500}} = A\frac{(x/a)^{\alpha_0}+\xi_0}{(x/a)^{\alpha_0}+1}\frac{1}{[1+(x/b)^2]^{\beta_0}} \tag{4.3}$$

with $x = r/r_{500}$ and best fit parameter $\alpha_0 = 0.93$; $\beta_0 = 0.43$; $A = 2.03$; $\xi_0 = 0.81$.

Also, the metal profile neither show explicit peak nor seems to follow a specific (relaxed or disturbed) trend when compared with general cluster sample behaviour.

4.3.3 Surface Brightness profile

The radial surface brightness (SB) profiles are computed in the [0.7–2] keV energy band, which provides an optimal ratio of the source and background flux in XMM-Newton data. The annuli for the SB profile are again centered on the X-ray peak and have been determined by requiring a fixed S/N=10 and minimum width of 2″.

First, the profile was fitted in the outer radii ($> 1.3'$) with a single β-model (Fusco-Fermiano 1976, see eq. 1.9) and extrapolated in the inner regions (Fig. 4.12). The best fit values are $\Sigma_0 = 0.42 \pm 0.05$, $r_c = 224.24 \pm 0.15$, $\beta = 0.76 \pm 0.01$. It is evident a

r_{min}-r_{max} [arcmin]	kT [keV]	Z $Z_\odot$	n_e [cm^{-3}]	t_{cool} [Gyr]
$0-0.5$	$7.11^{+0.09}_{-0.09}$	$0.61^{+0.04}_{-0.04}$	$(1.19 \pm 0.24)10^{-2}$	6.44 ± 1.29
$0.5-1$	$7.43^{+0.12}_{-0.13}$	$0.56^{+0.04}_{-0.04}$	$(0.65 \pm 0.22)10^{-2}$	12.10 ± 4.02
$1-1.5$	$7.38^{+0.12}_{-0.12}$	$0.43^{+0.04}_{-0.04}$	$(0.37 \pm 0.08)10^{-2}$	20.99 ± 4.71
$1.5-2$	$6.97^{+0.14}_{-0.13}$	$0.37^{+0.04}_{-0.04}$	$(0.25 \pm 0.04)10^{-2}$	30.48 ± 5.68
$2-2.5$	$6.98^{+0.17}_{-0.17}$	$0.35^{+0.05}_{-0.05}$	$(0.17 \pm 0.03)10^{-2}$	43.60 ± 7.53
$2.5-3$	$6.84^{+0.20}_{-0.18}$	$0.38^{+0.06}_{-0.06}$	$(0.12 \pm 0.02)10^{-2}$	60.15 ± 9.62
$3-3.5$	$6.90^{+0.27}_{-0.25}$	$0.51^{+0.08}_{-0.08}$	$(0.09 \pm 0.01)10^{-2}$	82.03 ± 12.09
$3.5-4$	$6.61^{+0.34}_{-0.32}$	$0.26^{+0.09}_{-0.09}$	$(0.70 \pm 0.09)10^{-3}$	106.17 ± 14.47
$4-4.5$	$6.84^{+0.47}_{-0.37}$	$0.56^{+0.14}_{-0.14}$	$(0.45 \pm 0.03)10^{-3}$	140.01 ± 17.84
$4.5-6$	$6.05^{+0.40}_{-0.38}$	$0.23^{+0.14}_{-0.13}$	$(0.42 \pm 0.04)10^{-3}$	166.06 ± 19.60
$6-6.5$	$4.99^{+0.40}_{-0.37}$	$0.39^{+0.15}_{-0.16}$	$(0.34 \pm 0.03)10^{-3}$	187.60 ± 21.01
$6.5-7$	$6.03^{+0.79}_{-0.65}$	$0.00^{+0.00}_{-0.18}$	$(0.28 \pm 0.02)10^{-3}$	251.99 ± 29.45
$7-7.5$	$5.38^{+0.66}_{-0.60}$	$0.11^{+0.21}_{-0.11}$	$(0.22 \pm 0.03)10^{-3}$	297.48 ± 41.37
$7.5-8$	$3.97^{+0.46}_{-0.42}$	$0.56^{+0.25}_{-0.20}$	$(0.15 \pm 0.03)10^{-3}$	364.28 ± 84.05

Tab. 4.3: The table reports spectral fit results: extraction rings in arcminutes *(Col. 1)*, projected temperature with fixed SP contribution *(Col. 2)*, metals abundance with fixed SP contribution *(Col. 3)*, together with the results for the calculation of deprojected electronic density calculated in Sec. 4.3.3 *(Col. 4)* and cooling time of Sec. 4.3.4 *(Col. 5)*.

brightness excess characterizing the central regions of cool-core clusters. Thus, a double β-model (LaRoque et al. 2006) of the form

$$\Sigma = \Sigma_{01}\left[1+\left(\frac{r}{r_{c1}}\right)^2\right]^{-3\beta_1+1/2} + \Sigma_{02}\left[1+\left(\frac{r}{r_{c2}}\right)^2\right]^{-3\beta_2+1/2} \tag{4.4}$$

where r_{c1},r_{c2} are the core radius and Σ_{01}, Σ_{02} are the central surface brightnesses of the two components, is fitted on the entire radial range. In this case the best fit parameters are $\Sigma_{01} = 0.56 \pm 0.05$, $r_{c1} = 189.62 \pm 0.41$, $\beta_1 = 2.17 \pm 0.91$ and $\Sigma_{02} = 0.35 \pm 0.04$, $r_{c2} = 257.04 \pm 0.25$, $\beta_2 = 0.80 \pm 0.04$ with $\chi^2/d.o.f \simeq 1.64$. The requirement of a second component is usually typical of relaxed systems.

From β and r_c obtained from fitting the surface brightness, under the assumption of

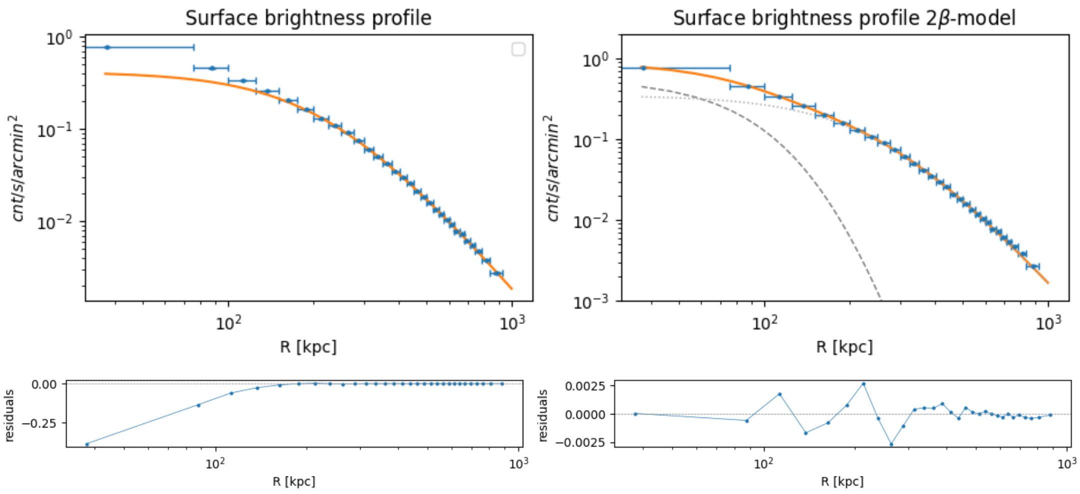

Fig. 4.12: Surface brightness profile, fitted with single β model (*left*) to the outer region ($> 1.3'$); and with the best fit double β model (*right*). In the latter case, the two components are also visible as dotted and dashed grey line.

spherical symmetry, the electron density profile can be extracted as

$$n_e(r) = \left\{ n_{e1}^2 \left[1 + \left(\frac{r}{r_{c1}} \right)^2 \right]^{-3\beta_1} + n_{e2}^2 \left[1 + \left(\frac{r}{r_{c2}} \right)^2 \right]^{-3\beta_2} \right\}^{0.5} \tag{4.5}$$

where n_{e1}, n_{e2} are the central densities of the two surface brightness components. These can be obtain by using the normalization factor $\mathcal{N}$ of the apec model

$$\mathcal{N} = \frac{10^{-14}}{4\pi \left[D_A (1+z) \right]^2} \int n_e n_H dV \tag{4.6}$$

where D_A is the angular distance of the source, n_e,n_H are the electron and proton densities in units of cm^{-3} and for a collisionally ionized plasma (e.g., Gitti et al. 2012) $n_H \sim 0.82 n_e$. $\mathcal{N}$ can be evaluated by fitting the spectra within a radius $R_{extr} = R_{500}$ and used to calculate

$$n_0 = \sqrt{\frac{10^{14}\, 4\pi (\Sigma_{12} LI_2 + LI_1) D_A \, D_L \, 0.82 \mathcal{N}}{\Sigma_{12} LI_2 \, EI_1 + LI_1 \, EI_2}} \tag{4.7}$$

where Σ_{12} is the ration of the central SB of component-1 to component-2; $\mathrm{EI_i}$ is the emission integral[13] for component-i and $\mathrm{LI_i}$ is the line emission measure[14] for component-i

---

[13] $EI = 2\pi \int \int x \left(1 + \frac{x^2 + l^2}{x_c^2} \right)^{-3\beta} dx dl$

[14] $LI = \int \left(1 + \frac{l^2}{x_c^2} \right)^{-3\beta} dl$

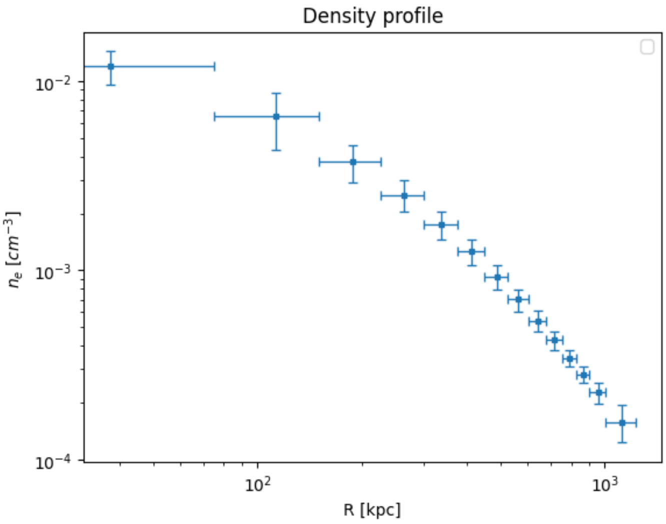

Fig. 4.13: Deprojected density profile calculated in the same spectral bins used for spectral fitting (*Col.1* of Tab. 4.3)

(precise calculation can be found Hudson et al. 2010). Finally

$$n_{e1}^2 = \frac{\Sigma_{12} LI_2}{\Sigma_{12} LI_2 + LI_1} n_0^2 \quad , \quad n_{e2} = \frac{\Sigma_{12} LI_1}{\Sigma_{12} LI_2 + LI_1} n_0^2 \tag{4.8}$$

and the deprojected density can be calculated using eq. 4.5. Results from the deprojection are listed in Tab. 4.3 and the density profile is shown in Fig. 4.13.

When the gas density and temperature profiles are known, the total mass within a radius r can be estimated by solving the equation of hydrostatic equilibrium and assuming spherical symmetry

$$M(<r) = -\frac{k_B T_g(r) r}{G \mu m_p} \left[\frac{d \ln n_e}{d \ln r} + \frac{d \ln T_g}{d \ln r} \right] \tag{4.9}$$

where k_B is the Boltzmann constant, $\mu \sim 0.6$ is the molecular wight in units of the proton mass m_p, and G is the gravitational constant. The mass profile has been calculated and the cluster mass within R_{500}[15] is $M_{500} = (5.99 \pm 0.46)\, 10^{14}\, M_\odot$, in good agreement with the total mass estimated with SZ data $M_{500} = (5.97 \pm 0.24)\, 10^{14}\, M_\odot$ (*Plank* collaboration et al. 2014).

4.3.4 Cooling time profile

From the temperature and density profiles, the cooling time of each region can be estimated as

$$t_{cool} = \frac{H}{\Lambda(T) n_e n_p} = \frac{\gamma}{\gamma - 1} \frac{kT(r)}{\mu X n_e(r) \Lambda(T)} \tag{4.10}$$

---

[15] it is the radius within which the mass density is 500 times of the critical density $\rho_c(z) = E^2(z) 3 H_0^2 (8G)^{-1}$, at the cluster redshift

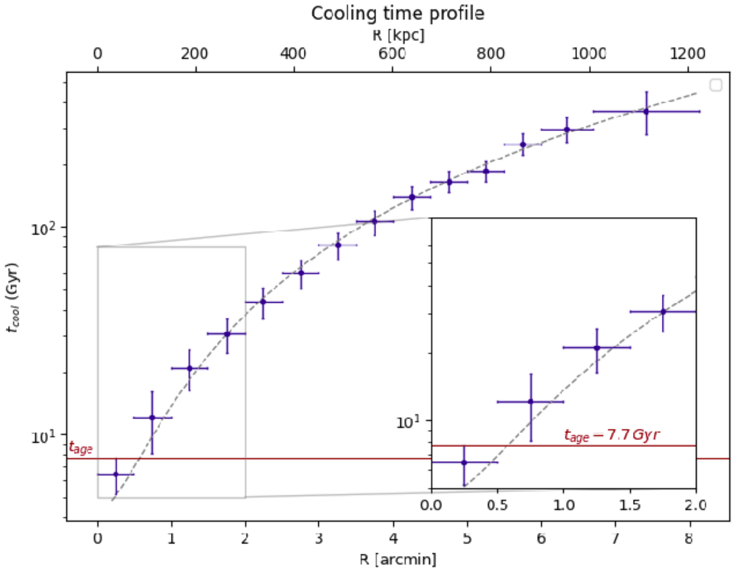

Fig. 4.14: Cooling time profile for A1413. Each point represents the cooling time for the annular region used for the spectral extraction. The blue line represents $t_{age} = 7.7\,Gyr$ while the grey line is the best fit $t_{cool} = 9.26\,r^{1.84}$

where $\gamma = 5/3$ is the adiabatic index, H is the enthalpy, $\mu \sim 0.6$ is the molecular wight for a fully ionized plasma and $\Lambda(T)$ is the cooling function (Sutherland&Dopita 1993). Results are listed in Tab. 4.3 and the cooling time profile is shown in Fig. 4.14. The cooling radius, i.e. the radius at which the cooling time is shorter than the age of the system, can be estimated assuming the cluster's age to be equal to the look-back time at z=1, because at this time many clusters appear to be relaxed: $t_{age} \simeq 7.7\,Gyrs$ (blue lines of Fig. 4.14). Thus, the cooling radius for A1413 is $\mathrm{r_{cool}} = 0.6\,\mathrm{arcmin} = 90\,\mathrm{kpc}$.

Hudson et al. 2010 argued that the central cooling time t_{cool} is the best parameter, for low-redshift clusters, to identify cool-core and non-cool-core clusters. They divided clusters into three types:

- $t_{cool} < 1\,Gyr$ for strong cool-core clusters
- $t_{cool} \sim 1 - 7.7\,Gyr$ defines weak cool-core clusters
- $t_{cool} > 7.7\,Gyr$ for non-cool-core clusters

Following the definition of a cool-core based on the cooling time given by Hudson et al. 2010, A1413 appears to be a weak cool-core clusters $t_{cool} = 6.44 \pm 1.29\,Gyrs$.

4.3.5 Morphological X-ray parameters

Moreover, another good check to investigate the dynamical state of a cluster is to determine some key X-ray morphological parameter (Sec. 2.5). Cassano et al. 2010 argued that the most sensitive parameters to the dynamical state of clusters are the **centroid shift** w (eq. 2.21) and **concentration parameter** c (eq. 2.20). Between the two there is an anti-correlation:

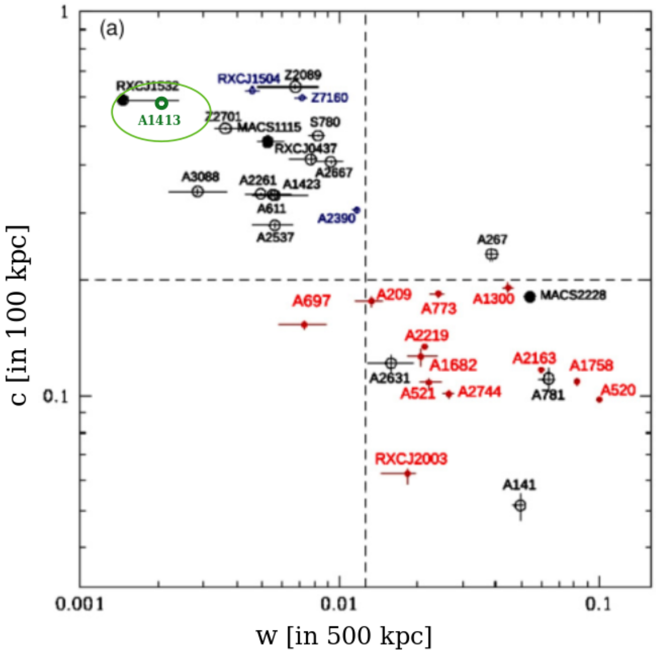

Fig. 4.15: Concentration parameter c vs. centroid shift w. Values $(w, c) = (2.7\,10^{-3};\ 0.6)$ obtained for A1413 (green point) compared with a sample of 67 galaxy clusters studied by Cassano et al. 2010 from GMRT RH Survey: radio-halos (red filled dots), no-radio halos (black open dots, mini-halos (blue open dots).

- relaxed clusters: low w, high c
- disturbed clusters: high w, low c

In its study, Cassano et al. 2010 found that the the median value of each parameter ($w \simeq 0.012, c \simeq 0.2$) splits the sample in radio halos and no-radio halos clusters. Moreover, they find no-radio halo cluster in the regions selected by $w < 0.012, c > 0.2$ (populated by relaxed clusters), while the fraction of radio halos increases to 73%–78% in the regions selected by w>0.012, c <0.2.

As shown in fig. 4.15, A1413 falls in the region of relaxed clusters $(w, c) = (2.7\,10^{-3};$ $0.6)$, which suggest A1413 being a cool-core cluster.

Despite being a very powerful tool, these morphological parameters are not always effective, and different study may report different limit values. For example, following the division of Lovisari et al. 2017, clusters classified as relaxed have a concentration higher than 0.15 and a centroid-shift value lower than $2.1{\cdot}10^{-3}$. In this case, A1413 would have a value $w = 2.1 \cdot 10^{-3}$ inconsistent with the classification. Moreover, one must consider that w is a parameter sensitive to the presence of substructures, identifying dynamically active systems. Hence, it can be that clusters, where an old merger occurred, developed a strong elliptical shape but still host a cool region in the center.

4.3.6 2D maps

Since A1413 appears to be a very peculiar cluster, a step forward in studying its dynamical state could be investigating its 2-dimensional spectroscopic properties to examine eventual particular features, that in the standard analysis wuold have gone unnoticed.

Using 2-dimensional maps of the main ICM properties is a very powerful tool to identify substructure, asymmetries and local variations (Zhang et al. 2009) that would be lost with azimuthally averaged profiles. As final step of the X-ray analysis, the 2D temperature, electron number density, entropy and pressure maps are created, based on the spectral measurements in each spatial bin.

The binning method used is the Weighted Voronoi Tesselations (WVT) Binning code (Diehl&Statler 2006), a spatially adaptive 2-dimensional binning algorithm, which makes use of Voronoi Tassellation to produce a very compact binning structure with a constant S/N per bin. Obviously, the higher the S/N ratio, the bigger the binned region, i.e. the "resolution" on which the spectral information are derived, decreases. Thus, to achieve a better compromise between S/N and resolution, maps are performed with S/N=50. As for the spectral profile, this allows that the 1σ uncertainty in the spectrally resolved temperature is $\sim$10% .

We use the background subtracted, exposure corrected image in [0.3-7] keV, presented in previous section, to determine the binned region, centered on the X-ray peak, and the same model described above to perform the spectral fitting within each region. In this case, each binned region is folded with ARF (since it varies a lot from on- to off-axis), while the RMF is calculated once and applied to all spectra to spare time. This has a low impact on the final map (see Lovisari et al., in prep), since RMF has a small spatial variation from on- to off-axis. Since all the main radio emission is within $0.5\,R_{500}$ (see section 5.4) the map shown in Fig. 4.16 are present inside that region.

The most clear evidence comes out from the temperature map, that appears very inhomogeneous, on the contrary to what expected from a relaxed cool-core cluster. Moreover, usually strong cool-core clusters present a central drop in temperature that would be reflected in a defined central region with lower temperature (Lovisari et al. 2011): this is not visible in Fig. 4.16c. If the object were totally relaxed, there would be few local variations. This suggests that some event in the past has perturbed the gas on large scale, giving rise to local turbulences.

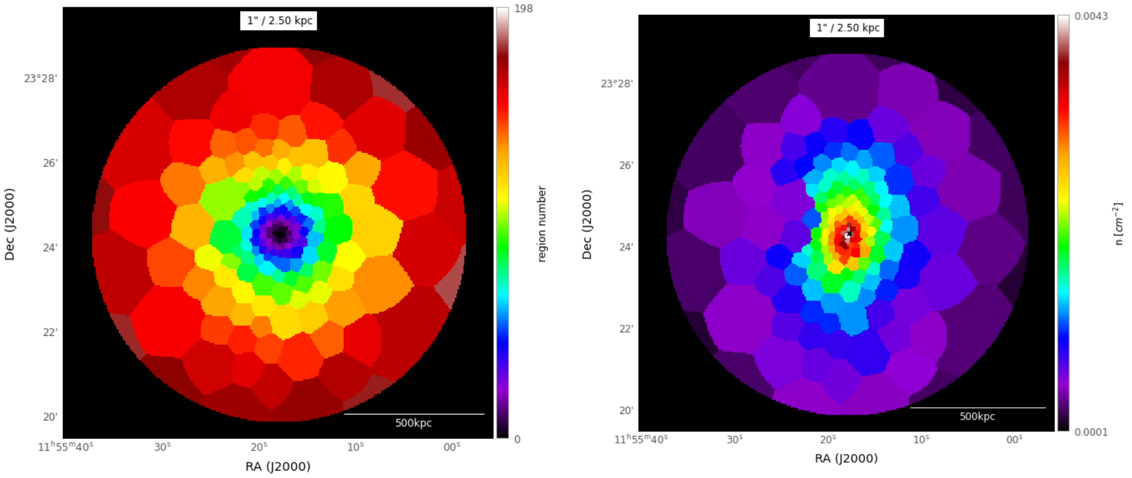

(a) 195 regions with S/N 50

(b) Density map

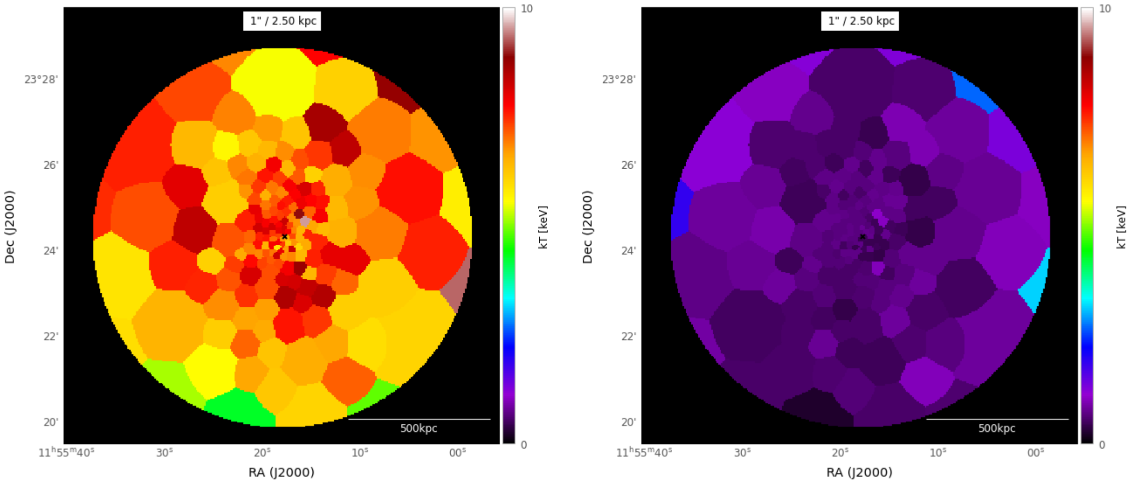

(c) Temperature maps

(d) Temperature error

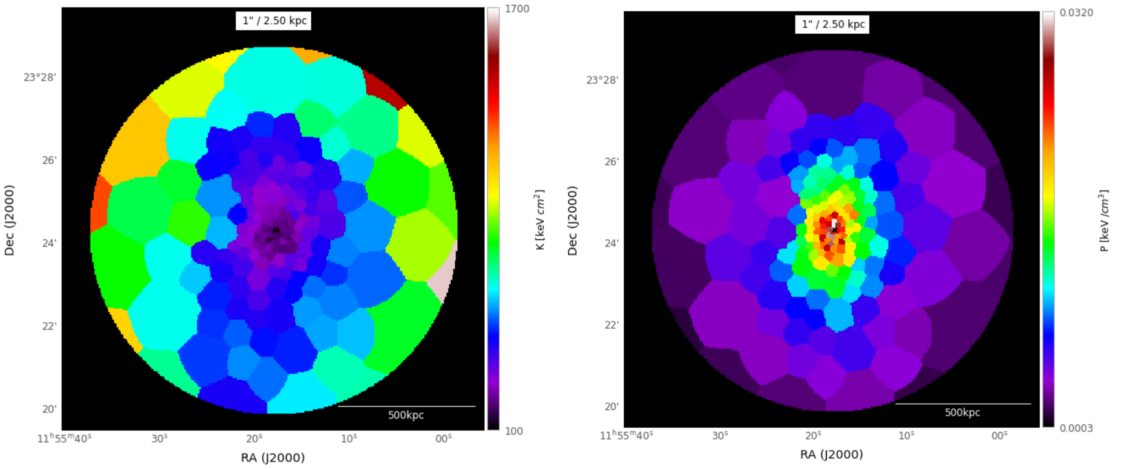

(e) Entropy map

(f) Pressure maps

Fig. 4.16: 2D maps, centered in Xray peak, obtained with S/N=50. Temperature, density, pressure and entropy are projected quantities.

Radio Analysis

In this chapter the main steps of the radio analysis are described. Before going into the details of the analysis, an overview of the radio fundamentals is given in Sec. 5.1. Then, in Sec. 5.2, the main characteristic of LOFAR are described. Finally, the process used to obtain the radio image is reported in Sec. 5.3, together with the main result of the analysis (section 5.4).

The aim of this part is to classify the nature of the radio source and define its properties.

5.1 Radio Fundamentals

Radio Astronomy is the study of radiation from celestial sources at frequencies between $\sim$ 10 MHz to 1 THz. The observing window (Fig. 5.1) is constrained by atmospheric refraction and absorption/emission: charged particles in the ionosphere reflects radio waves back into space at $<$ 10 MHz *(low-frequency cut-off)*; vibrational transitions of molecules have similar energy to infra-red photons and absorb the radiation at $>$ 1 GHz (completely by $\sim$ 300 GHz).

Radio telescopes are ground-based instruments and the radio range is so broad (5 decades in frequency) that different telescope technologies can be used.

Radio telescopes are receiving antennas, passive device that converts electromagnetic radiation in space into electrical currents in conductors.

An antenna can be used as a receiving or transmitting device. It is often easier to calculate the properties of transmitting antennas and to measure the properties of receiving antennas. Thus, thanks to the Reciprocity Theorem[1], the antenna properties can be calculated both in receiving and transmitting terms; in the latter case, the main pa-

---

[1] An antenna can be treated either as a receiving device, gathering the incoming radiation field and conducting electrical signals to the output terminals, or as a transmitting system, launching electromagnetic waves outward. These two cases are equivalent. For most radio astronomical applications is sufficient the *weak reciprocity theorem* that relates the angular dependences of the transmitting power pattern and the receiving collecting area of any antenna: “The power pattern of an antenna is the same for transmitting and receiving”

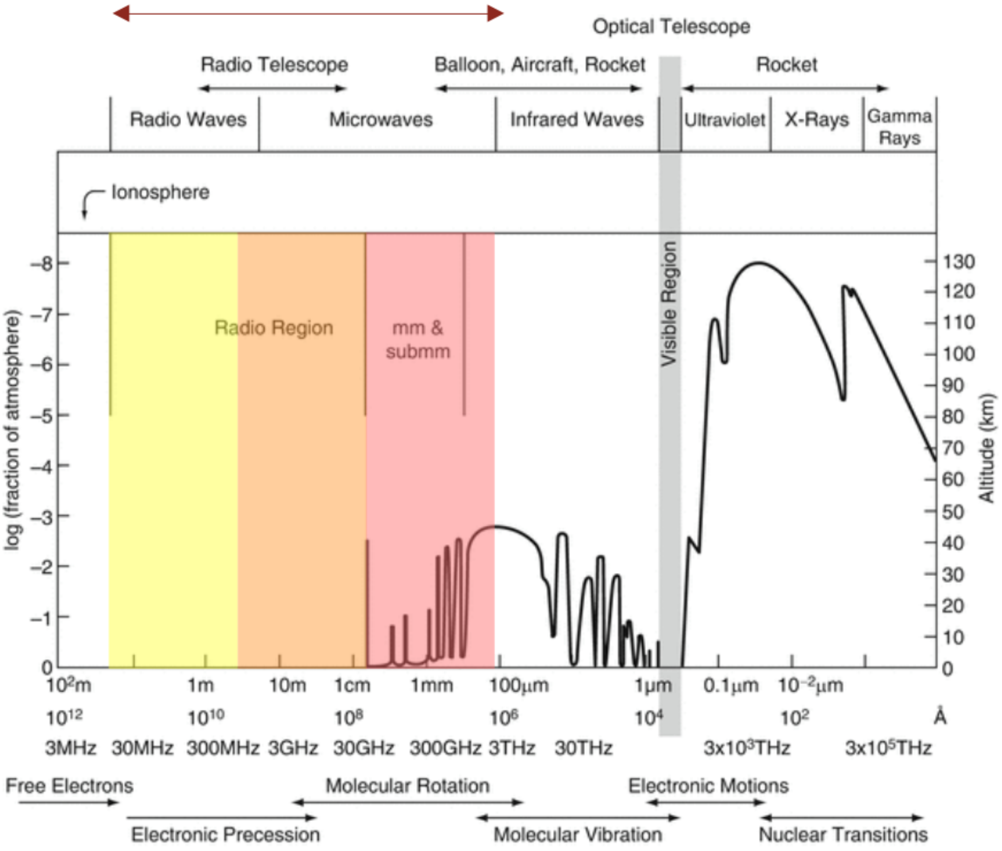

Fig. 5.1: Transmission through the atmosphere versus wavelength λ and frequency ν. The thick curve gives the fraction of the atmosphere (left vertical axis) and the altitude (right axis) needed to reach a transmission of 0.5, i.e. the boundary where the intensity of the radiation at each wavelength is reduced to half its original value. The fine scale variations in the thick curve are caused by molecular transitions. The thin vertical line on the left (∼10 MHz) marks the boundary where ionospheric effects prevents astronomical measurements. For example, from the thick curve, at $\lambda = 100\,\mu\text{m}$, one half of the astronomical signal penetrates to an altitude of 45 km. In contrast, at $\lambda = 10\,\text{cm}$, all of this signal is present at the earth's surface. Credits: adapted from Wilson et al. 2013

rameters are the power gain $G(\theta, \Phi)$, i.e. the power transmitted per unit solid angle in direction (θ, Φ) relative to an isotropic antenna, and the beam solid angle Ω_A, i.e. the angle within the antenna radiates most of its power.

The main parameters defining a receiving antenna are the *effective area*[2] $A_e(\theta, \Phi)$ and the *beam solid angle*. The average effective collecting area A_e of an antenna whose output spectral power is P_ν, in response to an unpolarized point source of total flux density S_ν, is defined by

$$\langle A_e \rangle = \frac{\lambda^2}{4\pi} \tag{5.1}$$

which implies that all lossless antennas, from tiny dipoles to the 100-m diameter Green Bank Telescope (GBT), have the same average collecting area, for a given observation

---

[2] The receiving counterpart of transmitting power gain is the effective area.

frequency.

In general, a lossless receiving antenna, having maximum effective collecting area A_0, receives most of the power into a beam solid angle defined as

$$\Omega_A = \frac{\lambda^2}{A_0} \tag{5.2}$$

The larger peak collecting area A_0, the smaller beam solid angle Ω_A. Thus, A_e quantifies how much directional an antenna could be.

5.1.1 Reflector Antennas

Traditional radio telescopes use large reflectors to collect and focus power onto their small feed antennas, such as wave guide horns or dipoles backed by small reflectors, that are connected to receivers, which amplifies and converts them to electrical signals. The most common reflector shape is a paraboloid of revolution because it can focus the plane wave from a distant point source onto a single focal point. This is the configuration of the conventional *single-dish radio telescope.* Even if these are not the kind of radio telescopes used by LOFAR (see Sec. 5.2, this configuration is useful to understand the working principle and the main relations that can be applied to all radio telescopes.

The *beam pattern*, or power gain as a function of direction, of an aperture antenna be calculated applying the Far Field approximation[3] and making use of the reciprocity theorem,i.e. by first calculating the beam pattern of a transmitting paraboloid and then extending the reasoning in the receiving case (precise step-by-step calculation can be found in Condon and Ransom 2015). Considering a one-dimensional aperture of width D, whose transmitting feed illuminates the aperture with an electric field strength $g(x)$ that varies across the aperture (see Fig. 5.2 left). The total electric field $f(l)$ produced by the whole aperture at large distances ($R \gg R_{ff}$) and at an angle θ with respect to the normal, is just the vector sum of the elemental electric fields df from each element extending from x to $x + dx$:

$$f(l) = \int_{aperture} g(u) e^{-i2\pi lu} du \tag{5.3}$$

where $l = \sin\theta$ and $u = x/\lambda$ is position along the aperture in wavelength units. In words, in the far field, the electric-field pattern $\{(\updownarrow)$ of an aperture antenna is the Fourier Transform (FT) of the electric field distribution $\}(\sqcap)$ illuminating that aperture: $\{(\updownarrow) = \mathcal{FT}(\}(\sqcap))$.

---

[3] The far-field radius R_{ff} define the distance where a point source must be, for the received waves to satisfy the assumption that they are nearly planar across the reflector

Then, following the definition of the Pointing flux $\langle S\rangle = c\langle E_{\perp}^2\rangle/4\pi$, the *power pattern* $P(l)$ is proportional to the square of the electric field pattern $P(l) \propto f^2(l)$.

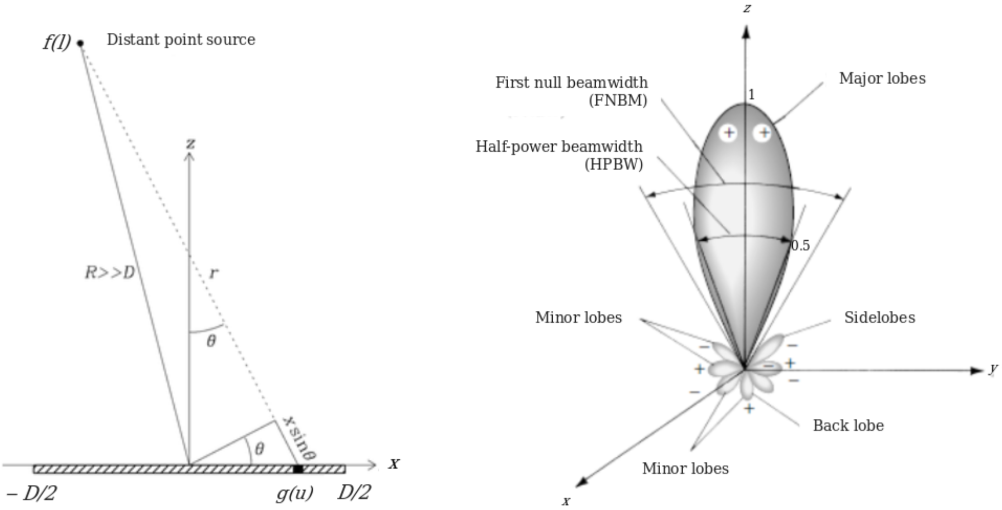

Fig. 5.2: *Left:* Coordinate system for a one-dimensional linear aperture spanning $-D/2 < x < +D/2$; *Right:* Radiation lobes and beam widths of an antenna power pattern.

For the simplest case of a uniformly illuminated[4] one-dimensional aperture of width D at wavelength λ, when $l = sin\theta \sim \theta$ for $\theta \ll 1$, the power pattern turns into:

$$P(\theta) = \Big(\frac{D}{\lambda}\Big)^2 sinc^2\Big(\frac{\theta D}{\lambda}\Big) \tag{5.4}$$

It follows the sinc function and the central peak of the power pattern between the first zeros is called the *primary beam*, while the smaller peaks are the *sidelobes* (Fig. 5.2 right). They are separated by zeros in the power pattern at the angles $\theta \sim \pm\lambda/D,\ \pm 2\lambda/D$ etc. Radio astronomers use the angle between the half-power points to specify the angular width of the main beam, calling it the half-power beamwidth (HPBW) or the full null beamwidth (FNBW), when considering angle separated between first nulls in the patterns.

In this case, satisfying $P(\theta_{HPBW}/2) = 1/2$, the angle between two directions having radiation intensity equal to 0.5 of the beam maxim can be found $\theta_{HPBW} \sim 0.89\lambda/D$.

The general scaling relation is

$$\theta_{HPBW} \propto \frac{\lambda}{D} \tag{5.5}$$

where the constant of proportionality varies slightly with the illumination taper (e.g. for cosine-tapered field pattern, $\theta_{HPBW} \sim 1.2\lambda/D$).

---

[4] strength of the illumination is constant over the aperture $g(u) = constant$, with $u \in (-D/2\lambda, +D/2\lambda)$

The receiving HPBW is sometimes called the *resolving power* of a telescope because two equal point sources separated by the HPBW are just resolved by the Rayleigh criterion. In other words, it can be considered the radio counterpart of the PSF.

5.1.2 Interferometer

Large single-element radio telescopes can be constructed cheaply, but have relatively low angular resolution (eq. 5.5) and pointing accuracy, small field-of-view ($\sim \lambda/D$, consisting of only one or several beams), and limited sensitivity. The largest fully steerable dish has diameter D=100 m and its angular resolution is approximately 17” at 7-mm wavelength, so impossibly large diameters would be needed to achieve sub-arcsecond resolution (reached for example by optical instruments) at radio wavelengths. Interferometric techniques have been developed to combine several single-element telescopes into a *multi-element array.* In this way, radio interferometry can provide the highest angular resolution imaging possible in astronomy.

The simplest radio interferometer is a pair of radio telescopes whose voltage outputs are correlated (multiplied and averaged). Even the most elaborate interferometers with N$\gg$2 antennas, often called elements, can be treated as $N(N-1)/2$ independent two-element interferometers, so a basic understanding of this simple case is essential.

Considering two identical dishes, pointing in the same direction specified by the unit vector $\hat{s}$, separated by the baseline vector $\vec{b}$, as show in Fig. 5.3. Consider for simplicity, a quasi-monochromatic interferometer, one that responds only to radiation in a very narrow band τ_g centered on frequency $\nu = \omega/2\pi$. Then the time averaged output voltages of antennas $V_1 = V \cos\omega[(t-\tau_g)]$, $V_2 = V\cos(\omega t)$ at time t is:

$$R = \langle V_1 V_2 \rangle = \frac{V^2}{2}\cos(\omega\tau_g) \tag{5.6}$$

where the term $\tau_g = \vec{b}\cdot\hat{s}/c$ in the geometric delay, due to the extra distance that plane waves from a distant point source must travel to reach the first antenna (see Fig. 5.3).

The correlator output voltage R varies sinusoidally as the Earth’s rotation changes the source direction relative to the baseline vector. These sinusoids are called *fringes*, and the fringe phase is

$$\Phi = \omega\tau_g = \omega\frac{b\cos\theta}{c} \tag{5.7}$$

Since $d\Phi/d\theta = -2\pi(b\sin\theta/\lambda)$, the fringe period $\Delta\Phi = 2\pi$ corresponds to an angular shift $\Delta\theta = \lambda/(b\sin\theta)$.

The response R_c of the quasi-monochromatic two-element interferometer with a “cosine” correlator to a spatially incoherent slightly extended (much smaller than the primary beamwidth) source with sky brightness distribution $I_\nu(\hat{s})$ near frequency $\nu = \omega/2\pi$) is obtained by treating the extended source as the sum of independent point sources: $R_c = \int I(\hat{s})\cos(2\pi\nu\vec{b}\cdot\hat{s}/c)\,d\Omega$.

Moreover, like any real function, the source brightness distribution can be written as the sum of even and odd (antisymmetric) parts: $I = I_E + I_O$. In that case even cosine function R_c, sensitive only to the even part I_E, is not enough. To detect the odd part I_O, a "sine" correlator whose output is odd, $R_s = \int I(\hat{s})\sin(2\pi\nu\vec{b}\cdot\hat{s}/c)\,d\Omega$ is needed.

The combination of cosine and sine correlators is called a *complex correlator* and its output consists in the *complex visibility*

$$\mathcal{V} \equiv R_c - iR_s = Ae^{i\Phi} = \int I(\hat{s})exp\big\{-i2\pi\vec{b}\cdot\hat{s}/\lambda\big\}d\Omega \tag{5.8}$$

where $A = \sqrt{R_c^2 + R_s^2}$ is the visibility amplitude and $\Phi = \tan^{-1}(R_s/R_c)$ the visibility phase.

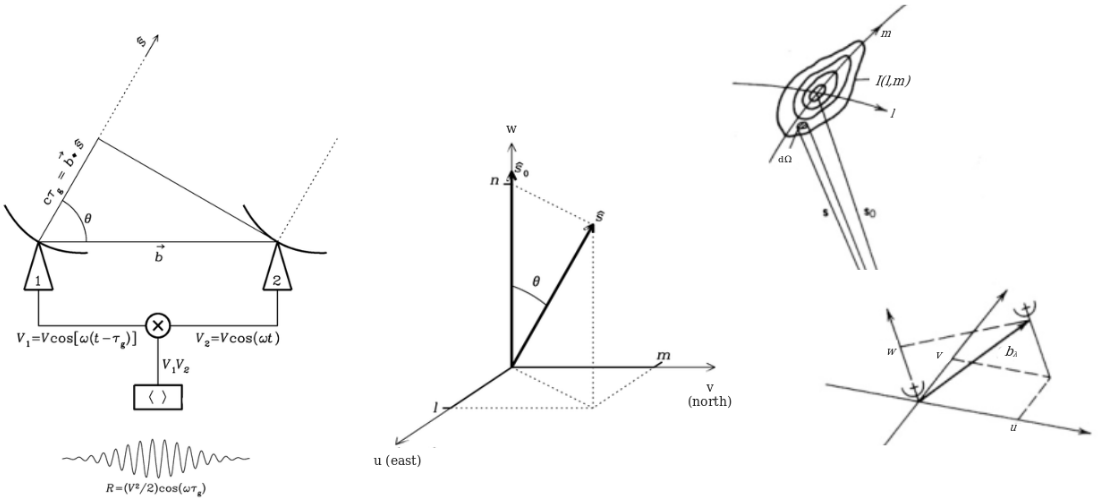

Fig. 5.3: *Left:* Components of a two-element quasi-monochromatic multiplying interferometer. The output voltages V_1 and V_2 are amplified, multiplied ($\times$), and time averaged ($\langle\rangle$) by the correlator to yield an output of amplitude R. The quasi-sinusoidal output fringe shown occurs if the source direction in the interferometer frame is changing at a constant rate $d\theta/d$t. Credit: Condon and Ransom 2015. *Middle:* The (u, v, w) coordinate system for interferometers. The w-axis points in the reference direction $\hat{s}_0$ usually containing the source to be imaged. Projected onto the plane normal to the w-axis, u is the east–west baseline in wavelengths and v is the north–south baseline in wavelengths. l, m, and n are projections of the unit vector $\hat{s}$ onto the u-, v-, and w-axes, respectively. Credit: Condon and Ransom 2015. *Right:* Geometric relationship between a source under observation $I(l, m)$ and an interferometer or one antenna pair of an array. The antenna baseline vector, measured in wavelengths, has length b_λ and components (u, v, w) Credit: Thompson et al. 2007

Interferometers in Three Dimensions

As previously done when dealing with single antennas (eq. 5.3), it is convenient to write baseline vector $\vec{b}$ in three dimensions, using the (u, v, w) coordinate system, i.e. expressing the baseline vector in wavelength units. As shown in Fig. 5.3 the w-axis is in the reference direction $\hat{s}_0$ usually chosen to contain the target radio source, while the u- and v-axes point east and north in the (u,v) plane normal to the w-axis. An arbitrary unit vector $\hat{s}$ has components (l, m, n), called direction cosines, with $n = \sqrt{1 - l^2 - m^2}$, defining position in the sky. With this coordinate system $d\Omega = dldm/\sqrt{1 - l^2 - m^2}$, and therefore the 3D generalization of eq. 5.8 becomes:

$$\mathcal{V}(u, v, w) = \int\int \frac{I_\nu(l, m)}{\sqrt{1 - l^2 - m^2}} exp\Big\{ - i2\pi(ul + vm + wn)\Big\} dl\, dm \tag{5.9}$$

Note that this is not a three-dimensional Fourier Transform. However, we can get a 2D FT if the third term in the phase factor is sufficient small:

$$w(1 - \sqrt{1 - l^2 - m^2}) = w(1 - \cos\theta) \sim w\frac{\theta^2}{2} \ll 1 \tag{5.10}$$

In this case, eq. 5.9 becomes a two-dimensional Fourier transform, which can be inverted to give the source brightness distribution in terms of the measured visibilities:

$$I_\nu(l, m) \approx \int\int \mathcal{V}(u, v, 0)\, exp\Big\{ + i2\pi(ul + vm)\Big\} dl\, dm \tag{5.11}$$

This is the fundamental relation between interferometer response (complex visibility) and sky surface brightness, largely used during imaging (Sec. 5.3): visibility as a function of baseline coordinates $\mathcal{V}(u, v)$ is the Fourier transform of the sky brightness distribution as a function of the sky coordinates $I(l, m)$.

This condition is always satisfied for small FoV, where the approximation of the 3D celestial sphere to a 2D plane still holds. Instead, for large FoV, the w-term is not negligible and other techniques (e.q. the *w-stacking* method, described in §5.3.2) must be used, to be able to apply the FT and obtain the surface brightness from the data visibilities.

The power pattern of 2 directional antennas interferometer can be calculated by extending the reasoning of one single antenna (§5.1.1) and making use of the FT convolution therorem[5]. In this case, the 2 antennas can be treated as two uniformly illuminated one-dimensional aperture of width D at a distance b, i.e. [the electric field $g(u)$ can be model through] a convolution between a double pulse[6] with a rectangle function. Thus,

---

[5] The convolution theorem states that the Fourier transform of the product of two functions is the convolution of their Fourier transforms.

[6] Isotropic antennas can be considered as delta functions and the interferometer point-source response would be a sinusoid spanning the sky.

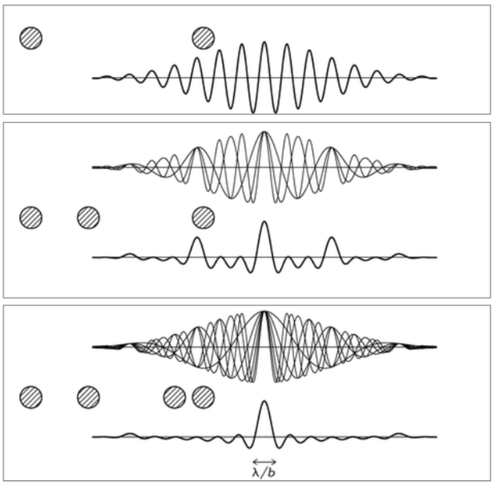

Fig. 5.4: The instantaneous point-source responses of interferometers with overall projected length b and two, three, or four antennas distributed as shown are indicated by the thick curves. The synthesized primary beam of the four-element interferometer is nearly Gaussian with angular resolution $\theta \sim \lambda/b$

the power pattern of a 2-elements interferometer is the product of the corresponding FT, that is the product cosine and sinc function:

$$P(\theta) \propto cos^2\Big(\pi \frac{b}{\lambda} cos\theta\Big)\, sinc^2\Big(\pi \frac{D}{\lambda} cos\theta\Big) \tag{5.12}$$

The sinc term is determined by the single antenna aperture D and set the scale of the field of view $FOV \sim \lambda/D$: smaller antennas diameter means larger FOV, and vice versa. The primary beam, instead, is governed by cosine term and, differently from eq. 5.5, it is inversely proportional to the baseline size in wavelenghts:

$$\theta_{HPBW} \propto \frac{\lambda}{b} \tag{5.13}$$

Thus, interferometry allows a big enhancement to the resolution of the radio telescopes, and therefore the FOV will contain more (about $(b/D) \gg 1$) resolution elements.

Note that the fringes of the power pattern can be seen as sensitivity to a given angular scale. Thus, the interferometer with directive antennas responds to a finite range of angular frequencies centered on $bsin\theta/\lambda$. The instantaneous point-source response pattern of an interferometer can be improved by adding more Fourier components, that is, more baselines. The synthesized beam of the multielement interferometer, obtained by averaging the outputs of all N(N-1)/2 two-element interferometers, rapidly approaches a Gaussian as N increases, as show in Fig. 5.4.

Finally, because the antenna diameters D must be smaller than the baseline b (otherwise, the antennas would overlap), the angular frequency response cannot extend to zero, which means that the interferometer cannot detect an isotropic source, like the 3K CMB. Given a specific array configuration, the interferometer is just sensitive to angular scales in a given range

$$\theta \in \Big[\frac{\lambda}{b_{max}}, \frac{\lambda}{b_{min}}\Big] \tag{5.14}$$

where λ/b_{min} is called *maximum recoverable scale* that the radio interferometer can detect.

5.2 About LOFAR

LOFAR, the LOw-Frequency ARray, is a new-generation radio interferometer, constructed in the north of the Netherlands and across Europe, which covers the low-frequency range of the electromagnetic spectrum, from 10-240 MHz, i.e. 30-1.2 m (Haarlem et al. 2013). It is made up of two types of antennas, the Low Band Antennas (LBAs) and High Band Antennas (HBAs), that together form a so-called station.

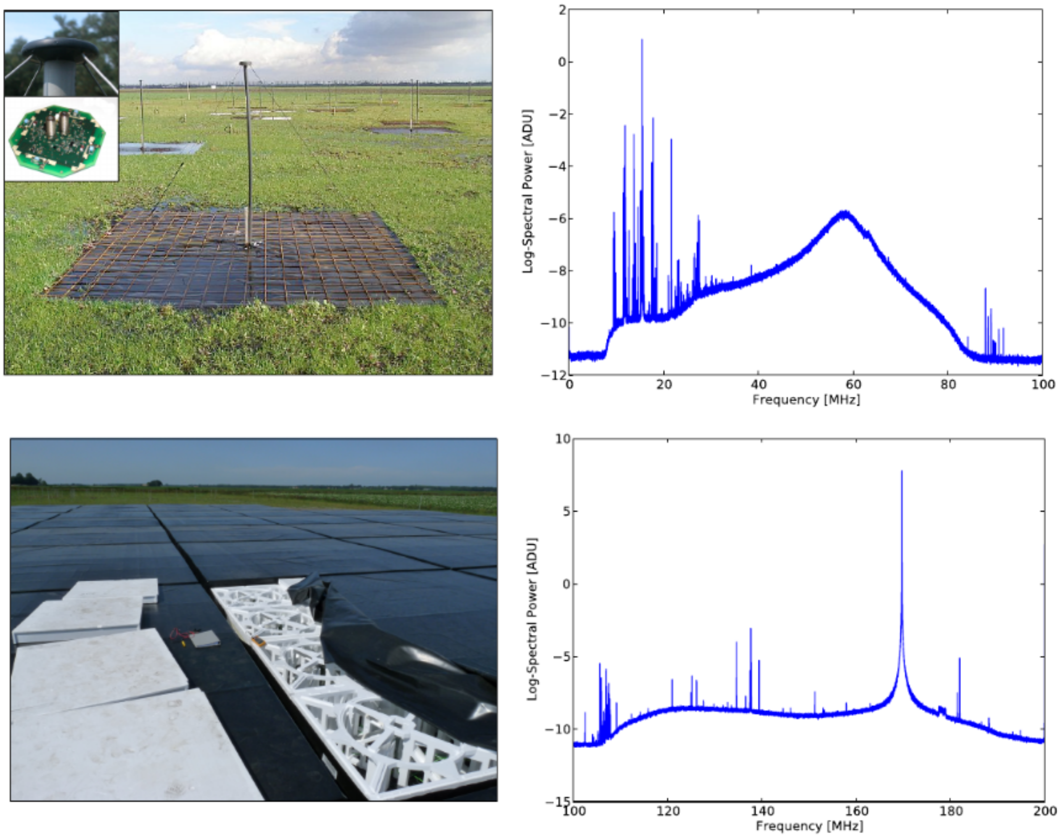

Fig. 5.5: *Top left*: image of a single LOFAR LBA dipole including the ground plane. *Top right*: median averaged spectrum for all LBA dipoles in one core station. The peak of the dipole response at 58 MHz is clearly visible as well as strong RFI below 30 MHz, partly because of ionospheric reflection of sub-horizon RFI back toward the ground, and above 80 MHz, due to the FM band. *Bottom left*: closeup image of a single LOFAR HBA tile. The protective covering has been partially removed to expose the actual dipole assembly. *Bottom right*: median averaged spectrum for all HBA tiles in one core station. Various prominent RFI sources are clearly visible distributed across the band including the strong peak near 170 MHz corresponding to an emergency pager signal. Credit: Haarlem et al. 2013.

LBAs are designed to operate from the atmospheric spectral cutoff of the "radio window" at 10 MHz up to the onset of the commercial FM radio band at 90 MHz. Due to the presence of strong radio frequency interference (RFI) at the lowest frequencies and the proximity of the FM band at the upper end (see 5.5, top right), this range is operationally limited to 30–80 MHz by default. One LBA element consists of a simple dipole, sensitive to two orthogonal linear polarizations (X and Y), and places above a conducting ground plane with the wires at an angle of 45 degrees with respect to the ground.

HBAs, instead, are designed to operate in the frequency range between 120 and 240 MHz. At these frequencies, sky noise no longer dominates the total system noise, as is the case for the LBAs. Consequently, a different design was required to minimize contributions to the system noise due to the electronics (see Fig. 5.5, bottom row). Each HBA "tile" is an assembly of 16 bow-tie-shaped dual dipole antennas arranged in a 4x4 grid.

As mentioned before, LOFAR consists of stations of clustered LBAs and HBAs. There are three kinds of LOFAR station layouts with individual characteristics (different antenna field configurations and underlying electronics), which, according to their distance from the centre of the array, are classified as *Core*, *Remote* or *International stations*.

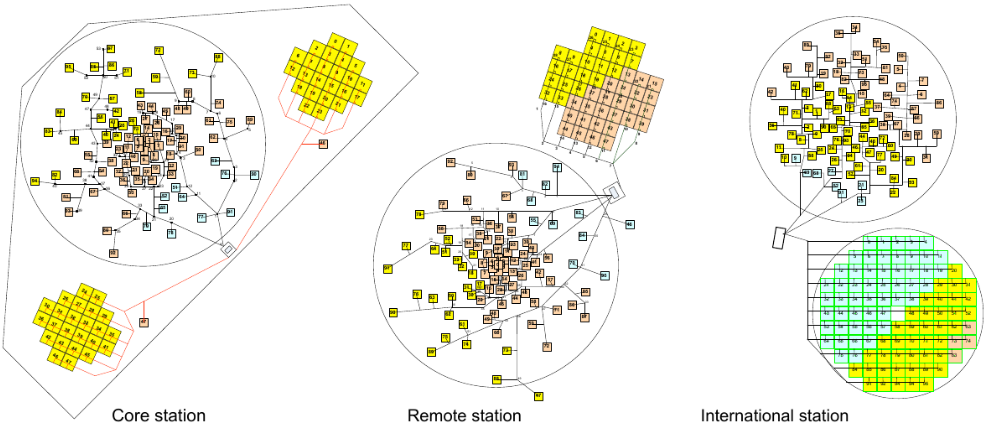

Fig. 5.6: Station layout diagrams showing core, remote and international stations. The large circles denote the LBA antennas while the arrays of small squares indicate the HBA tiles. Note that the station layouts are not shown on the same spatial scale. Credits: Haarlem et al. 2013

LOFAR antenna stations perform the same basic functions as the dishes of a conventional interferometric radio telescope. However, unlike previous generation high-frequency radio telescopes, the antennas within a LOFAR station do not physically move. Instead, pointing and tracking are achieved by combining signals from the individual antenna elements[7] to form a phased array using a combination of analog and digital beam forming techniques (see Thompson et al. 2007). Thus, station-level beam-forming allows for rapid repointing of the telescope as well as the potential for multiple, simultaneous observations from a given station.

---

[7] Combining different antenna in this way forms an *aperture array*: the receiving elements are added together by taking into account the delay due to the waves arriving at different times, from different directions.

Moreover, a number of different types of beam must be considered when dealing with the LOFAR telescope (Fig. 5.7). LOFAR beam-forming is hierarchical in nature - forming first beams at HBA tile level, then station level, and then array level - so the picture can be confusing if one is not completely clear on what 'beam' is meant in a particular situation.

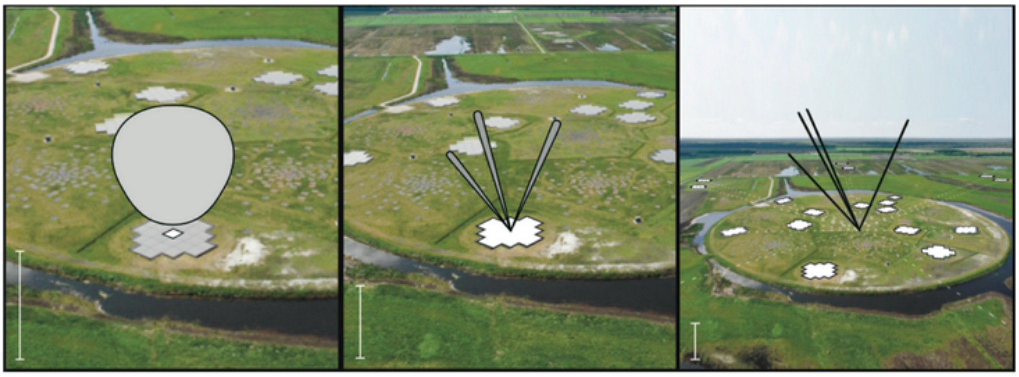

Fig. 5.7: Different types of beam used in LOFAR observations. *Left*: Dipole or tile beam; *Middle*: Station beam or sub-array pointing; *Right*: Tied-array beams. Credit: *ASTRON-WebSite* n.d.

Dipole and Tile Beams

LBA antennas are sensitive to the entire visible sky, so the LBA 'dipole beam' covers the entire sky, but with a significant drop in sensitivity below about 30° elevation.

Each HBA 'tile beam' (sometimes called the 'analogue beam') is formed by combining the signal from these 16 antenna elements in phase for a given direction in the sky (Fig. 5.7, left). Thus, in turn, the field of view is limited to 30-15 degrees at the FWHM of the beam over the frequency range 110-240 MHz.

Station Beam or Sub-Array Pointing (SAP)

A 'station beam', also known as a 'sub-array pointing' (SAP) is formed by combining, with the appropriate phase-rotation, all the selected LBA antennas or HBA tiles in a given station to form a beam towards a specified direction (Fig. 5.7, middle). A particular configuration of HBA tiles is the *HBA-dual*, where the data from each HBA field in a core station (Fig. 5.6, left) are correlated as separate stations in the correlator. This configuration provides many more short baselines in the core (i.e. major sensitivity to extended emission on scales $\sim$1 deg).

Beam-forming is done independently for each subband and the resulting beam of each subband is referred to as a "beamlet". Multiple beamlets with the same pointing position are summed to produce beams with a larger bandwidth. Thus the available bandwidth (up to 488 subbands in 8-bit mode) has to be distributed over all the specified station beams. For example, if 8 station beams are specified with equal subbands, the total number of subbands per individual station beam should not be more than 61.

Tied-Array Beams (TABs)

Each SAP returned from multiple core stations can be combined coherently to form multiple tied-array beams (Fig. 5.7, right), each with a different pointing direction within the overall station beam but covering the same range of subbands as the SAP.

Stations throughout Europe comprise a large range of baselines $\sim 50\,\mathrm{m}$ to $\sim 2000\,\mathrm{km}$, and thus a resolution spannig between few degrees to sub-arcsec.

5.3 LOFAR data analysis

The data used in this work are part of the LOFAR Two-metre Sky Survey (LoTSS, Shimwell et al. 2019), a sensitive ($\mathrm{rms} \sim 100\mu\mathrm{Jy/beam}$), high-resolution (FWHM of the synthesised beam of ~ 6"), low-frequency (120-168 MHz) radio survey of the northern sky.

LoTSS observations are conducted in the HBA DUAL INNER configuration, with 8 hrs observing time and a frequency coverage of 120-168 MHz (central frequency of 144 MHz, i.e. 2 m wavelenght). By exploiting the multi-beam capability of LOFAR and observing in 8-bit mode two pointings are observed simultaneously.

Data calibration with LOFAR comprises different steps which can be summarised as follows. Since visiblities are complex numbers, both amplitude and phase must be calibrated for each antenna as a function of time. The correction factors, *amplitude gains*, to set the absolute flux-scale are computed using a flux calibrator, i.e. a powerful, stable, well known source, under the assumption that the flux density of the calibrator will not change significantly over the time of the observation.

Instead, the phase-calibration at low frequency (below 1 GHz) must take into account several factors, and can not be performed using a nearby phase-calibrator as done at higher frequencies. Below, we will summarise the main differences with respect to observations conducted ay higher frequencies.

First of all, the FoV is large (about 3° radius at 144 MHz) making it almost impossible to find sources with the properties that would be needed by a phase calibrator. In addition, and more importantly, at these frequencies the very variable ionosphere introduces a differential phase delay that changes both in space and time. Typically, one needs ~ 40 different spatial corrections over a LoTSS pointing area, that must be tracked with a 10s solution interval (Mevius et al. 2016).

Therefore, two type of calibrations are executed: the Direction-Independent calibration, that uses a phase sky model obtained with data from other survey working at similar frequency (e.g. GMRT); and a Direction-Dependent calibration (DDE), that splits the images in different regions, called "facets", and achieves a further "localized" phase and amplitude correction, in order to take into account variation across the FoV.

A1413 falls in two pointings of the survey, namely $\mathrm{P}\,177 + 22\_\mathrm{PSZG}226.18 + 76.79$, and $\mathrm{P}\,180 + 22\_\mathrm{PSZG}226.18 + 76.79$, that must be properly combined. Data were prepared by LoTSS-DR2 pipeline (Shimwell et al., in prep), which works on the direction-independent calibration products (i.e. 25 measurament sets for each pointing, that cover the 120-168 MHz band) and returns fully direction-dependent calibrated data.

After calibration, the so called "extraction and self-calibration" procedure is performed: a region around the target of interest in selected and all the sources outside that region are subtracted using the direction-dependent gains obtained by the pipeline. The station beam is corrected for directly in the visibility space, and the phase center of the observation is shifted toward the direction of the target. This way, we are left with 2 data sets centered on the target that do not need any further beam correction. These 2 data sets are self-calibrated again to obtained ad-hoc calibration solutions in the region of interest.

The work carried out here, starts from extracted and self-calibrated data, and consists in imaging the target at high and low resolution to classify the kind of radio emission and its properties. The software WSClean (§5.3.2) is used for imaging.

Fig. 5.8 shows the LoTSS image centered on A1413 (LoTSS DR2, Shimwell et al., in prep). It is evident that, apart from discrete point sources and residual calibration errors, the cluster shows diffuse emission well beyond the center, that we investigate in the next sessions.

5.3.1 Imaging

Imaging consists in obtaining the surface brightness distribution $I_\nu(l, m)$ from the output interferometric data, the complex visibilities.

As defined in eq. 5.9, $\mathcal{V}(u, v)$ should consist in a continuous function in the (u,v) plane. Actually, for a real array, comprising of a finite number N of element (finite number of baselines), the true continuous visibility function $\mathcal{V}$ is not available: only samples of the visibility function can be obtained, at discrete locations in the Fourier plane.

Moreover, in order to have a good image of the radio source, a good coverage of the (u,v) plane is required. This can be achieved through the technique of the *Earth-rotation aperture synthesis*: the Earth's rotation varies the projected baseline coverage of an interferometer whose elements are fixed on the ground, and thus, increasing the sampling of the (u,v) plane. The (u,v) coverage will result in a number of different ellipses having the same shape and will increase the number of Fourier components to which the interferometer is sensitive.

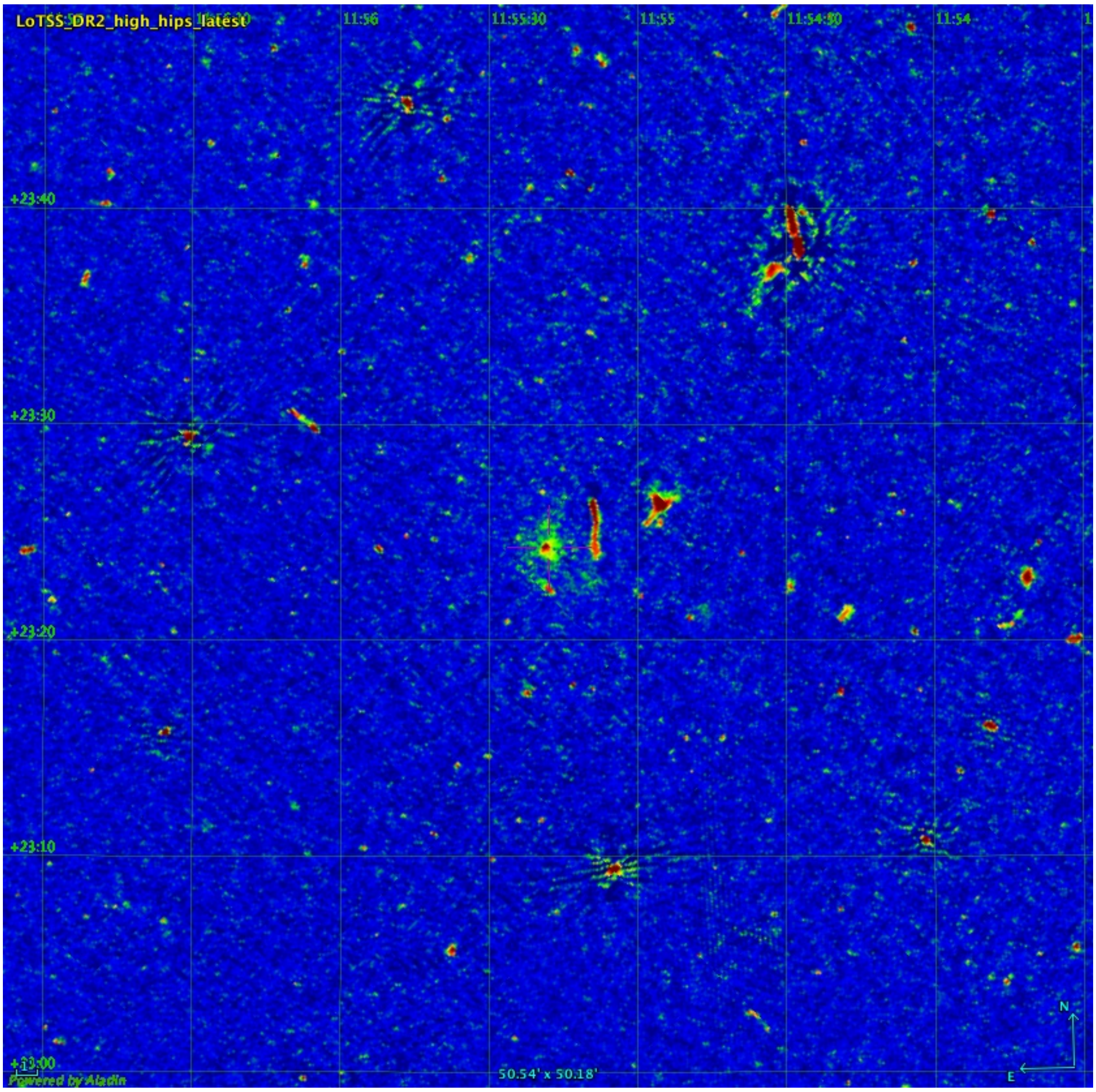

Fig. 5.8: Mosaic of the two pointing of the target A1413 from LoTSS-DR2 (Shimwell et al., in prep).

Generally speaking, $\mathcal{V}(u,v)$ samples are limited by the number of antennas and Earth-sky geometry: one pair of antennas correspond to two (u,v) samples at a time[8]; N antennas to N(N-1) samples at a time and using the *Aperture Synthesis technique*, the (u,v) plane can be filled even more, over time.

The radio data set is composed by sampled visibilities defined as $\{S(u,v)\cdot\mathcal{V}(u,v)\}$, where $S(u,v)$ is the sampling function, i.e. the function that represent the (u,v) coverage:

$$S(u,v) = \sum_{i}^{N(N+1)/2} \delta(u-u_i)\,\delta(v-v_i) \tag{5.15}$$

As mentioned in Sec. 5.1.2, if eq. 5.10 holds, by inserting the sampled visibility into the Fourier inverse, the so-called Dirty Image can be obtain

$$S(u,v)\cdot\mathcal{V}(u,v) \xrightarrow{FT^{-1}} I^D(l,m) \quad ; \quad I^D(l,m) \xrightarrow{FT} S(u,v)\cdot\mathcal{V}(u,v) \tag{5.16}$$

Applying the convolution theorem from Fourier transform theory, the dirty image $FT^{-1}\{S(u,v)\cdot\mathcal{V}(u,v)\}$, can be written as the convolution of the true image $I(l,m)$ with a Dirty beam $B(l,m)$

$$I^D(l,m) = FT^{-1}\{S(u,v)\} * FT^{-1}\{\mathcal{V}(u,v)\} = B(l,m) * I(l,m) \tag{5.17}$$

The classical Högbom's CLEAN algorithm (Högbom 1974,1983), is a purely image-domain algorithm that forms the basis for most deconvolution algorithms used in radio interferometry. It finds a solution to the convolution equation by positing a model for the true sky brightness, based on the a priori assumption that the sky intensity distribution can be treated as a collection of point sources, i.e. sum of δ functions.

The algorithm proceed iteratively as follows:

- Find the localization of the strongest intensity pixel in the dirty map $\max(\left|I^D\right|)$: it gives the location and strength of a potential point source
- Add a fraction $\gamma \simeq 0.1-0.2$, called *loop gain*, of this peak $\gamma\cdot\max\left|I^D\right|$ and its spatial position to the model I^C, which will become a list of the clean components
- Convolve $\gamma\cdot\max\left|I^D\right|$ by the dirty beam and subtract the resulting convolution from the dirty map in order to clean out the side lobes associated to the localized clean component. The result of this operation is the *Residual Image*:

$$I^R = I^D - \gamma B * I^C \tag{5.18}$$

---

[8] since $T(l,m)$ is real, $\mathcal{V}(u,v)$ is Hermitian and $\mathcal{V}(-u,-v) = \mathcal{V}^*(u,v)$. It means getting two visibilities for each (u,v) measurement.

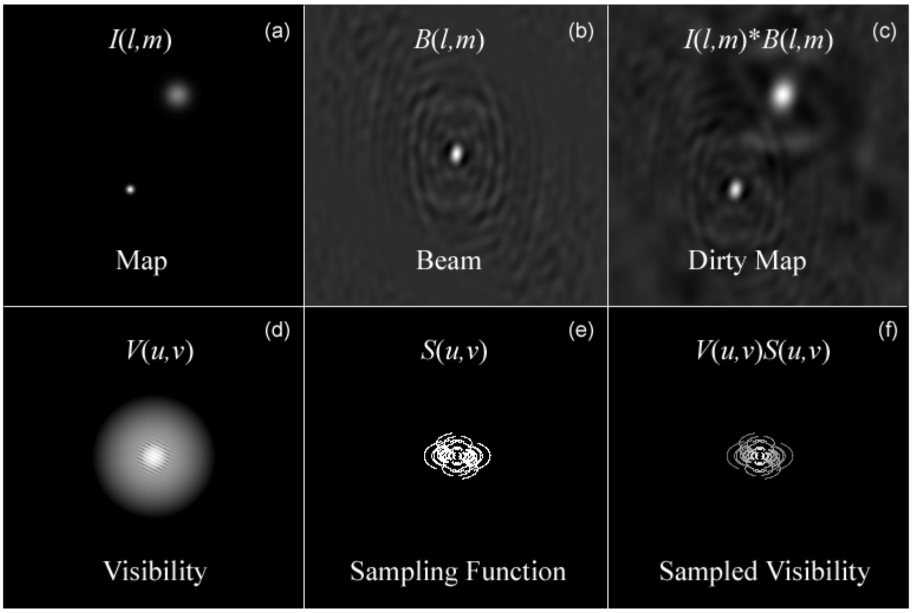

Fig. 5.9: Schematic summary of different quantities related to imaging process. The bottom row lies in the *visibilities domain*: (f) box illustrates the Sampled visibility data. Once corrected and calibrated, these data are the starting point of cleaning technique. The top row instead lies on the *image domain*: the process of deconvolution starts from the dirty map, (g) box.

that becomes the new reference image.

At each cycle, the residual image is updated and a new peak is found. The stopping criteria are set by the number of clean components found, a theoretical rms to be reached, a given flux value to clean etc. The last residual image is the *Noise Image*, where typically no more structure should be present.

Finally, during *Restoration*, in order to recover the true sky surface brightness, the noise map is added to the clean map I^C, convoluted with the *clean beam* B^I, i.e. a Gaussian beam whose size matches the synthesized beam size:

$$I = I^C * B^I + I^R \tag{5.19}$$

Note that, since Högbom's CLEAN uses only delta functions, it is most appropriate for fields of isolated point sources.

5.3.2 WSClean Imager

WSClean ("w-Stacking Clean") is a command-line imager that is tailored for wide-field imaging (Offringa et al. 2014). It supports several deconvolution methods, including multi-scale and multi-frequency deconvolution.

The w-term

For wide-field imaging, sky curvature and non-coplanar baselines result in a non-zero w-term (Mevius et al. 1999). Standard 2D imaging applied to such data would produce artifacts around sources away from the phase center. The image degradation effects of the w-term is a significant issue for low-frequency telescopes, such as LOFAR, that by nature are wide-field instruments. Thus, the imaging algorithm needs to account for the "w-term" during inversion.

There are several methods to deal with the w-term during imaging, WSClean uses the w-stacking technique. The w-stacking method grids visibilities on different smaller layers with $w = cost$ and performs the w-corrections after the inverse 2D FT. In fact, eq. 5.9 can be separated in a part depending on w-term and another only on (l, m):

$$\mathcal{V}(u, v, w) = \int\int \frac{I(l, m)\, e^{-2\pi i w(\sqrt{1-l^2-m^2}-1)}}{\sqrt{1-l^2-m^2}} \times e^{-i2\pi(ul+vm)} dl\, dm \tag{5.20}$$

So, for small FoV, equation 5.20 is an ordinary two-dimensional Fourier transform going from (u, v) space to (l, m) space, and can be firstly inverted to get

$$\frac{I(l, m)}{\sqrt{1-l^2-m^2}} = e^{2\pi i w(\sqrt{1-l^2-m^2}-1)} \int\int \mathcal{V}(u, v, w) \times e^{i2\pi(ul+vm)}\, dudv \tag{5.21}$$

and finally the phase shift $e^{2\pi i w(\sqrt{1-l^2-m^2}-1)}$ can be applied.

Summarizing, the whole FoV is divided in area with constant w-term, the upon procedure is applied to every w-layer, and all the w-projection terms are finally multiplied (integrated) in the image plane, to reconstruct the sky function. Fig. 5.10 shows the resulting image after cleaning with (right) or without (left) the w-correction. It is evident the improvement, in particular for bright sources far from the center of the FoV, phase differences strongly afflicts the quality of the image if the w-term is not taken into account 5.10a.

Description of the cleaning algorithm

The image reconstruction framework is based on Cotton-Schwab major/minor cycles (referenza Schwab and Cotton 1983). During minor cycles, the algorithm operates largely in the image domain starting with a PSF and a residual image. The output is an incremental model image. As in the Clarks algorithm (referenza 1980), during minor cycle iterations a small patch of the PSF is used, instead of the full pattern. This is an approximation that will result in a speed-up in the minor cycle, but could introduce errors in the image model if there are bright sources spread over a wide field-of-view where the flux estimate at a given location is affected by sidelobes from far-out sources. To minimize this error, the iterations are stopped when the brightest peak in the residual image is

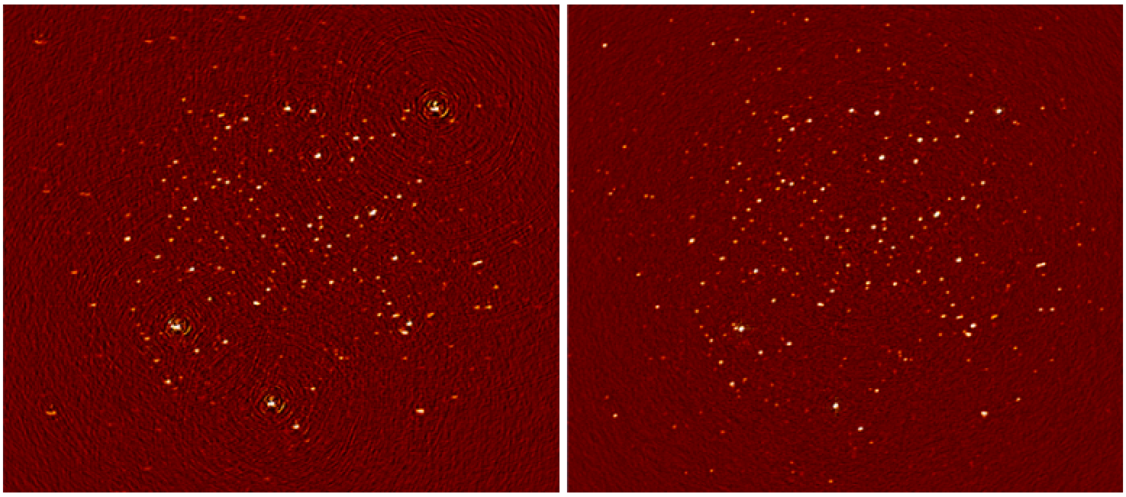
(a) (b)

Fig. 5.10: Difference of the cleaning procedure, correcting the w-terms (right) and without correcting the w-terms (left). Note in particular the improvement for bright point sources in the bottom left corner of panel (a) that due w-term appear degradated and diffused, while in panel (b) are defined and point-like.

below the first sidelobe level of the brightest source in the initial residual image.

Then, during the next major cycle, which operates mainly in the visibility domain, the contribution of the previously composed model image is subtracted out from the original visibilities, and the residual visibilities are regridded and Fourier-transformed to produce a new residual image.

This approach allows for a practical trade-off between the efficiency of operating in the image domain and the accuracy that comes from returning to the ungridded list of visibilities after every 'step' (minor cycle).

Weighting scheme

To pass from the visibility to the image domain, the speed of the algorithm is improved by using a Fast Fourier Transform (FFT), that requires data on a regularly spaced grid. Aperture synthesis does not provide $S(u,v)\mathcal{V}(u,v)$ on a regularly spaced grid and thus, data are gridded into the 2-d array before FFT. Since (u,v) points are not uniformly distributed on the u-v plane, there will be cells of the grid more populated then others.

It is then possible to weight the visibilities in different ways. The weight given to each visibility sample can be adjusted to fit the desired output. As a matter of fact, the weighting function multiplies the sampling function

$$S(u,v) \to S(u,v)\,W(u,v) \tag{5.22}$$

altering also the PSF of the instrument. The most used weight are 'natural', 'uniform', 'Briggs' (Briggs 1995), but also on top of the weighting scheme, an UV-taper can be applied to further adjust the weight calculations.

- Uniform weighting scheme
  Uniform weighting will give each scale the same weight, independently on how many visibilities fall in one u-v cell. In this weighting mode, the resulting PSF has the narrowest possible main lobe (i.e. highest possible angular resolution) and suppressed sidelobes across the entire image, but the peak sensitivity is significantly worse than optimal.

- Natural weighting scheme
  The natural weighting scheme gives equal weight to all samples. Since lower spatial frequencies are usually sampled more often than the higher ones, the inner uv-plane will have a significantly higher density of samples and hence higher signal-to-noise than the outer uv-plane. In this case, $W(u, v) = 1/\sigma^2$ in occupied cells, where σ^2 is the noise variance. Generally it gives more weight to short baselines, so the angular resolution is degraded, but it maximizes point source sensitivity.

- Briggs weighting scheme
  Briggs or Robust weighting creates a PSF that smoothly varies between natural and uniform weighting, based on the signal-to-noise ratio of the measurements and a tunable parameter, called the robustness parameter R. The scaling of R is such that R=0 gives a good trade-off between resolution and sensitivity, varying between -2.0 (close to uniform weighting) to 2.0 (close to natural).

In addition to the weighting scheme specified via the 'weighting' parameter, a taper can be used to shape the synthesized beam. A Gaussian taper multiplies the uv-weights with a Gaussian function (which therefore makes the synthesized beam approach a Gaussian function), to weight down high spatial-frequency measurements. The effect of uv-taper is that the clean beam becomes larger, and surface brightness sensitivity increases for extended emission.

Multi-scale (MS) cleaning

Multi-Scale CLEAN (Cornwell 2008) is a scale-sensitive deconvolution algorithm designed for images with complicated spatial structure. It starts from the dirty image and parameterizes it into a collection of inverted tapered paraboloids, at different scales, i.e., convolves it with scales of different size and selects the scale with the highest peak. Then, it enters in a sub-minor loop where finds the peak for that specific scale-convolved image, convolves with scale-psf and subtracts, as classical cleaning procedure. This is done for each input scale. A pictorial representation of how a source with structure at multiple spatial scales is modeled in Multi-Scale CLEAN is illustrated in Fig. 5.12. The top left and bottom left images show flux components of two different scale sizes. The

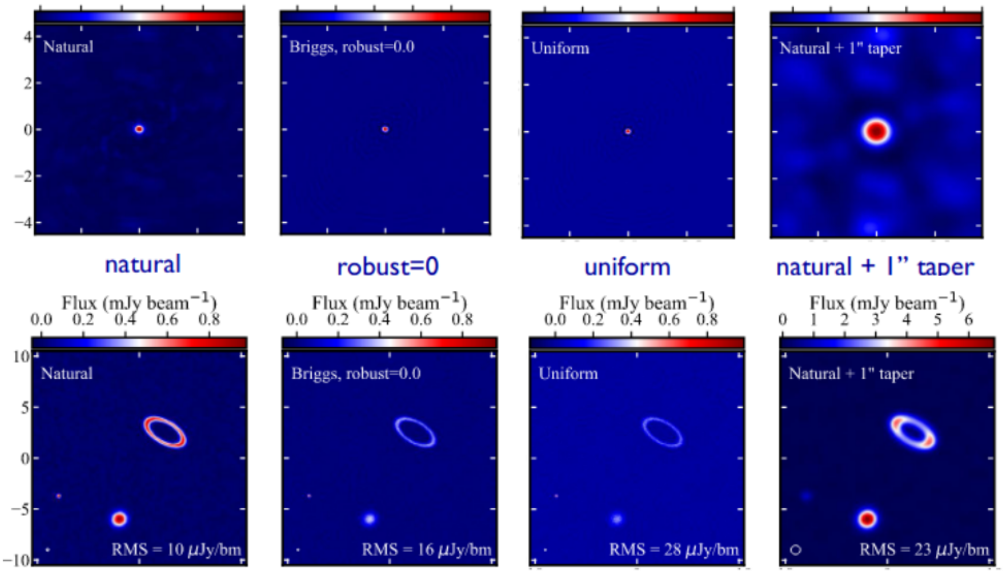

Fig. 5.11: Differences between the various weight in terms of PSF and resulting images. From natural to uniform the PSF becomes smaller, but the rms increases. Last columns shows the result of applying additional taper to an already degraded natural resolution.

images in the middle column show sets of delta functions that mark the locations and amplitudes of the flux components for each scale. The image on the far right, the final model, is the sum of the convolutions of the first two columns of images.

Multi-frequency (MF) cleaning

When working with large bandwidth, it could happen that the approximation of constant spectrum sources falls and the spectral variation need to be taken into account during deconvolution. So, the flux (and thus the fraction of it to be subtracted) is different across the observational bandwidth. To account for that, multi-frequency algorithms have been implemented. Wsclean approach is to use the full bandwidth to determine the location of clean components, which decreases the chance of selecting noise peaks or sidelobes. Then, the full-bandwidth is divided into several channels - determined by the user[9] - and the spectral variation of each clean component is determined by measuring the flux in the individual channel images at the location of the peak. Separated model images and PSF are constructed for each output channel, and the subtraction occurs at each channels. The stopping thresholds are relative to the integrated image, and the output image is created in the middle of the sampled frequency range.

Here the main parameter used to perform the cleaning with WSClean are listed

- `minuv-l` and `maxuv-l`: set the minimum and maximum uv values (in wavelengths) that are gridded and used to obtain the final image.

---

[9] For our analysis, the multi-frequency clean is performed by dividing the full-band in 6 channels

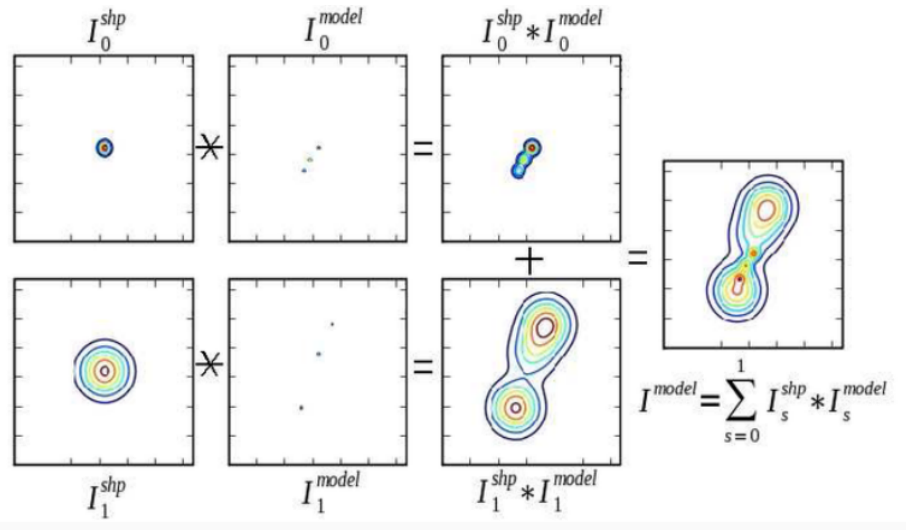

Fig. 5.12: The figure illustrates how a source with multi-scale features can be represented by two scale sizes. *Left:* flux components of two different scale sizes. *Middle:* sets of delta functions that mark the locations and amplitudes of the flux components for each scale. *Far right:* the model is the sum of the convolutions of the first two columns.

- `scale`: the pixel size is decided based on the Nyquist sampling theorem, which states that the pixel dimension Δx must be at least half of the beam, in order to perform a good sample of the signal and reconstruct reasonable part of the information.

$$\Delta x < \frac{1}{2}\frac{\lambda}{b_{max}} \tag{5.23}$$

- `mask`: a mask is used to speed-up the cleaning process, specifying to search for components only in certain regions of the image: all zero values are interpreted as being not masked, and all non-zero values are interpreted as masked, so that WSClean can be forced to to find components only in a certain area. Masks during this analysis are created with PyBDSF software[10], and in some cases manually edited to add eventually undetected areas by the software itself. Using a mask allows the clean to perform better, since it searches component in specific areas, instead of the whole FoV.

- `threshold`: defines where to stop cleaning. WSClean will continue cleaning until the peak residual flux is below the given threshold. It is good practice to make sure cleaning has reached the threshold, and only use the number of clean components found `niter` to make sure WSClean will not run for an excessively long time. Unless otherwise stated, the stopping criteria used in this work is noise-based, by setting the threshold parameter equal to theoretical[11] rms noise, always

---

[10] PyBDSF (the Python Blob Detector and Source Finder) is a tool designed to decompose radio interferometry images into sources and make available their properties for further use.

[11] LOFAR Image noise calculator

combined with a mask to avoid to over-clean.

- `weight`: defines the weighting scheme, uniform, natural or Briggs, where in the latter case also the robust parameter needs to be specified. A good choice when handling with LOFAR data is a Briggs weighting and so, this is the scheme used for all the analysis.
- `multiscale`: sets the scales (in pixels) where peaks are searched for in the multi-scale clean.
- `taper`: tapering used to shape the synthesized beam. The two options are Gaussian or Tukey taper. As mentioned before, this improves the sensitivity of the diffuse emission imaging process and reduces the resolution of the image.

5.4 Results

5.4.1 Source subtraction

In order to study the large scale emission of A1413, imaging at high and low spatial resolution is needed. First, we subtracted the point-sources that overlap and contaminate the extended radio emission using high resolution images. Then, we imaged the subtracted visibilities at low resolution to recover the extended emission.

In general, for data from the LOFAR survey, a good choice is to apply a Briggs weighting scheme with a negative robust parameter R, as it allows to down-weight the secondary lobes. Moreover, the standard inner u-v cut, which sets range of baselines to be gridded (see eq. 5.14), is fixed at $\mathrm{b_{min}} > 80\lambda$ to avoid interference on short baseline (i.e. more extended angular scales on the sky). This cut correponds to an angular scale of $\sim$1 deg.

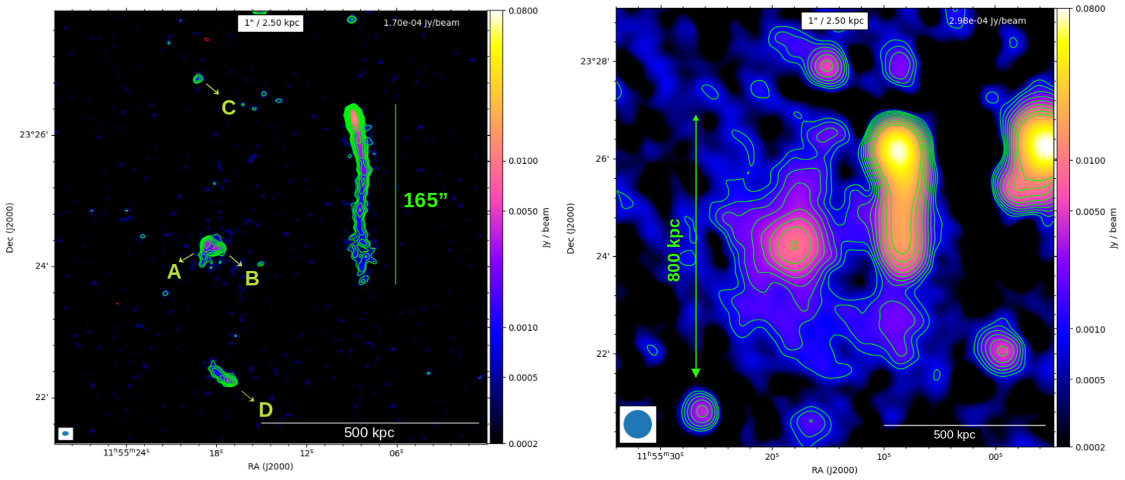

Fig. 5.13: *Left panel:* High resolution 144MHz image with beam $4'' \times 6''$ (shown in the bottom left corner). The contour levels start at 3σ, where $\sigma = 170\,\mu\mathrm{Jy/beam}$, and are spaced with a factor of $\sqrt{2}$. The -3σ contours are red coloured. The two point sources, that are going to be subtracted are labeled with letters: two central AGN A, B; one point-like north source C and one slightly extended south source D. As a reference, the rough extension of the AGN tail on the right is displayed. *Right panel:* Low resolution 144MHz image with beam $35'' \times 35''$ (shown in the bottom left corner). The contour levels start at 3σ, where $\sigma = 298\,\mu\mathrm{Jy/beam}$, and are spaced with a factor of $\sqrt{2}$. The -3σ contours are red coloured. In this case, as a reference, the rough extension of the halo emission is displayed.

First, a high resolution image with $R = -1$ was obtained to inspect the data (Fig. 5.13, left). In this image, different sources, named with letters (A, B, C, D), are visible within a radius of 500 Kpc ($\sim 0.5 R_{500}$) from the cluster centre: the emission from these sources contaminates the diffuse emission that we want to study, and thus, must be subtracted. The AGN tailed galaxy on the right, with optical counter part at z = 0.144, is instead quite extended and difficult to remove, i.e. disentangle from the diffuse radio emission, and moreover could play a role in the emission mechanism, as discussed below. Therefore, we decided to not subtract it.

A usual way to subtract the compact sources is to identify the corresponding clean component in the model image and subtract them directly from the visibilities. Few steps are needed:

- First imaging all the original data visibilities (column DATA of the .MS file[12]) and identify, in the output model, the components of the compact source to be subtracted;

- compute the visibilities corresponding to the selected clean components. This is done by performing at anti-Fourier transform of the selected model components (`-predict` step in Wsclean) which fills the MODEL_DATA column with the visibilities

- perform the subtraction and create a new data column SUBTRACTED_DATA = DATA - MODEL_DATA

Three steps of subtraction have been performed (Fig. 5.14). The initial image (Fig. 5.14 (*top row, left*)) was made with $\mathrm{R} = -2$ to obtain a high angular resolution (FWHM $3.9'' \times 2.9''$) that allows to select the emission from the discrete sources only. The resulting clean component are shown in Fig. 5.14 *(top row, right)*. Since the sources are extended, we checked that their emission was fully subtracted making an image with a slightly different robust ($\mathrm{R} = -1.5$). This image, (Fig. 5.14 *(middle row, left)*) shows that residual emission, particularly from sources A,B and D, is still present. Hence, we subtracted emission corresponding to component in the regions on Fig. 5.14 *(middle row, right)*.

Finally, the subtracted data set was imaged at lower resolution ($12.10'' \times 7.10''$): A, B, and C compact sources, appear to be well subtracted from the uv-data ((Fig. 5.14 *(bottom row, left)*)). Because of its extended emission, residuals from D source, at the South of the cluster, are still present. Therefore, we proceeded as explained above, this time making an image with an inner UV-cut able to exclude the emission more extended then 300". This is a good way to be sure to select and subtract an extended source, without considering also the diffuse emission we want to study after.

---

[12] LOFAR Measurement Set (MS) is structured as a set of tables, where the Main Table contains the visibility data, flags, UV weights, etc; and the Subtables contain meta data, such as information about antennas, field, spectral windows etc.

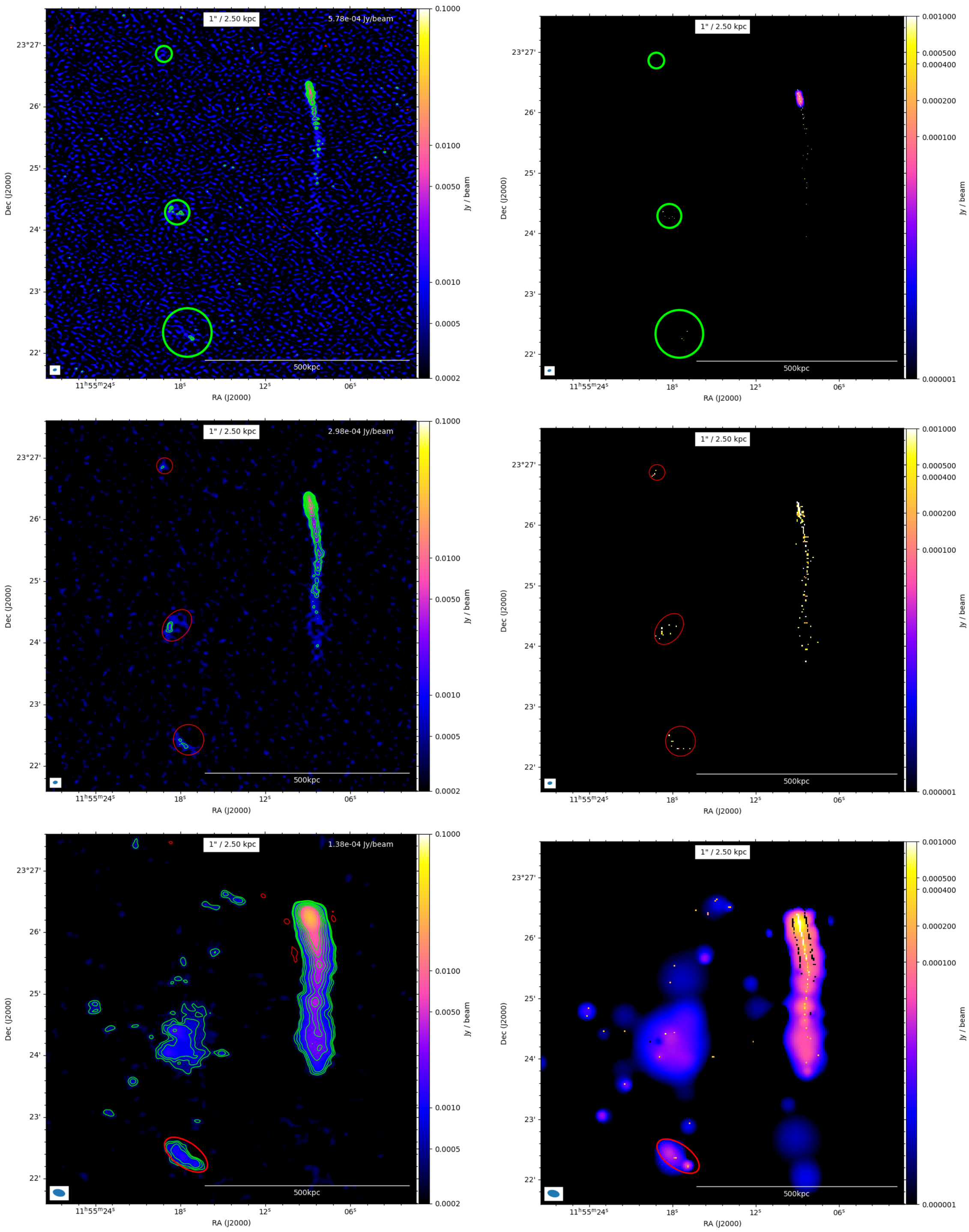

Fig. 5.14: Images (left columns) and models (right columns) used for the point sources subtraction. Selected and subtracted components are displayed with circular regions. *Top row:* First subtraction step. This very high resolution image (beam $3.90'' \times 2.60''$) was obtained with weighting Briggs $\mathrm{R} = -2$ and multi-scale (0,2,4,8,16 pixels scales). *Middle row:* Second subtraction step to clean better, in particular A and B central sources. Very high resolution image (beam $4.70'' \times 3.30''$). To obtain this resolution, weighting Briggs $\mathrm{R} = -1.5$ and multi-scale with small 0,2,4 pixels scales was used. *Bottom row:* Third subtraction step to definitively remove the slightly extended source D. The image has a resolution of $12.10'' \times 7.10''$ and was obtained using a less negative robust parameter $\mathrm{R} = -0.25$ but with a u-v cut to exclude the emission on scale larger than 300", i.e. $\sim 750\,\mathrm{kpc}$.

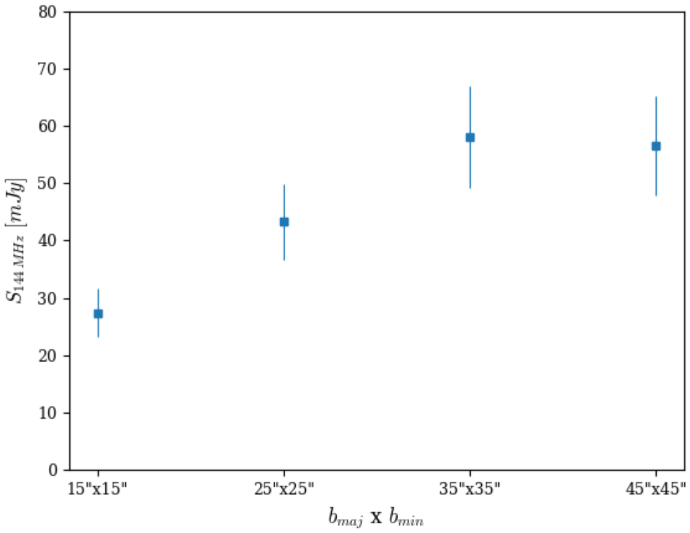

Fig. 5.15: Flux within 3σ contour level without the AGN tail contribute for all the low-resolution images of Fig. CA.1.

Eventually, the final uv-subtracted dataset is imaged including all standard baselines ($> 80\lambda$), maintaining a negative Briggs weighting with $\mathrm{R} = -0.25$ and tapering down the baselines longer than $\sim 20, 13, 10, 6\,\mathrm{k}\lambda$ (i.e. using a gaussian taper with a FWHM of 10, 15, 20, 30 arcseconds, respectively) to gain sensitivity towards the diffuse emission (see Fig. A.1).
Indeed, the goal is to study the extended radio emission, maximising the sensitivity to low surface brightness extended emission of the cluster, without degrading too much the resolution (i.e., preserving the maximum resolution possible). As shown in Fig. 5.15, as the beam size increases, it collects more and more flux of the diffuse emission, until it starts decreasing, because the extended halo emission is spread on a larger area. The image that collects the higher flux sets the optimal resolution to study the extended emission. In this case the highest sensitivity is achieved with FWHM of 35"×35" (Fig. 5.13, right).

As shown in Fig. 5.13, there is a clear evidence of a wider low brightness emission, never detected before: a quite unusual radio source for a cool core cluster. The question that arises is whether it can be considered as a single giant radio halo, or we are facing a hybrid two component emission, as in the case of RXJ1720.1+2638 (Savini et al. 2019) or of PSZ1G139.6124.20 (Savini et al. 2018). Also, the influence of the AGN tail, apparently mixed with the extended emission, must be taken into account and excluded from the flux calculation[13]. The 3σ flux of entire diffuse emission (without the AGN tail) is equal to $58.08 \pm 8.85\,\mathrm{mJy}$, which means $\mathrm{P}_{144\mathrm{MHz}} = (3.0 \pm 0.5)\,10^{24}\,\mathrm{W/Hz}$. The halo

---

[13] The flux density errors ΔS is estimated as $\Delta S = \sqrt{(\sigma_{cal} \cdot S)^2 + N_{beam} \cdot rms^2}$, where $N_{beam} = N_{pixel}/beam\,area$ is the number of beams in the source area, and σ_{cal} indicates the systematic calibration error on the flux density, with typical value 15% for LOFAR HBA observations (Shimwell et al. 2019). Error calculation Δ_S is applied on all flux measurements hereafter.

emission extends to about $800\,\mathrm{kpc} \sim 320''$ (N-S direction) and $500\,\mathrm{kpc} \sim 200''$ (E-W direction, excluding the AGN tailed galaxy).

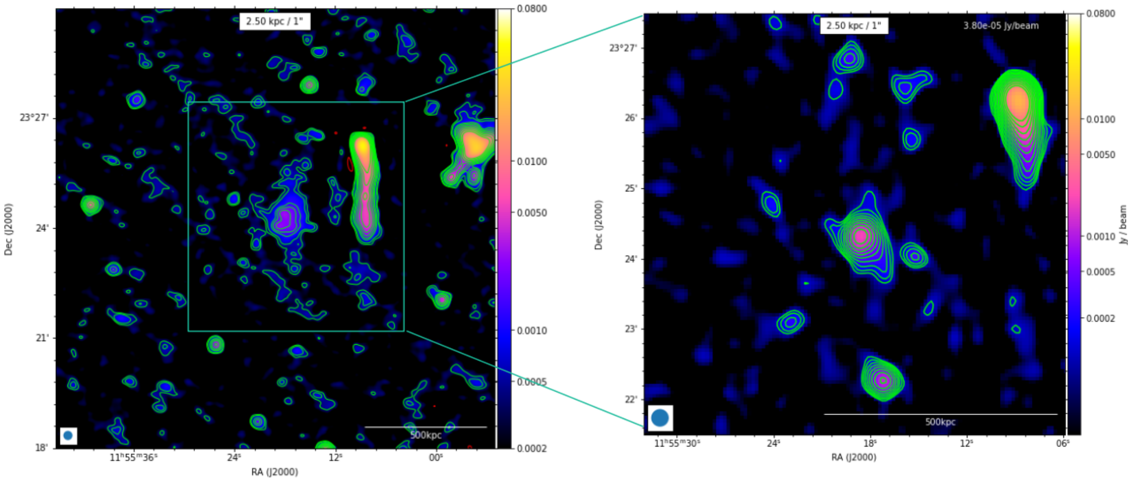

Fig. 5.16: *Left panel:* Medium resolution ($15'' \times 15''$) 144MHz image of A1413. the contour levels star at 2σ, where $\sigma = 203\,\mu\mathrm{Jy/beam}$ and are spaced with a factor of $\sqrt{2}$. *Right panel:* Image of A1413 from Govoni et al. 2009 at 1.4 GHz with a FWHM of $15'' \times 15''$. The first contour level is drawn at 0.1 mJy/beam and the rest are spaced by a factor $\sqrt{2}$. The sensitivity (1σ) is 0.035 mJy/beam. Red circles on both images, illustrate the region of $\mathrm{r} \sim 0.7'$ extracted to determine the MH spectra index $\alpha_{144}^{1400} = 1.11 \pm 0.17$.

5.4.2 Comparison with high frequency data

Govoni et al. 2009 have studied the emission of A1413 using 1.4 GHz VLA data. Here, we complement our LOFAR image with the one presented by Govoni et al. 2009 to derive information about the source spectral properties of the previously classified mini-halo central emission. The radio MH emission detected by Govoni et al. 2009, is about 1.5' ($\simeq$ 220 kpc) in size, and has a flux of $\mathrm{S_{MH,1.4GHz}} = 1.9 \pm 0.7\,\mathrm{mJy}$, which corresponds to a power of $\mathrm{P_{MH,1.4GHz}} = 1.0 \cdot 10^{23}\,\mathrm{W/Hz}$ (see Tab. 5.1).

Note that, in the VLA analysis, just the flux of one faint unresolved radio sources (the A source in our analysis), detected in the FIRST survey (see Fig. 3.2a), was taken into account. Thus, the flux density of MH diffuse emission reported above, estimated via subtraction of the FIRST source (flux density of $2.9 \pm 0.7\,\mathrm{mJy}$) from the total VLA emission in the cluster center (flux density of $4.8 \pm 0.2\,\mathrm{mJy}$), can be considered as an upper limit.

To estimate the spectral index of the MH emission, we have re-imaged the LOFAR data (Fig. 5.16, left) at the same $15'' \times 15''$ resolution as the VLA image (Fig. 5.16, right). The size of the considered region is taken from literature ($\mathrm{r} \sim 0.7'$ Govoni et al. 2009),

A1413	ν MHz	$S_{3\sigma}$ mJy	$P_{3\sigma}$ 10^{23} W/Hz	D kpc
Halo	144	36.70 ± 5.70	18.70 ± 2.90	$(D_{max}, D_{min}) = (800, 500)$
Mini-Halo	144	23.90 ± 3.70	12.20 ± 1.90	220
Mini-Halo	1440	1.90 ± 0.70	1.01 ± 0.10	220

Tab. 5.1: Summary of the main properties of the two radio emission in A1413. From the spectral analysis we obtained $\alpha_{MH} = 1.11 \pm 0.17$ while $\alpha_{Halo} > 1.6$ at 1σ.

with the total flux density of $\mathrm{S_{MH,144MHz}} = 23.9 \pm 3.7\,\mathrm{mJy}$ (Tab. 5.1). The spectral index is estimated as $\alpha_{MH} = 1.11 \pm 0.17$. Note that the spectral index might be steeper, considering that the flux reported by Govoni et al. 2009 is overestimated, as explained above.

As the extended halo emission is not detected in the VLA image, we can put a lower limit to its average spectral index, comparing the mean halo brightness at 144MHz with the rms noise of VLA image. In this case, the central $\mathrm{r} < 0.7'$ MH was masked to derive flux coming from the giant halo only $\mathrm{S_{Halo\,144MHz}} = 36.70 \pm 5.70\,\mathrm{mJy}$, corresponding to $\mathrm{P_{Halo\,144MHz}} = (1.87 \pm 0.29)\,10^{24}\,\mathrm{W/Hz}$ (Tab. 5.1). We derive that the halo external emission must have a spectral index steeper than $\alpha_{Halo} > 1.6$ at 1σ. The different spectral index of the two regions may suggest the presence of two different kind of radio emission co-existing in the same cluster. Further investigation is performed in Chapter 6, when also X-ray properties are considered.

5.4.3 Halo emission analysis

LOFAR 35" resolution image image was re-analized using HALO-FDCA (Boxelaar et al. 2021) fitting procedure[14] to obtain a more reliable and noise independent value of its extension and flux: from this analysis the e-folding radius $\mathrm{r_e} \sim 190\,\mathrm{kpc}$ and a flux of $93.33 \pm 12.34\,mJy$ inside $3r_e$ (integration radius set inside the program). HALO-FDCA code allows the user to choose the type of the model with which the data are fitted: circular, elliptical and skewed (which is an extended version of exponential profile of eq. 2.27). In this case, the central MH was masked to derive flux coming from the giant halo (see Fig. 5.17). We performed the fit using LOFAR iamge with FWHM $35'' \times 35''$, and selected the fit with best χ^2_{red} and lower AIC estimator. The result of the best-fit are listed in Tab. 5.2.

The position of A1413 radio halo in the $\mathrm{P_{144}} - \mathrm{M_{500}}$ relation is shown in Fig. 5.18.

---

[14] Halo-FDCA (Flux Density CAlculator) is able to perform flux density (and power) estimations of radio halos in galaxy clusters, using Bayesian Inference.

Cluster	S_ν mJy	P 10^{24} W/Hz	I_0 μJy arcsec^{-2}	r_{max} kpc	χ^2_{red}	AIC
A1413 (LOFAR)	93.33 ± 12.34	5.26 ± 0.69	$3.13^{0.36}_{0.30}$	$275.29^{36.63}_{34.44}$	0.99	-3 272

Tab. 5.2: Main results of the HALO-FDCA fitting procedure of the halo 35" resolution LOFAR image with central MH excluded modeled with a skewed model. Col 2: halo flux densities at $\nu = 144\,MHz$ integrated at $3r_e$; Col 3: corresponding power; Col 4: output central surface brightness parameter; Col 5: maximum e-folding radius of the model to indicate the halos estimated size (the skewed model for instance has four r parameters). Uncertainties on presented values are taken from MCMC walker distributions. Col 6: reduced χ squared value; Col 7: The Akaike information criterion (AIC) estimator for model selection.

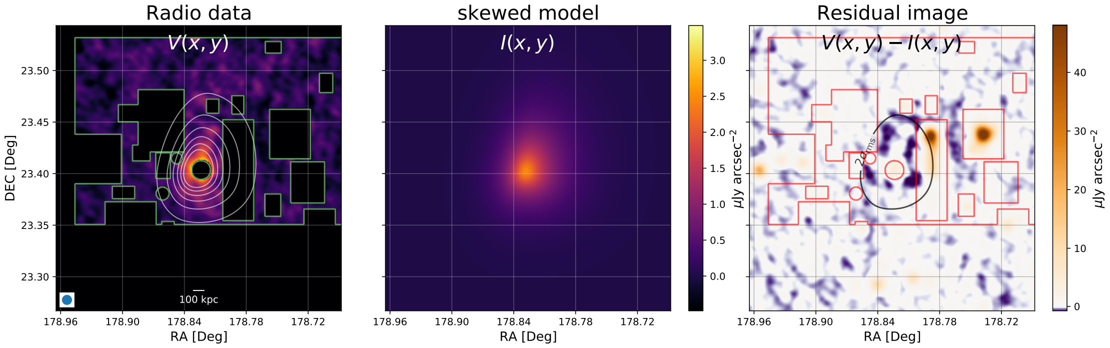

Fig. 5.17: Fitting result for A1413 at 144 MHz. *Left panel:* LOFAR 35" resolution image, with beam depicted on the bottom. The contours show the model at [1, 2, ..., 7]σ_{rms} levels. Contaminated regions are masked out and contoured in green. *Middle panel*: Model skewed map. *Right panel:* residual image. The contour shows the $2\sigma_{rms}$ level of the model. The red contour now shows the masked regions, but this time the contamination is visible. Fitting parameter results are listed in Tab. 5.2

The two coloured points indicate the discrepancy between $\mathrm{P}_{144\,\mathrm{Halo}}$ calculated wihtin 3σ contour and the one estimated from Halo-FDCA fit. This difference comes from the fact that the 3σ flux of the radio halo $\mathrm{S}_{\mathrm{Halo}\,144\mathrm{MHz}} = 36.70 \pm 5.70\,\mathrm{mJy}$ is clearly underestimated, because to calculate it, we subtracted the contribution from the AGN tail and the central MH region. On the other hand, Halo-FDCA fills these region by interpolanting the masked region (see Fig. 5.17) and also, integrates the flux down to $3r_e$, that correponds to 80% of the total flux. Both points, however, follow the general behaviour (the sample contains value taken from literature and clusters newly analyzed with Halo-FDCA by vanWeeren et al. 2020). In particular $\mathrm{P}_{\mathrm{Halo-FDCA}} = (5.26 \pm 0.69)\,10^{24}\,\mathrm{W/Hz}$ is consistent with the best fit line.

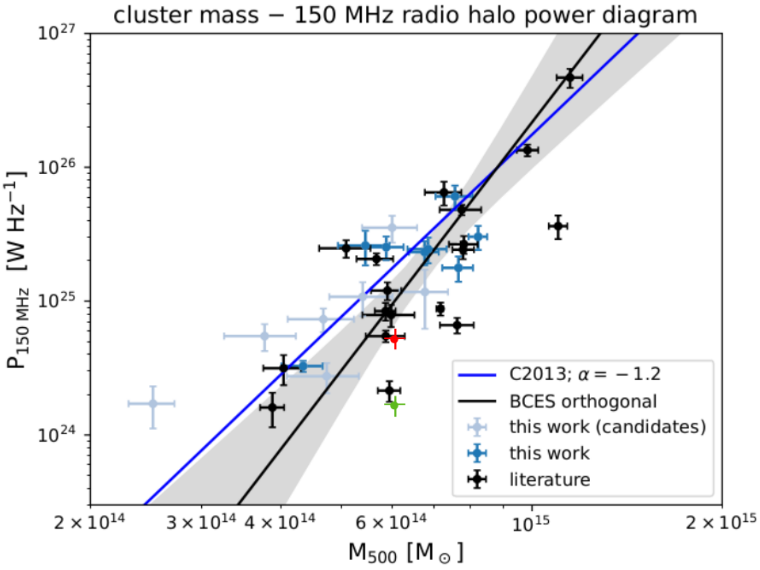

Fig. 5.18: Position of A1413 halo emission in the $\mathrm{P}_{144} - \mathrm{M}_{500}$ plane. The two points correspond to power estimated by the Halo-FDCA (red point) with $3r_e$ and to power within 3σ contour (green point). Credits: adapted from Fig. 2.8 (vanWeeren et al. 2020).

Discussion

Theoretical models predict that giant radio halos originate during merger events, when relativistic CRe in the ICM can be re-accelerated by turbulence (Sec. 2.1). In this scenario, the properties of the radio halos should be connected with the mass and merging history of the host cluster. However, the details of the re-acceleration mechanisms are not understood yet. Important information about the distribution of CRe and magnetic field with respect to the thermal gas may be derived from the comparison between radio and X-ray observations. Indeed, it has been found that the radio emission from giant halos roughly follows the distribution of the thermal gas (e.g., vanWeeren et al. 2019).

Since many years, quantitative studies to investigate the point-to-point correlation between the radio and X-ray brightness distribution of giant halos have been attempted (Govoni et al. 2001, Feretti et al. 2001, Giacintucci et al. 2005). However, most of them were limited by the resolution and sensitivity of the radio and X-ray observations. Now, thanks to deep and sensitive observations, these studies can be carried out in more detail (Rajpurohit et al. 2021).

To determine the local values of the radio and X-ray brightness, radio and X-ray images have been subdivided into rectangular grids and for each point of the grid, the mean radio and X-ray surface brightness have been calculated. Note that, since this approach involves spatial averaging, this kind of analysis is insensitive to features on scales smaller than the cell size, but it allows to identify local variation of X-ray and radio brightness that would be averaged out when computing classical azimuthal profiles.

Data are then fitted with a generic power-law relation of the type

$$\log(I_R) = A\,\log(I_X) + B \tag{6.1}$$

where the slope of the scaling A determines whether the radio brightness (i.e. the magnetic field strength and CRe density) declines faster ($A > 1$) than the X-ray brightness (i.e. the thermal gas density), or vice versa ($A < 1$). In general, in the literature, a positive correlation has been found with *linear* or *sub-linear* scaling for the few giant radio halos that have been analysed with this method. However, there are also some exceptions: for examples, no clear correlation has been found in the Bullet cluster (Shimwell et al. 2014). The connection between thermal and non-thermal plasma could reflect the particle re-acceleration mechanism, and it could be used to discriminate between models of halo formation (Govoni et al. 2001).

Recently, Ignesti et al. 2020 have extended the work carried out for giant radio halos to a sample of mini halos. Contrary to what is generally reported in the literature for giant radio halos, they found that mini-halos have *super-linear* scaling between radio and X-rays (i.e. $A > 1$, see eq. 6.1). This suggests that the distribution of relativistic electrons and magnetic field is steeper than the gas distribution, and more peaked towards the cluster centre. The difference between the radio-X ray correlation for mini halos and giant halos could also suggest an intrinsic difference in the nature of these radio sources.

6.1 Origin of the halo emission

The X-ray emission from A1413 shows an elliptical morphology, elongated in the S-N direction, which is also clearly visible in its radio emission (see Fig. 6.1). Thus, we can conclude that the ellipticity is a common feature of this cluster in both radio, X-ray, and optical analysis (see Fig. 3.1, Chapter 3).

In order to understand the radio emission discovered in A1413, we performed a composite X-ray and radio study by using the radio images at 144 MHz presented in Fig. 5.13 (left) and the XMM-Newton images and maps presented in Fig. 4.8 and 4.16.

Following Govoni et al. 2001, a grid covering the cluster region has been constructed and for each box the mean radio and X-ray quantities, as well as the root-mean-square (rms), which can be assumed as an estimate of the statistical error, has been calculated. The size of the boxes $35'' \times 35''$, has been chosen to be equal to the area of the beam. This grid resolution allow also to be minimally affected by the PSF of XMM-Newton, which for MOS and pn is $\sim 5'' - 6''$ (FWHM).

The area to consider for this fit was chosen based on lowest X-ray brightness level, that includes the halo radio emission and excludes other external radio sources (see Fig. 6.2), in order to select an homogeneous and not radio-biased area. Both point-like and extended (the AGN tailed galaxy) contaminating sources in the radio image were identified and cells containing them, removed.

Presumably, the AGN tailed galaxy also influences some contiguous regions. Thus, a safe choice is to exclude these regions too. To determine them, we simply identify points that appears to be an extension/continuation to the well defined tail emission (red points of Fig. 6.3a). Fig. 6.2 shows the grid overlapped on both the X-ray and the radio image.

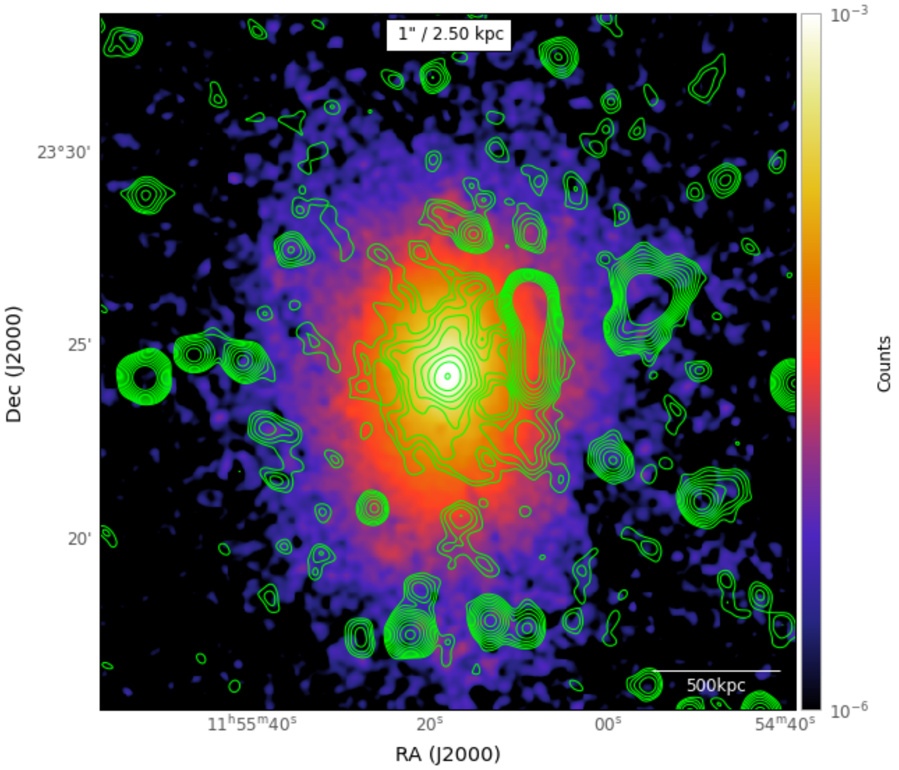

Fig. 6.1: LOFAR 144MHz contours of the radio emission from A1413, superimposed on XMM-Newton [0.7-2]keV band image. The contour levels star at 2σ, where $\sigma = 298\,\mu\mathrm{Jy/beam}$ and are spaced with a factor of $\sqrt{2}$.

The red and magenta boxes of Fig. 6.2 indicate the excluded regions. We note that also 4 magenta central boxes corresponding to the mini-halo are not taken into account.

We used the `LinMix` package (Kelly et al. 2007) to search for a X-ray and radio correlation and determine the best-fit parameter to the observed data. `LinMix` uses a Bayesian approach, and allows one to consider measurement uncertainties on both quantities. It can also handle non-detections (i.e. upper or lower limits) on the y-variable. The threshold for upper-limits is fixed at 2σ in the radio image following Botteon et al. 2020[1]. The correlation strength is measured by the Pearson correlation coefficient[2] r_p. Tab. 6.1 summarizes the slope and correlation coefficient of the $I_R - I_X$ trend shown in Fig. 6.3b. The two surface brightnesses are positively correlated $r_p = 0.82$ and have a sub-linear scaling $A = 0.63^{+0.07}_{-0.06}$, in agreement with other literature works (e.g., Botteon et al. 2020,

---

[1] In the past, the correlation was performed only considering data points above 3σ. Botteon et al. 2020 noted that the introduction of a threshold combined with a large intrinsic scatter can introduce a bias in the correlation and it has been demonstrated that threshold of 2σ is the best choice Botteon et al. 2020.

[2] Pearson correlation coefficient is a measure of linear correlation between two sets of data. Two variables that are positively $r_p > 0$ or negatively $r_p < 0$ correlated, can have different grades of correlation:

- $0 < |r_p| < 0.3$ weak correlation;
- $0.3 < |r_p| < 0.7$ moderate correlation;
- $0.7 < |r_p| < 1$ strong correlation

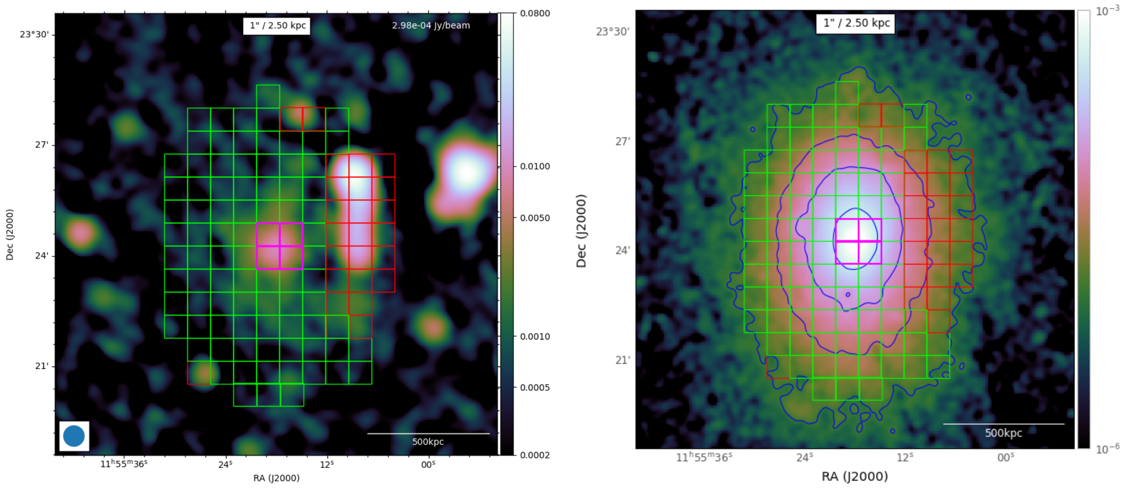

(a)

(b)

Fig. 6.2: LOFAR 144MHz image (a) and XMM [0.7-2]keV image (b) of A1413 with grid overlapped. Boxes are 35"x35" size. Final grid, used for correlation, is composed by green boxes; red boxes are excluded from the correlation since contaminated from point-like sources and the AGN tailed galaxy; magenta boxes correspond to the central mini-halo.

Rajpurohit et al. 2021). Therefore, the correlation indicates that the decline of the non-thermal radio component is shallower than the thermal one: this slope can be explained by re-acceleration models, while it is a challenge for hadronic models (as explained by Govoni et al. 2001).

Most of the thermal energy content of a galaxy cluster results from the dissipation of the kinetic energy via shock waves and turbulent cascade (that are stronger in the case of major mergers). A (small) fraction of this energy can be channeled into relativistic particles and magnetic field, while the rest of the dissipated energy is thermalized in the hot ICM. Thus, in the framework of re-acceleration models, a correlation between the thermal and non-thermal components is expected.

With simple assumptions, it is easy to derive the expected linear relation between radio and X-ray surface brightness. The radio emissivity due to synchrotron emission j_R at a given frequency ν, depends on the number density of relativistic electrons $N(E)dE = N_0 E^{-\delta} dE$ and on the magnetic field strength B (see eq. 2.3). Assuming a single radio spectral index $\alpha = 1$, eq. 2.3 becomes

$$j_R \propto E_{CRe} \cdot u_B \cdot \nu^{-1} \tag{6.2}$$

where $E_{CRe} = \int EN(E)dE$ is the relativistic electron energy density and $u_B = B^2/8\pi$ is the magnetic field energy density.

Instead, the X-ray emissivity j_X depends on the thermal gas density n_e and temperature T_X as $j_X \propto n_e^2 \sqrt{k_B T_X}$. Given the relation for the thermal energy density

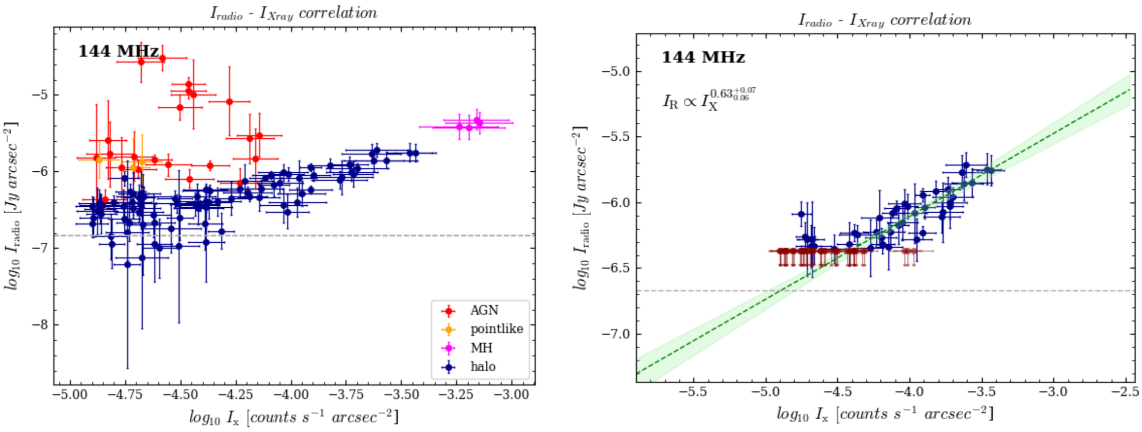

(a) (b)

Fig. 6.3: *Left panel:* $I_R - I_X$ scatter plot of the various contamination sources. Magenta points correspond to mini-halo central boxes; red and orange points correspond to AGN tailed galaxy and point-like sources boxes. The horizontal grey dash-dotted lines indicate the 1σ in the radio maps. *Right panel:* $I_R - I_X$ relation of the halo in A1413, extracted in square boxes with width of $35''$. The radio brightness strongly correlates with the X-ray. Upper limits (dark-red points with arrow) refer to cells where the radio surface brightness is below the 2σ level. The horizontal grey dash-dotted lines indicate the $\sigma = 298\,\mu Jy/beam$ in the radio maps. Shaded green area show samples from the posterior distribution. The best-fit (green dashed line) is reported with the corresponding 1σ confidence interval.

$E_{th} = 3n_e k_B T$, j_X results:

$$j_X \propto E_{th}^2\,(k_B T)^{-3/2}. \tag{6.3}$$

So, if the temperature of the plasma in the regions where $I_R - I_X$ are extracted is the same, a scaling

$$E_{CRe} \cdot u_B \propto E_{th} \tag{6.4}$$

implies a linear scaling between the radio and X-ray brightness (which are the line-of-sight projected emissivities), while a sub-linear scaling implies that the spatial distribution of CRe or magnetic field is broader than that of the thermal plasma. Such a linear relation can be explained by re-acceleration models, assuming that the energy density in relativistic electrons is proportional to the thermal energy density. Moreover, our results imply that $E_{CRe} \cdot u_B \propto E_{th}^{1.7}$, and thus, such a trend is a observational constrain, that theoretical models must undergo.

On the other hand, for hadronic models, j_R has a more constrained dependence, resulting from the fact that the spectrum of the radio emitting electrons is shaped by the parent cosmic ray proton spectrum. Thus, in this case we have:

Halo	Grid	A	r_p
$I_R - I_X$	$35'' \times 35''$	$0.63^{0.07}_{0.06}$	0.82
Mini-Halo	Grid	A	r_p
$I_R - I_X$	$15'' \times 15''$	$1.66^{0.16}_{0.13}$	0.93

Tab. 6.1: `LinMix` fitting slopes and Pearson (r_p) correlation coefficients for the data of Fig. 6.3b and Fig. 6.5.

$$E_{CRe} \propto E_{CRp} E_{th} \tag{6.5}$$

where E_{CRp} is the energy density of relativistic protons in the ICM. Hence, a linear correlation between radio and X-ray brightness in these models can be explained under the assumption that the energy density of magnetic field B and CR in the cluster do not decline with radius; sub-linear correlations require that the energy density of CR increases with radius. These assumptions are not physical and for this reason finding linear or sub-linear scalings between the radio and X-ray surface brightness is a challenge for hadronic models. We conclude that the emission from the halo in A1413 can not be explained in the hadronic scenario.

6.2 Origin of the mini-halo

We used the same approach described above to investigate the $I_R - I_X$ spatial correlation of the central emission. This time, we use the high resolution image that allows to resolve the emission into more independent cells, having a size of $15'' \times 15''$ each. (Fig. fig. A.1a). The region considered for the correlation covers the same mini-halo area used for spectral index calculation in 5.4 (size $r \sim 0.7'$ Govoni et al. 2009), and is shown in Fig. 6.4.

Also in this case, there is a clear evidence of a spatial correlation between radio and X-ray emission, with Pearson coefficient $r_p = 0.93$. Differently from the sub-linear or linear scalings that are reported in the literature for giant radio halo, but consistently with the sample of MHs studied by Ignesti et al. 2020, the relation in super-linear $A = 1.66^{+0.16}_{-0.13}$. The super-linear scaling between I_R and I_X suggests that the number density of emitting electrons and magnetic field rapidly declines from the center to the external regions, and in particular, the radio emission is more peaked than the thermal emission, indicating that the ICM non-thermal component is more concentrated around the central AGN. This is consistent with the hadronic scenario, that predicts a super-linear scaling between the surface brightness for radial decreasing magnetic field (e.g., Govoni et al. 2001). We note, however, that the re-acceleration model can not be excluded, as depending on the CRe distribution it could also produce a superlinear scaling of the X-ray and radio surface brightness.

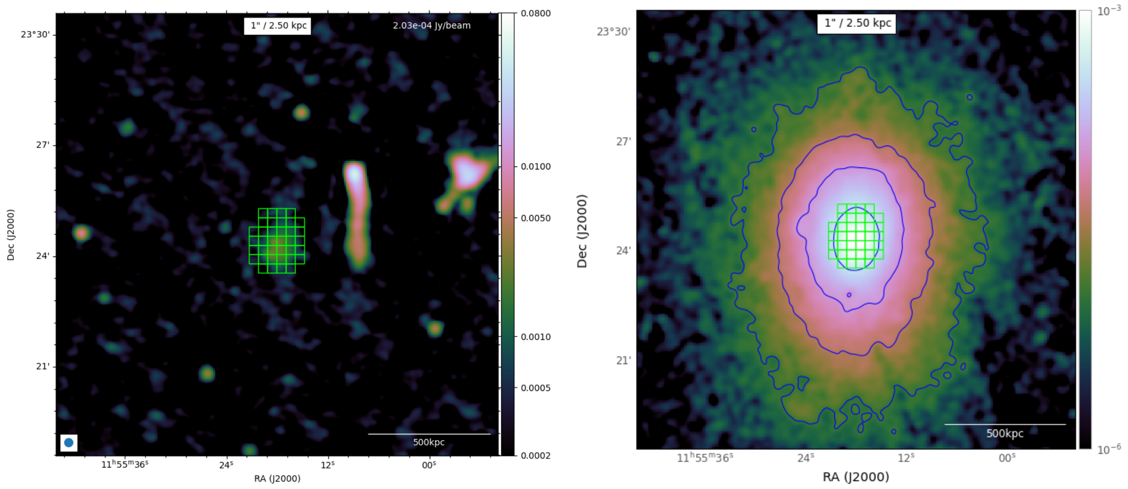

(a) (b)

Fig. 6.4: LOFAR 144MHz image (a) and XMM [0.7-2]keV image (b) of A1413 with grid overlapped. Grid used for correlation, with boxes are 15"x15" size, is overlaid to both images.

6.3 Radio and X-ray spectral properties

The X-ray analysis that we have performed allows us to investigate for possible correlations between the radio emission and other thermal properties of the cluster. We note that this has been done only for few cases in the literature, but it is a very promising analysis to unveil the origin of the radio emission in galaxy clusters, as we will explain

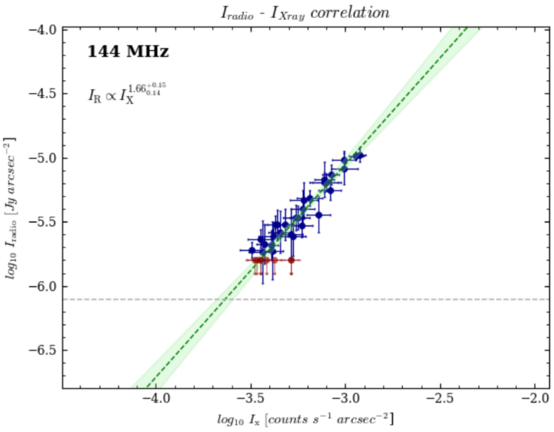

Fig. 6.5: $I_R - I_X$ relation of the mini-halo in A1413, extracted in square boxes with width of $15''$. The radio brightness strongly correlates with the X-ray. Upper limits (dark-red points with arrow) refer to cells where the radio surface brightness is below the 2σ level. The horizontal grey dash-dotted lines indicate the $\sigma = 203\,\mu Jy/beam$ in the radio maps. Shaded green area show samples from the posterior distribution. The best-fit (green dashed line) is reported with the corresponding 1σ confidence interval.

in the following.

We searched for possible connections between the radio surface brightness and X-ray spectral information. Few studies of this kind are known in literature (Pearce et al. 2017, Botteon et al. 2020, Rajpurohit et al. 2021), and indeed, the presence of these correlations is still debated. In the works mentioned above, the point-to-point correlation was performed between the spectral index of the radio emission and the spectral X-ray temperature of the ICM, because the spectral index is more sensitive to the re-acceleration processes and therefore, it is a more trustworthy/accurate proxy than the radio brightness. A comparison between these two quantities was firstly reported by Orrù et al. 2007, who found that highest temperature regions trace the flattest spectrum emission of the radio halo in A2744. It was argued that this correlation provided support to the turbulent re-acceleration model. Later, Pearce et al. 2017 used deeper radio and X-ray data for the same cluster and found no strong evidence for the existence of a correlation between the two quantities. In other recent works, (Botteon et al. 2020, Rajpurohit et al. 2021), it was found that the flat spectral index regions seem to be actually associated with higher temperature regions.
For A1413, no other observation at lower frequencies are available and so, no correlation with the spectral index of the radio halo can be performed. However, as we have accurate T and radio images, we investigate for the first time the possible $I_R - kT$ relation. To investigate this correlation, the same grid shown in Fig. 6.2 and temperature map of Fig. 4.16c have been used.

Since each cell of the grid can include more than one temperature value (see Fig. 6.6a), temperatures of the 2D map inside each point of the grid were averaged with proper weights. Following Mazzotta et al. 2004, we rebinned the temperature map of Fig. 6.6a to find a averaged value T_{mean} for each cell of the grid. The idea is: given a multi-temperature thermal emission, define the temperature as close as possible to the one you would obtain, from the spectra of that cell only. To do that, each temperature value T_i inside a cell must be weighted for

- plasma emissivity: since X-ray emissivity is proportional to the square of the gas density $\epsilon \propto n_e^2$, it is expected that the spectroscopic temperature is determined more by region at higher density

- response of the instrument: XMM−Newton is most sensitive to the soft region of the X-ray spectrum, thus lower temperature should be more weighted. This effect ha a functional form of $\propto (T/keV)^k$, where k depends on the specific observational conditions and on the instrument used. Mazzotta et al. 2004 showed that a good choice for Chandra and XMM−Newton is $k = -0.75$.

- the relative contribution of one temperature to another, i.e. the portion of area relative to a given temperature that falls in the considered cell, respect the total area of the temperature map, having the same temperature: $a_i = A_i/A_{i,tot}$

$$T_{mean} = \frac{\sum_i W_i T_i}{\sum_i W_i}, \quad W_i = \frac{n_i^2}{T_i^{0.75}} a_i \tag{6.6}$$

where the weight W_i gives the relative contribution of the spectral component with temperature T_i to the ideal total spectrum T_{mean}. The results of weighted averaged inside each cell of the grid is displayed in Fig. 6.6b.

The correlation (Fig. 6.7a) is done again with `LinMix` software and the results are listed in Tab. 6.2. We found a moderate positive correlation between the radio surface brightness and the ICM temperature $r_p = 0.37$. The positive correlation is quite moderate and, as such, it will not be investigated further here.

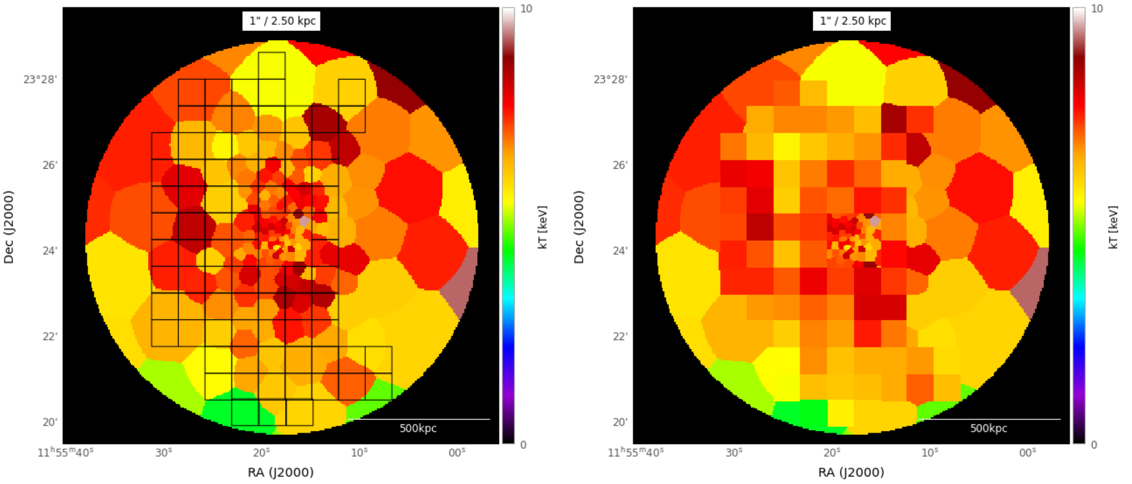

(a) (b)

Fig. 6.6: Temperature map of Fig. 4.16c with grid overlapped (a); Results from temperature averaging in each box of the grid with weight W_i (b).

Halo	Grid	A	r_p
$I_R - kT$	$35'' \times 35''$	$3.15^{1.06}_{1.03}$	0.37
$I_R - P$	$35'' \times 35''$	$0.99^{0.13}_{0.12}$	0.78
$I_R - K$	$35'' \times 35''$	$-1.95^{0.28}_{0.32}$	-0.69

Tab. 6.2: `LinMix` fitting slopes and Pearson (r_p) correlation coefficients for the data of Fig. 6.7.

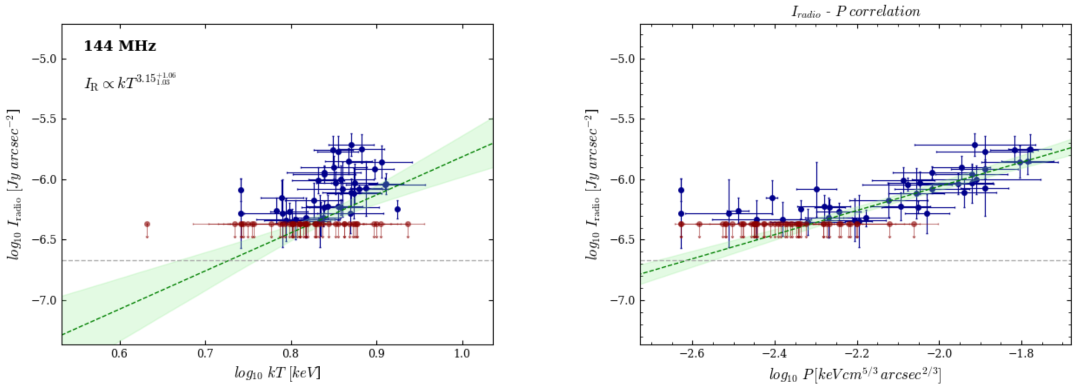

(a) $log(I_R) - log(kT)$ (b) $log(I_R) - log(P)$

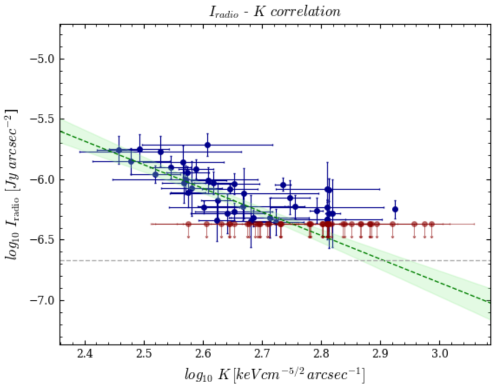

(c) $log(I_R) - log(K)$

Fig. 6.7: Surface brightness of the radio halo against the thermodynamical quantities of the ICM evaluated in the same region: temperature (a), pressure (b), entropy (c), all quantities are projected along the line of sight.

For the first time, we also search for a possible relation between radio surface brightness and pressure or entropy (Fig. 6.7b and Fig. 6.7c). Again, this correlation has been performed using the X-ray maps obtained in Sec. 4.3.6, with proper weights using a procedure similar to the one described before. The correlation is quite strong in both cases: in particular $I_R - P$ appears to be positively correlated with $r_p = 0.78$, while an anti-correlation $r_p = -0.69$ is found for $I_R - K$.

Since the pressure can be used as a proxy for turbulent motions, this correlation is telling something important in the framework of re-acceleration models: regions characterized by higher pressure are tracing regions where the turbulent gas has been re-energised and are those that show a higher radio emissivity.

Also, both high temperature and entropy are expected in regions where the gas has been re-energised by turbulent motions (Gaspari et al. 2014). Therefore, we argue that the dynamics of the gas (turbulence) correlates with entropy making re-acceleration more efficient. That could explain the presence of brighter radio emission in higher entropy regions.

By comparing these latest correlations with the previous $I_R - I_X$, it is evident that the strongest correlation persists between the radio and X-ray surface brightnesses. This confirms a tight connection between the relativistic CRe and the thermal gas.

Conclusions

In this Thesis work, we have presented a composite X-ray and radio analysis of the galaxy cluster A1413. For this purpose, XXM-Newton and LOFAR data were first analysed separately to characterize the properties of the two emissions, and then combined to quantify the connection between the thermal and non-thermal components of the ICM.

The main results can be summarized as follows:

- The X-ray morphology of the cluster on large scales, is not spherically symmetric, confirming the ellipticity found by previous works in both optical and X-ray bands, and suggesting the occurrence of a merger that has left a clear, though minor, imprint on the gas distribution towards the N-S axis of the cluster (Fig. 4.8).
- We have determined the radial and integrated properties of the ICM by performing a spectral analysis within $R_{500} \sim 1224$ kpc from the cluster center. Results from this analysis show that the temperature profile in the core does not decline sharply as it is instead expected in the inner regions of a strong cool-core cluster. Moreover, the metallicity profile is flatter (Fig. 4.10) than what expected for a very relaxed system. However, the surface brightness profile is well fitted with a double β-model, which typically accounts for brightness excess in the central core of cool-core relaxed systems. The total hydrostatic mass enclosed within R_{500} is $M_{500} = (5.99 \pm 0.46)10^{14}\, M_{\odot}$.
- The information that we obtain from our analysis reveal an interesting and peculiar dynamical status of A1413. The morphological indicators $w = 2.7 \cdot 10^{-3}$ and $c = 0.6$ are consistent with the properties of a very relaxed cluster (Fig. 4.15). However, based on statistical studies (Cassano et al. 2010) these kind of systems usually do not host a radio halo, which is instead the case for A1413.

  However, from the calculation of the cooling time, A1413 can be classified as a weak cool-core cluster $t_{cool} = 6.44 \pm 1.29$ Gyr, with a corresponding cooling region $r_{cool} \sim 0.6\, arcmin \approx 90\, kpc$. This is in agreement with the finding of Hudson et al. 2010 who argued that weak cool-core clusters are characterized by moderate cooling time, elevated central entropy, and slightly decreasing central temperature profiles.

- We also derived the thermodynamic 2D maps to investigate local variations of the thermal quantities. As shown in Fig. 4.16c, the temperature map is not typical of relaxed cool-core cluster. Local variations of the temperature are found, that could be due to past minor of major merger events. The presence of diffuse radio emission on the cluster scale (see Fig. 6.1) is also consistent with the scenario of a minor merger event, not powerful enough to significantly perturb the core. In line with this scenario, the radio mini-halo (discovered by Govoni et al. 2009) suggests that the core has not been disrupted.

- We have used low frequency radio data to analyse the non-thermal emission of this cluster. After subtracting the radio point sources that contaminated the diffuse emission, we have imaged the data at low resolution to maximise the sensitivity to low surface brightness emission. This led to the discovery of an extended low-surface brightness emission never detected before, with a large linear size of about 800 kpc. This radio emission is detected so far only at low frequency and extends on scales typical of giant radio halos. Actually, the radio emission hosted by A1413 was previously classified as mini-halo (Giacintucci et al. 2017, Savini et al. 2019) with a size of $\sim 200\,kpc$.

- The extended low brightness halo emission and the central mini-halo-like emission have been studied separately, to understand whether they should be considered as a classical giant halo or as the superpositon of two different sources and re-acceleration mechanisms.

- To this aim, we calculated spectral index values for both emissions. We analysed the spectral index properties between 140 and 1400 MHz combining LOFAR and VLA data taken from the literature. The radio flux density, integrated within the emission from the mini-halo, is characterised by a spectral index $\alpha_{144}^{1.4} = 1.1 \pm 0.17$ We have derived a limit for the spectral index of the halo emission, that must be steeper than $\alpha > 1.6$.

  This suggests the coexistence of two different kinds of radio emission in A1413: the more compact radio emission, that is coincident with the cool core region and has a spectrum typical of a mini-halo with $\alpha_{144}^{1.4} = 1.1 \pm 0.17$; surrounded by a steeper $\alpha > 1.6$ low-brightness diffuse emission.

- Like the optical and X-ray emission, also in the radio band the cluster shows an N-S elongated shape. Moreover, the halo shows a complex structure that seems to be mixed with the AGN tailed galaxy west located as shown in Fig. 5.13 (right). Therefore, we have fitted the extended emission to obtain a reliable and noise-independent value of its size and flux. We have found a total flux of 93.33 ± 12.34mJy within $3r_e$, that coincides to $P_{144} = (5.26{\pm}0.69)\ 10^{24}\ W/Hz$. Thus, the large-scale radio emission from A1413 is consistent with the $P_{144} - M_{500}$ relation expected for steep radio halos detected at low frequency.

- We have performed a point-to-point correlation analysis between the X-ray and radio surface brightness, which confirms the spatial connection between the non-thermal and thermal emission in galaxy clusters. We have investigated a possible correlation for both the halo and the mini-halo regions separately, to check if they show different trends typical of mini halos and giant halos.

- In agreement with previous studies (e.g., Govoni et al. 2001, Botteon et al. 2020), the radio brightness of the halo strongly correlates ($r_p = 0.82$) with the X-ray brightness, with a sub-linear scaling $I_r \propto I_X^{0.63^{+0.07}_{-0.06}}$. A linear or sublinear scaling between the $I_R - I_X$ is in line with turbulent re-acceleration models, while can not be explained by hadronic models. Thus, we conclude that the emission from the halo can not be explained in the hadronic scenario.

- The mini-halo central region, instead, presents a super-linear relation $I_r \propto I_X^{1.66^{0.16}_{0.13}}$ and even a stronger correlation $r_p = 0.93$. This is in contrast with what has been found for giant halos, and in agreement with the results found for mini-halos (Ignesti et al. 2020).

  A super-linear scaling between I_X and I_R suggests that the number density of emitting electrons and magnetic field rapidly declines from the center to the external regions, as predicted by the hadronic scenario. However, re-acceleration models cannot be excluded, as a super-linear scaling of the X-ray and radio surface brightness could be produced, depending on the exact CRe distribution.

- The different trends of the two radio sources further strengthens the idea that the radio emission of A1413 is composed by two different components. This would mean that the mechanisms responsible for the (re)acceleration of the radio emitting particle are different.

- The point-to-point comparison has been performed also between the radio surface brightness and other ICM thermodynamic properties, for the halo diffuse source. The strongest correlations is found between I_R and pressure. We argue that regions characterized by higher pressure are those where the turbulent gas has been re-energised, and hence have a higher emissivity. This is e a further indication of the connection between radio emission and turbulent heating of the gas in the ICM.

Low Resolution Radio Images

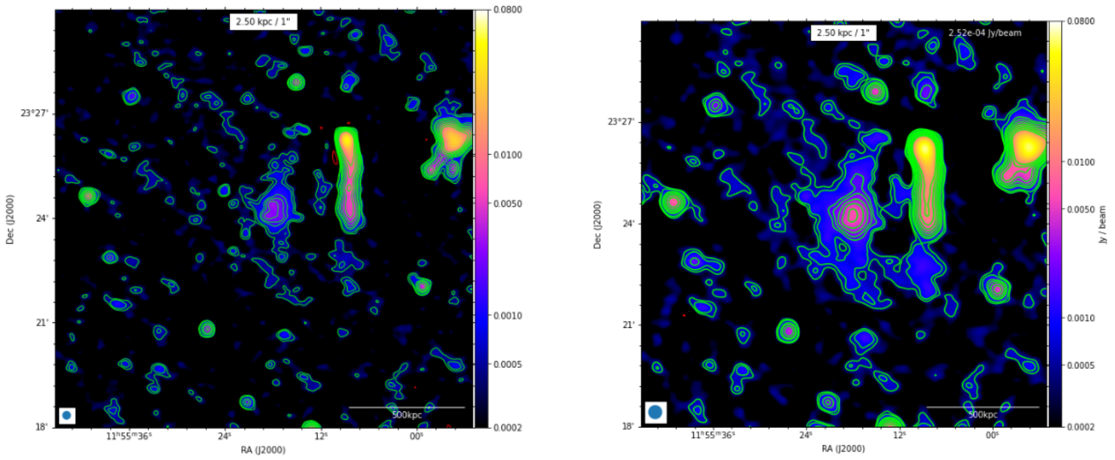

(a) beam 15x15, $\sigma = 203\,\mu\mathrm{Jy/beam}$, $\mathrm{S} = 27.37 \pm 4.22\,\mathrm{mJy}$

(b) beam 25x25, $\sigma = 252\,\mu\mathrm{Jy/beam}$, $\mathrm{S} = 43.26 \pm 6.62\,\mathrm{mJy}$

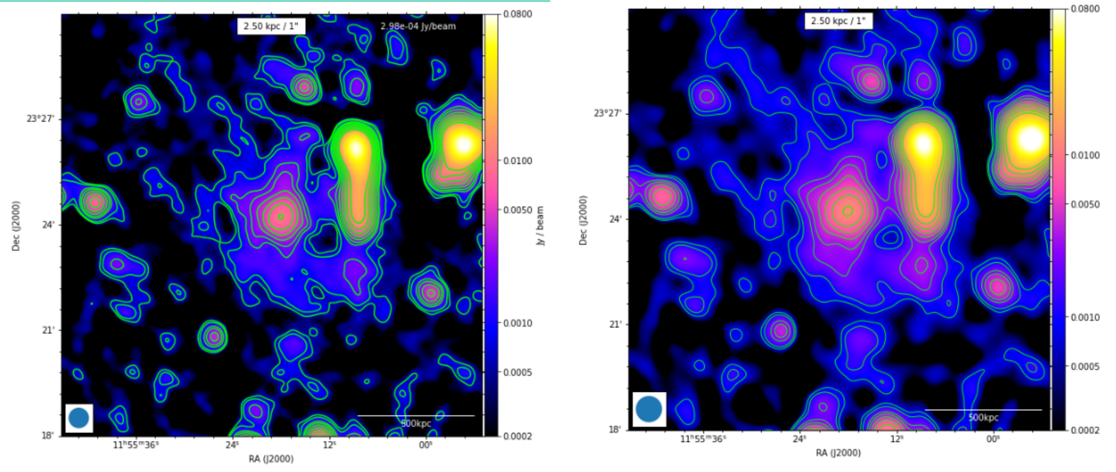

(c) beam 35x35, Contours=[-3,2,3,6…,45]σ $\sigma = 298\,\mu\mathrm{Jy/beam}$, $\mathrm{S} = 58.08 \pm 8.86\,\mathrm{mJy}$,

(d) beam 45x45, $\sigma = 385\,\mu\mathrm{Jy/beam}$, $\mathrm{S} = 56.63 \pm 8.66\,\mathrm{Jy}$

Fig. A.1: Low resolution at 144MHz image with increasing beam size (displayed in the bottom left area of the images) from (a) to (d). Fluxes within 3σ contour are listed below each image.

Bibliography

Abell, G.O. (1958). “The Distribution of Rich Clusters of Galaxies.” In:

Arnaud&Evrard (1999). “The L$_X - Trelationandintraclustergasfractionsof X - rayclusters$”. In: *MNRAS*. DOI: 10.1046/j.1365-8711.1999.02442.x.

Arnauld (1996). “XSPEC: the first ten years”. In: *Astronomical data analysis software and Systems*.

ASTRON-WebSite (n.d.). URL: https://www.astron.nl/.

Bacchi, M. et al. (2003). “Deep images of cluster radio halos”. In: *A&A*.

Bagchi, J. et al. (2002). “Evidence for Shock Acceleration andIntergalactic Magnetic Fields in a Large-ScaleFilament of Galaxies ZwCl 2341.1+0000”. In: DOI: 10.1016/S1384-1076(02)00137-9.

Baldi, A. et al. (2007). “A CHANDRA ARCHIVAL STUDY OF THE TEMPERATURE AND METAL ABUNDANCE PROFILES IN HOT GALAXY CLUSTERS AT $0.1 \leq z \leq 0.3$”. In: *The Astrophysical Journal*.

Beck&Krause (2005). “Revised equipartition minimum energy formula for magneticfield strength estimates from radio synchrotron observations”. In: *Astron. Nachr.*

Bîrzan, L. et al. (2004). “A Systematic Study of Radio-induced X-Ray Cavities in Clusters, Groups, and Galaxies”. In: *The Astrophysical Journal*. DOI: 10.1086/383519.

— (2008). “Radiative Efficiency and Content of Extragalactic Radio Sources: Toward a Universal Scaling Relation between Jet Power and Radio Power”. In: *The Astrophysical Journal*. DOI: 10.1086/591416.

Blasi, P et al. (2007). “GAMMA RAYS FROM CLUSTERS OF GALAXIES”. In: DOI: 10.1142/S0217751X0703529X.

Böhringer, H. et al. (2010). “Substructure of the galaxy clusters in the REXCESS sample:observed statistics and comparison to numerical simulations”. In: *A&A*. DOI: 10.1051/0004-6361/200913911.

Böhringer&Norbert (2010). “X-ray spectroscopy of galaxy clusters: studying astrophysical processes in the largest celestial laboratories”. In:

Bonafede, A. et al. (2010). “The Coma cluster magnetic field from Faraday rotation measures”. In: *A&A*.

— (2014). “A giant radio halo in the cool core cluster CL1821+643”. In:

Botteon, A. et al. (2018). “Shocks and cold fronts in merging and massive galaxy clusters: new detections with Chandra”. In: *MNRAS*. DOI: 10.1093/mnras/sty598.

— (2020). “The beautiful mess in Abell 2255”. In: *The Astrophysical Journal*. DOI: 10.3847/1538-4357/ab9a2f.

Boxelaar, J.M. et al. (2021). “A robust model for flux density calculations of radio halos in galaxy clusters: Halo-FDCA”. In: *Astronomy and Computing*. DOI: 10.1016/j.ascom.2021.100464.

Bravi, L. et al. (2016). “On the connection between radio mini-halos and gas heating in cool core clusters”. In: *MNRAS*. DOI: arXiv:1603.00368.

Briggs, D. (1995). “HIGH FIDELITY DECONVOLUTION OF MODERATELY RESOLVED SOURCES - PhD Thesis, New Mexico Institude of Mining and Technology”. In:

Brüggen, M. et al. (2012). “Magnetic Fields, Relativistic Particles, and Shock Waves in Cluster Outskirts”. In: *Space Sci Rev*. DOI: 10.1007/s11214-011-9785-9.

Brunetti, G. et al. (2007). “COSMIC RAYS AND RADIO HALOS IN GALAXY CLUSTERS: NEW CONSTRAINTS FROM RADIO OBSERVATIONS”. In: *The Astrophysical Journal*.

— (2009). “On the evolution of giant radio halos and their connectionwith cluster mergers”. In: *A&A*. DOI: 10.1051/0004-6361/200912751.

— (2013). “Is the Sunyaev-Zeldovich effect responsible for the observed steepening in the spectrum of the Coma radio halo?” In: *A&A*. DOI: 10.1051/0004-6361/201321402.

Brunetti&Jones (2014). “Cosmic Rays in Galaxy Clsuters and their non-thermal emission”. In: *International Journal of Modern Physics*.

Brunetti&Lazarian (2007). “Compressible turbulence in galaxy clusters: physics and stochasticparticle re-acceleration”. In: *Mon. Not. R. Astron. Soc.* DOI: 10.1016/S1384-1076(02)00137-9.

Carilli&Taylor (2002). “Cluster Magnetic Fields”. In: *Annual Review*. DOI: 10.1146/annurev.astro.40.060401.093852.

Carter&Read (2007). “The XMM-Newton EPIC background and the productionof background blank sky event files”. In: *A&A*. DOI: 10.1051/0004-6361:20065882.

Cassano, R. et al. (2004). “Occurence and Luminosity Functions of Giant Radio Halos from Magneto-TurbulentModel”. In: *Journal of the Korean Astronomical Society*. DOI: 10.5303/JKAS.2004.37.5.589.

— (2006). “Statistics of giant radio haloes from electron reacceleration models”. In: *Mon. Not. R. Astron. Soc.* DOI: 10.1111/j.1365-2966.2006.10423.x.

— (2008). “A morphological comparison between giant radio halos and radiomini-halos in galaxy clusters”. In: *A&A*. DOI: 10.1051/0004-6361:200810179.

— (2010). "ON THE CONNECTION BETWEEN GIANT RADIO HALOS AND CLUSTER MERGERS". In: *The Astrophysical Journal Letters*. DOI: 10.1088/2041-8205/721/2/L82.

— (2013). "REVISITING SCALING RELATIONS FOR GIANT RADIO HALOS IN GALAXY CLUSTERS". In: *The Astrophysical Journal Letters*. DOI: 10.1088/0004-637X/777/2/141.

Castagné, D. et al. (2012). "Deep optical observations of the massive galaxy cluster Abell 1413". In: *Astronomy&Astrophysics* 548. DOI: 10.1051/0004-6361/201116837.

Cavagnolo, K. W. et al. (2010). "A relationship between AGN jet power and radio power". In: *The Astrophysical Journal*.

CHEX-MATE Collaboration: Arnaud, M., S. Ettori, et al. (2020). "The Cluster HEritage project with XMM-Newton: Mass Assembly and Thermodynamics at the Endpoint of structure formation. I. Programme overview". In: URL: https://arxiv.org/abs/2010.11972.

collaboration et al. (2014). "Planck2013 results. XXIX. ThePlanckcatalogueof Sunyaev-Zeldovich sources". In: *A&A*. DOI: 10.1051/0004-6361/201321523.

Condon, James J. and Scott M. Ransom (2015). *Essential Radio Astronom*.

Cornwell, T.J. (2008). "Multiscale CLEAN Deconvolution of Radio Synthesis Images". In:

Cuciti, V. et al. (2021). "Radio halos in a mass-selected sample of 75 galaxy clusters. II. Statistical analysis". In: *A&A*. DOI: 10.1051/0004-6361/202039208.

deLuca&Molendi (2004). "The 2–8 keV cosmic X-ray background spectrum as observed-with XMM-Newton". In: *A&A*. DOI: 10.1051/0004-6361:20034421.

Diehl, S. et al. (2008). "Constraining the Nature of X-Ray Cavities in Clusters and Galaxies". In: *The Astrophysical Journal*. DOI: 10.1086/591310.

Diehl&Statler (2006). "Adaptive binning of X-ray data with weighted Voronoi tessellations". In: *Mon. Not. R. Astron. Soc.* DOI: 10.1111/j.1365-2966.2006.10125.x.

Dolag, K. et al. (1999). "SPH simulations of magnetic fields in galaxy clusters". In: *A&A*.

— (2008). "Non-thermal processes in cosmological simulations". In:

Dressler, A. (1980). "A CATALOG OF MORPHOLOGICAL TYPES IN 55 RICH CLUSTERS OF GALAXIES". In: DOI: 10.1146/annurev-astro-081811-125502.

Enßlin, T. et al. (2011). "Cosmic ray transport in galaxy clusters: implications for radio halos, gamma-ray signatures, and cool core heating". In: *A&A*. DOI: 10.1051/0004-6361/201015652.

Fabian, A.C. et al. (1994). "ASCA Observations of Cooling Flows in Clusters of Galaxies". In:

Farnsworth, D. et al. (2013). "Discovering of Megaparsec-scale, low surface brightness nonthermal emission in merging galaxy clusters using the green bank telescope". In: DOI: 10.1088/0004-637X/779/2/189.

Feretti, L. et al. (2001). “The giant radio halo in Abell 2163”. In: *A&A*. DOI: 10.1051/0004-6361:20010581.

— (2012). “Clusters of galaxies : observational properties of the diffuseradio emission”. In: DOI: 10.1007/s00159-012-0054-z.

Ferrari, C. et al. (2008). “Observations of Extended Radio Emission in Clusters”. In: *Space Sci Rev*. DOI: 10.1007/s11214-008-9311-x.

Furlanetto&Loeb (2001). “An Intergalactic Magnetic Field from Quasar Outflows”. In: DOI: 10.1007/10856495_64.

Fusco-Femiano, R. et al. (2000). “HARD X-RAY EMISSION FROM THE GALAXY CLUSTER A2256”. In: *The Astrophysical Journal*.

— (2001). “Hard X-Ray Emission from the Galaxy Cluster A3667”. In: *The Astrophysical Journal*.

Fusco-Fermiano, Cavaliere & (1976). “X-rays from hot plasma in galaxy cluster”. In: *A&A*.

Gaspari, M. et al. (2014). “The relation between gas density and velocity power spectra in galaxy clusters: High-resolution hydrodynamic simulations and the role of conduction.” In: *A&A*. DOI: 10.1051/0004-6361/201424043.

Gasperin, F. de et al. (2017). “Gentle re energization of electrons in merging galaxy clusters”. In:

Giacintucci, S. et al. (2005). “Spectral properties and origin of the radio halo in A3562”. In: *A&A*. DOI: 10.1051/0004-6361:20053016.

— (2017). “Occurrence of Radio Minihalos in a Mass-limited Sample of Galaxy Clusters”. In: *The Astrophysical Journal*. DOI: 10.3847/1538-4357/aa7069.

Giovannini&Feretti (2000). “Halo and Relic Sources in Clusters of Galaxies”. In: DOI: 10.1016/S1384-1076(00)00034-8.

Gitti, M. et al. (2002). “Modeling the interaction between ICM and relativistic plasma in cooling flows: The case of the Perseus cluster”. In: *A&A*. DOI: 10.1051/0004-6361:20020284.

— (2012). “Evidence for AGN Feedback in Galaxy Clusters and Groups”. In: DOI: 10.1155/2012/950641.

Govoni, F. et al. (2001). “A comparison of radio and X-ray morphologies of four clusters of galaxies containing radio halos”. In: *A&A*. DOI: 10.1051/0004-6361:20010115.

— (2009). “A search for diffuse radio emission in the relaxed, cool-core galaxyclusters A1068, A1413, A1650, A1835, A2029, and Ophiuchus”. In: *A&A* 499. DOI: 10.1051/0004-6361/200811180.

Govoni&Feretti (2004). “MAGNETIC FIELDS IN CLUSTERS OF GALAXIES”. In: *Int.J.Mod.Phys.* DOI: 10.1142/S0218271804005080.

Grasso, Dario and Hector R. Rubinstein (2001). “Magnetic Fields in the Early Universe”. In:

Gunn&Gott (1972). "On the Infall of Matter Into Clusters of Galaxies and Some Effects on Their Evolution". In:

Haarlem, M.P. van et al. (2013). "LOFAR: The LOw-Frequency ARray". In: *A&A*. DOI: 10.1051/0004-6361/201220873.

Hoshino, A. et al. (2010). "X-ray Temperature and Mass Measurements to the Virial Radius of Abell 1413 with Suzaku". In: *Astronomical Society of Japan* 62, pp. 371–389. DOI: https://doi.org/10.1093/pasj/62.2.371.

Hudson, D.S. et al. (2010). "What is a Cool-Core Cluster? A Detailed Analysis of the Cores of the X-ray Flux-Limited HIFLUGCS Cluster Sample". In:

Ignesti, A. et al. (2020). "Radio and X-ray connection in radio mini-halos:implications for hadronic models". In: *A&A*. DOI: 10.1051/0004-6361/201937207.

Kelly, B.C. et al. (2007). "SOME ASPECTS OF MEASUREMENT ERROR IN LINEAR REGRESSION OF ASTRONOMICAL DATA". In: *The Astrophysical Journal*.

Kelner, S.R. et al. (2006). "Energy spectra of gamma-rays, electrons and neutrinos produced at proton-proton interactions in the very high energy regime". In: DOI: 10.1103/PhysRevD.74.034018.

King, I. (1962). "The Structure of Star Clusters. I. An Empirical Density Law". In: *MNRAS*. DOI: 10.1111/j.1365-2966.2006.10199.x.

Kravtsov, A.V. (2012). "Formation of Galaxy Clusters". In: DOI: 10.1146/annurev-astro-081811-125502.

Kulsrud, R.M. et al. (1997). "Magnetic Fields in the Early Universe". In: *THE ASTROPHYSICAL JOURNAL*.

LaRoque, S. J. et al. (2006). "X-RAY AND SUNYAEV-ZEL'DOVICH EFFECT MEASUREMENTS OF THE GASMASS FRACTION IN GALAXY CLUSTERS". In: *The Astrophysical Journal*,

Longair, Malcolm S. (2011). *High Energy Astrophysics*. Cambridge University Press.

Lovisari, L. et al. (2011). "Inhomogeneous metal distribution in the intracluster medium". In: *A&A*. DOI: 10.1051/0004-6361/201015400.

— (2017). "X-Ray Morphological Analysis of the Planck ESZ Clusters". In: *The Astrophysical Journal* 846. DOI: 10.3847/1538-4357/aa855f.

— (2019). "The non-uniformity of galaxy cluster metallicity profiles". In: *MNRAS*. DOI: 10.1093/mnras/sty3130.

Marelli, M. et al. (2017). "A systematic analysis of the XMM-Newtonbackground: I. Dataset and extraction procedures". In: DOI: 10.1007/s10686-017-9542-5.

Matthews, T.A. et al. (1964). "A Discussion of Galaxies Indentified with Radio Sources." In:

Mazzotta, P. et al. (2004). "Comparing the temperatures of galaxy clusters from hydrodynamical N-body simulations to Chandra and XMM–Newton observations". In: *MNRAS*. DOI: 10.1111/j.1365-2966.2004.08167.x.

McDonald, M. et al. (2018). “Revisiting the Cooling Flow Problem in Galaxies, Groups, and Clusters of Galaxies”. In: DOI: 10.3847/1538-4357/aabace.

McNamara&Nulsen (2007). “Heating Hot Atmospheres with Active Galactic Nuclei”. In: DOI: 10.1146/annurev.astro.45.051806.110625.

Mernier, F. et al. (2017). “Radial metal abundance profiles in the intra-cluster mediumof cool-core galaxy clusters, groups, and ellipticals”. In: DOI: 10.1051/0004-6361/201630075.

Mevius, M. et al. (1999). “Imaging with Non-Complanar arrays”. In:

— (2016). “Probing Ionospheric Structures using the LOFAR radio telescope”. In:

Murgia, M. et al. (2009). “Comparative analysis of the diffuse radio emission in the galaxy clusters A1835, A2029, and Ophiuchus”. In: *A&A*.

Nevalainen, J. et al. (2005). “XMM-NEWTONEPIC BACKGROUND MODELING FOR EXTENDED SOURCES”. In: *The Astrophysical Journal*.

O’Sullivan, E. et al. (2011). “Heating the Hot Atmospheres of Galaxy Groups and Clusters with Cavities: The Relationship between Jet Power and Low-frequency Radio Emission”. In: *The Astrophysical Journal*. DOI: 10.1088/0004-637X/735/1/11.

Offringa, A.R. et al. (2014). “WSClean: an implementation of a fast, generic wide-field imager for radio astronomy”. In: *Mon. Not. R. Astron. Soc.* DOI: 10.1093/mnras/stu1368.

Orrù, E. et al. (2007). “Low-frequency study of two clusters of galaxies:A2744 and A2219”. In: *A&A*. DOI: 10.1051/0004-6361:20066118.

Paturel, G. et al. (1989). “An extragalactic database. I. The catalogue of principal galaxies.” In: *A&A*.

Pearce, C.J.J. et al. (2017). “VLA Radio Observations of theHSTFrontier Fields Cluster Abell 2744:The Discovery of New Radio Relics”. In: *The Astrophysical Journal*. DOI: 10.3847/1538-4357/aa7e2f.

Perese, C. B. et al. (1998). “A ROSAT study of the cores of clusters of galaxies – I. Cooling flows in an X-ray flux-limited sample”. In: *Mon. Not. R. Astron. Soc.*

Pfrommer, C. and T. A. Enßlin (2004). “Constraining the population of cosmic ray protons in cooling flow clusters with-ray and radio observations:Are radio mini-halos of hadronic origin?” In: DOI: 10.1051/0004-6361:20031464.

Pizzo, R.F. (2010). “Tomography of galaxy clusters through low-frequency radio polarimetry - Ph.D. Thesis”. In:

Pointecouteau, E. et al. (2005). “The structural and scaling properties of nearby galaxy clusters”. In: *Astronomy&Astrophysics* 441, pp. 893–903. DOI: 10.1051/0004-6361:20052856.

Pratt, G. W. and M. Arnaud (2002). “The mass profile of A1413 observed with *XMM-Newton*: implications for te *M-T* relation”. In: *Astronomy&Astrophysics* 394, pp. 375–393. DOI: 10.1051/0004-6361:20021032.

Pratt, G.W. et al. (2008). "Temperature profiles of a representative sample of nearby X-raygalaxy clusters". In: *The Astrophysical Journal.* DOI: `10.1051/0004-6361:20065676`.

Rajpurohit, K. et al. (2021). "Dissecting nonthermal emission in the complex multiple-merger galaxy cluster Abell 2744: Radio and X-ray analysis". In: *A&A.*

Rawle, T.D. et al. (2012). "THE RELATION BETWEEN COOL CLUSTER CORES AND HERSCHEL-DETECTED STAR FORMATION IN BRIGHTEST CLUSTER GALAXIES". In: *The Astrophysical Journal.* DOI: `10.1088/0004-637X/747/1/29`.

Read, A. M. et al. (2011). "A new comprehensive 2D model of the point spread functions of the XMM-Newton EPIC telescopes: spurious source suppression and improved positional accuracy". In: *AA.* DOI: `10.1051/0004-6361/201117525`.

Rossetti, M. et al. (2015). "Measuring the dynamical state ofPlanckSZ-selected clusters:X-ray peak – BCG offset". In: *MNRAS.* DOI: `10.1093/mnras/stw265`.

Santos, J.S. et al. (2008). "Searching for cool core clusters at high redshift". In: *A&A.* DOI: `10.1051/0004-6361:20078815`.

Savini, F. et al. (2018). "First evidence of diffuse ultra-steep-spectrum radioemission surrounding the cool core of a cluster". In: *Monthly Notices of the Royal Astronomical Society.* DOI: `10.1093/mnras/sty1125`.

— (2019). "A LOFAR study of non-merging massive galaxy clusters". In: *Astronomy&Astrophysics* 622. DOI: `10.1051/0004-6361/201833882`.

Shimwell, T.W. et al. (2014). "Deep radio observations of the radio halo of the bullet cluster 1E 0657-55.8". In: *MNRAS.* DOI: `10.1093/mnras/stu467`.

— (2019). "The LOFAR Two-metre Sky Survey". In: *A&A.* DOI: `10.1051/0004-6361/201833559`.

Smith, R.K. et al. (2001). "COLLISIONAL PLASMA MODELS WITH APEC/APED: EMISSION-LINE DIAGNOSTICSOF HYDROGEN-LIKE AND HELIUM-LIKE IONS". In: *The Astrophysical Journal.*

Snowden, S.L. et al. (2008). "A catalog of galaxy clusters observed by XMM-Newton". In: *A&A.* DOI: `10.1051/0004-6361:20077930`.

Sokoloff, D.D. et al. (1999). "Depolarization and Faraday effects in galaxies". In: *Monthly Notices of the Royal Astronomical Society.* DOI: `10.1046/j.1365-8711.1999.02161.x`.

Spitzer, L. (1956). "Physics of Fully Ionized Gases". In:

Springel, V. (2005). "The cosmological simulation codeGADGET-2". In: DOI: `10.1093/mnras/stu1536`.

Sutherland&Dopita (1993). "Cooling Functions for Low-Density Astrophysical Plasmas". In: *The Astrophysical Journal.*

Taylor, G.B. et al. (2002). "Magnetic fields in the Centaurus cluster". In: *Mon.Not.R.Astron.Soc.*

Thomas L. Wilson Kristen Rohlfs, Susanne Hüttemeister (2013). *Tools of Radio Astronomy*. SpringerLink.

Thompson, A.R. et al. (2007). *Interferometry and Synthesis in Radio Astronomy - Third Edition*.

Vantyghem, A. N. et al. (2014). "Cycling of the powerful AGN in MS 0735.6+7421 and the duty cycle ofradio AGN in clusters". In: *MNRAS*. DOI: 10.1093/mnras/stu1030.

vanWeeren, R. J. et al. (2019). "Diffuse Radio Emission from Galaxy Clusters". In: *Space Sci Rev*. DOI: 10.1007/s11214-019-0584-z.

— (2020). "LOFAR observations of galaxy clusters in HETDEX". In: *A&A*.

Vazza, F. et al. (2014). "On the amplification of magnetic fields in cosmic filamentsand galaxy clusters". In: *MNRAS*.

Venturi, T. et al. (2008). "GMRT radio halo survey in galaxy clusters at z= 0.2–0.4". In: *A&A*. DOI: 10.1051/0004-6361:200809622.

— (2017). "The two-component giant radio halo in the galaxycluster Abell 2142". In: *A&A*. DOI: 10.1051/0004-6361/201630014.

Vikhlinin, A. et al. (2005). "CHANDRA TEMPERATURE PROFILES FOR A SAMPLE OF NEARBY RELAXED GALAXY CLUSTERS". In: *The Astrophysical Journal,*

— (2006). "CHANDRA SAMPLE OF NEARBY RELAXED GALAXY CLUSTERS: MASS, GAS FRACTION,AND MASS-TEMPERATURE RELATION". In: *The Astrophysical Journal*.

Voelk&Atoyan (2000). "EARLY STARBURSTS AND MAGNETIC FIELD GENERATION IN GALAXY CLUSTERS". In: *ApJ*.

Vogelsberger, M. et al. (2013). "Introducing the Illustris Project: Simulating the coevolution of dark and visible matter in the Universe". In: DOI: 10.1093/mnras/stu1536.

Voigt&Fabian (2006). "Galaxy cluster mass profiles". In: *MNRAS*. DOI: 10.1111/j.1365-2966.2006.10199.x.

Weaver, K. et al. (2020). *The XMM-Newton ABC Guide: An Introduction to XMM-Newton Data Analysis*. URL: https://heasarc.gsfc.nasa.gov/docs/xmm/abc/.

Wik, D.R. et al. (2014). "NuSTAR OBSERVATIONS OF THE BULLET CLUSTER:CONSTRAINTS ON INVERSE COMPTON EMISSION". In: DOI: 10.1088/0004-637X/792/1/48.

Willingale, R. et al. (2013). "Calibration of X-ray absorption in our Galaxy". In: *MNRAS*. DOI: 10.1093/mnras/stt175.

Wilson, T.L. et al. (2013). *Tools of Radio Astronomy - Sixth Edition*.

XMM-ESA-WebSite (n.d.). URL: https://www.cosmos.esa.int/web/xmm-newton.

XMM-Newton Users Handbook (n.d.). URL: https://xmm-tools.cosmos.esa.int/external/xmm_user_support/documentation/uhb/.

Yuan, Z. S. et al. (2015). "THE SCALING RELATIONS AND THE FUNDAMENTAL PLANE FOR RADIO HALOS AND RELICS OF GALAXY CLUSTERS". In: *ApJ.* DOI: 10.1088/0004-637X/813/1/77.

Zandanel, F. et al. (2015). "On the Physics of Radio Halos in Galaxy Clusters: Scaling Relations and Luminosity Functions". In: DOI: 10.1093/mnras/stt2250.

Zhang, Y. et al. (2009). "X-RAY SUBSTRUCTURE STUDIES OF FOUR GALAXY CLUSTERS USING XMM-NEWTON DATA". In: *The Astrophysical Journal.* DOI: 10.1088/0004-637X/699/2/1178.

ZuHone, J.A. et al. (2013). "TURBULENCE AND RADIO MINI-HALOS IN THE SLOSHING CORES OF GALAXY CLUSTERS". In: *The Astrophysical Journal.* DOI: 10.1088/0004-637X/762/2/78.